

# Investigations of seismic anisotropy beneath the Macquarie Ridge Complex

Haoran Du

A thesis submitted for the degree of  
*Master of Philosophy*  
at The Australian National University



Australian  
National  
University

The Australian National University  
Research School of Earth Sciences

August, 2023

© Copyright by Haoran Du 2023

All Rights Reserved

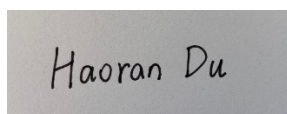
# Declaration

I, Haoran Du, declare that this thesis is my own original work undertaken at the Research School of Earth Sciences, Australian National University.

I certify that this work contains no material which has been accepted for the award of any other degree or diploma in my name, in any university or other tertiary institution and, to the best of my knowledge and belief, contains no material previously published or written by another person, except where due reference has been made in the text. In addition, I certify that no part of this work will, in the future, be used in a submission in my name, for any other degree or diploma in any university or other tertiary institution without the prior approval of the Australian National University.

I certify that the total word count of this thesis is: 20429, inclusive of figure captions and appendices, but excluding the bibliography.

Signature:

A rectangular box containing the handwritten signature "Haoran Du" in black ink on a light gray background.

4 August, 2023

# Acknowledgement

At the end of the completion of my thesis, I'd like to express my gratitude to many people and the organizations who gave me continuous support during my study of the Master of Philosophy of Earth Sciences program at the Australian National University.

Foremost, I am deeply grateful to my primary supervisor, Dr. Caroline M. Eakin, for her unwavering support and guidance throughout my Master's program. Her expertise and patience have been invaluable to me and have played a crucial role in the success of the thesis. I could not have imagined having a better supervisor and advisor for my study.

Besides my primary supervisor, I would like to thank the rest of my panel: Professor Hrvoje Tkalčić, Professor Meghan Miller and Dr. Chengxin Jiang, for their encouragement, feedback and insightful comments for my study.

I am also grateful to the Australian National University and the Research School of Earth Sciences for providing me with the essential facilities and resources to conduct my research.

Finally, I would like to extend my sincere gratitude to all of my families and friends for their love and support during this process. Without their encouragement and motivation, I would not have been able to complete this journey.

# Abstract

The Macquarie Ridge Complex (MRC) is located along the southeastern Australian-Pacific plate boundary, south of New Zealand. Given its remote location in the Southern Ocean, seismic station deployments are lacking, and therefore very few direct observations of seismic anisotropy have been made. The dynamics of this plate boundary are however of great interest due to changes in the plate boundary style both along strike and over time. Particular segments of the MRC are associated with trans-pressional motion (e.g., McDougall and Macquarie segments), while subduction initiation has been inferred for others (e.g., Puysegur and Hjort segments). Here we conduct source-side splitting analysis to investigate upper mantle dynamics using earthquakes that have occurred along this plate boundary. We combine this with a detailed investigation of SKS/PKS receiver-side splitting at the long-running permanent station on Macquarie Island (station: MCQ). We find the results from shear-wave splitting are locally consistent but vary along the plate boundary, potentially suggesting changes in seismic anisotropy and the pattern of the underlying mantle deformation. Analysis of the First Fresnel Zone are applied to explore how the different ray-paths may sample the sub-surface anisotropy at various depths. A comparison is then made with expected patterns of anisotropy in the lithosphere versus from the asthenosphere, by comparing with predictions from seafloor spreading, plate motions, and global azimuthal anisotropy models. Following this, the primary source of the anisotropy detected is considered more likely from the asthenospheric upper mantle, rather than the oceanic lithosphere which is relatively young (~10-35 million years) and thin (less than ~77 km) in this region.

Altogether, our splitting observations demonstrate the pattern of mantle deformation beneath the MRC changes both with proximity to the plate



boundary, as well as along the plate boundary itself, potentially reflecting the ongoing evolution of this plate boundary both in space and time.

# Contents

Declaration.....	I
Acknowledgement.....	II
Abstract.....	III
Chapter 1.....	1
Introduction.....	1
1.1 Thesis Overview and Motivation.....	1
1.2 Seismic anisotropy background.....	3
1.2.1 Definitions and relationship to the elastic tensor.....	3
1.2.2 Seismological tools and techniques to measure seismic anisotropy.....	7
1.2.3 Formation mechanisms of seismic anisotropy in the Earth's Interior.....	9
1.2.4 Where is seismic anisotropy found inside the Earth?.....	11
1.2.5 Patterns of mantle flow, seismic anisotropy, and its interpretation for various tectonic settings.....	20
Chapter 2.....	25
Tectonic Setting.....	25
2.1 The Macquarie Ridge Complex.....	25
2.2 Previous shear-wave splitting studies along the Australian-Pacific plate boundary.....	31
Chapter 3.....	40
Methodology and Data.....	40
3.1 Methodology.....	40
3.1.1 The shear-wave splitting concept.....	40
3.1.2 Receiver-side versus source-side applications.....	41
3.1.3 Measurement methods: Rotation correlation and transverse component minimization.....	43
3.2 Processing steps in SplitLab.....	45
Chapter 4.....	51
Shear-wave splitting results along the Macquarie Ridge Complex.....	51
4.1 Receiver-side splitting analysis of the Macquarie Ridge Complex.....	51

4.2 Stations, events, and modifications for source-side splitting analysis of the Macquarie Ridge Complex .....	60
4.3 Acquiring additional stations suitable for source-side analysis at the MRC.....	64
4.4 Preliminary analysis of source-side splitting results .....	67
Chapter 5.....	72
Interpretation and Discussion.....	72
5.1 Potential sources of seismic anisotropy .....	72
5.2 Plate motion and upper mantle dynamics beneath the MRC .....	82
5.3 Local and regional variations along the MRC .....	85
Conclusion .....	90
Bibliography.....	93
Appendix.....	A1

# Chapter 1

## Introduction

### 1.1 Thesis Overview and Motivation

This thesis summarizes all of the research progress and achievements of the Master of Philosophy of Earth Sciences program of Mr. Haoran Du at the Australian National University, Research School of Earth Sciences from February, 2021 to August, 2023. The primary goal is to investigate seismic anisotropy beneath the Macquarie Ridge Complex (MRC) using shear-wave splitting methodologies. The research was conducted in connection to the Australian Research Council (ARC) Discovery Project (DP200101854) titled “*Probing the Australian-Pacific plate boundary: Macquarie Ridge in 3-D*”, led by Chief Investigator Hrvoje Tkalčić, Caroline Eakin, Mike Coffin, Nicholas Rawlinson, and Joann Stock.

The Macquarie Ridge Complex refers to the southeastern oceanic portion of the Australian-Pacific plate boundary, from the Puysegur Trench, south of South Island New Zealand to the sub-marine Australia-Pacific-Antarctica triple junction (Massell et al., 2000). The MRC is a region of immense geological and tectonic significance. It is one of the few examples where subduction initiation is taking place today (e.g., Stern, 2004), providing valuable insights on one of the biggest unsolved mysteries in plate tectonics, i.e., how subduction begins. Macquarie Island, located in the Southern Ocean along this plate boundary, has been designated a UNESCO World Heritage Site based on its geological significance. The island itself was once part of a mid-ocean ridge but now sits at an elevation of 410 m, representing the only ‘normal’ oceanic crust above

sea level situated in the ocean basin in which it formed (e.g., Griffin and Varne, 1980). In addition, the MRC is associated with some of the world's largest submarine earthquakes not associated with a subduction zone, including a M8.2 in 1989 and a M8.1 in 2004, raising questions as to how it is possible to generate such large magnitude earthquakes. Overall, the MRC was and continues to be a highly dynamic plate boundary, rapidly evolving from seafloor spreading, to trans-pressure and subduction initiation in recent geological history. Investigations that seek to better understand this plate boundary therefore hold great potential to further our understanding of plate boundary evolution and dynamics in general.

Despite its geological importance, the MRC is difficult to study, due to its remote location in the Southern Ocean, far away from land. Accessible seismic data recorded within this region is very limited, with only one permanent seismic station (station code: MCQ) deployed on Macquarie Island, along the entire MRC. However, the station has been operating for many years (since 2004) providing a long running dataset, and the plate boundary is seismically active both of which are ripe for exploitation by seismological means. One aspect that has largely been unexplored beneath the MRC is the nature and extent of seismic anisotropy. In the Earth's interior, seismic anisotropy is thought to develop primarily in the upper mantle as a result of deformation or flow (e.g., Long and Becker, 2010). Methods to detect and measure seismic anisotropy therefore provide one of the few routes to infer, or indirectly observe, the pattern of mantle flow and dynamics inside the Earth.

The aim of this study is therefore to shed light on the seismic anisotropy, and therefore the mantle dynamics beneath the Macquarie Ridge Complex. This is achieved via the analysis of shear-wave splitting, combining receiver-side and

source-side methods, to retrieve the key splitting parameters (i.e., the fast anisotropic direction,  $\phi$  and delay time,  $\delta t$ ). This allows for new constraints to be placed on the underlying anisotropic geometry, and inferences to be made on the upper mantle dynamics beneath the MRC in relation to the evolution of this enigmatic plate boundary.

## **1.2 Seismic anisotropy background**

### **1.2.1 Definitions and relationship to the elastic tensor**

In physics, the term “anisotropy” signifies that a physical property of the material varies in different directions. In seismology, the concept of “seismic anisotropy” refers to the variation in seismic wave velocity with direction (Karato, 2008; Long and Becker, 2010). Contrary to anisotropy is the term “isotropy”, in which a physical property of a material is uniform in all directions. The crystallographic structures of many typical minerals and/or materials that compose the Earth are anisotropic to seismic waves (see Table 1.1 for examples), and thus seismic anisotropy is a relatively common phenomenon.

Fundamentally, seismic anisotropy (and seismic velocity) relates to the relationship between stress and strain in a material. Stress is defined as the force exerted per unit area and strain is the physical change that results in response to that stress (Karato, 2008). For elastic deformation (instantaneous and recoverable deformation) of elastic solids, the elastic constants are utilized to describe the linear relationship between the stress,  $\sigma$ , and strain,  $\epsilon$ , and the anisotropy of elastic materials can be described mathematically by the elastic constants.

When the stress is low, then the strain,  $\epsilon$ , is a linear function of stress,  $\sigma$ , namely,

$$\sigma = M\varepsilon \quad (1.1)$$

where M is the elastic constant.

When we consider the elasticity of a crystal or seismic anisotropy in three dimensions, then the elastic properties of the medium are described in terms of the elastic tensor. In such a case, a general form of the stress-strain relationship is used, namely,

$$\sigma_{ij} = \sum_{kl} C_{ijkl} \varepsilon_{kl} \quad (1.2)$$

where  $C_{ijkl}$  is the elastic tensor, composed of the elastic constants that correspond to the physical properties in different directions.

For an isotropic material, there are only two modes of strain, namely volumetric and shear strain and the response of a material must be the same for all types of shear strain. Consequently, one can write,

$$\sigma_{ij} = \lambda \delta_{ij} \sum_k \varepsilon_{kk} + 2\mu \varepsilon_{ij} \quad (1.3)$$

in this equation, the elastic parameter,  $\lambda$  and shear modulus,  $\mu$ , are the Lamé constants. These two constants are enough to describe it completely. The  $\delta_{ij}$  is Kronecker's delta ( $\delta_{ij} = 1$  for  $i=j$ ,  $\delta_{ij} = 0$  for  $i \neq j$ ).

For anisotropic materials, we know the elastic constants should not change if suffices (ij) are interchanged with (kl). Also, from the symmetry of strain tensor ( $\sigma_{ij} = \sigma_{ji}$ ), one can show that the elastic constants remain unchanged when suffices (ij) are changed to (ji). Therefore,

$$C_{ijkl} = C_{klij} = C_{ijlk} = C_{jilk} \quad (1.4)$$

Because of this symmetry relationship (1.4), one can write the elastic tensor using two indices with Voigt notation. With this notation, the elastic tensor can be represented by a 6×6 matrix. From the symmetry relations it follows that

$$C_{ij} = C_{ji} \quad (1.5)$$

Because of this symmetry relationship, the number of independent elastic constants is at most 21. The number of independent elastic constants can be further reduced by the symmetry of a material. Some examples of the elastic tensor for different symmetry systems are presented below.

#### Isotropic (2)

$$\begin{bmatrix} C_{11} & C_{12} & C_{12} & 0 & 0 & 0 \\ C_{12} & C_{11} & C_{12} & 0 & 0 & 0 \\ C_{12} & C_{12} & C_{11} & 0 & 0 & 0 \\ 0 & 0 & 0 & \frac{1}{2}(C_{11}-C_{12}) & 0 & 0 \\ 0 & 0 & 0 & 0 & \frac{1}{2}(C_{11}-C_{12}) & 0 \\ 0 & 0 & 0 & 0 & 0 & \frac{1}{2}(C_{11}-C_{12}) \end{bmatrix}$$

#### Cubic (3)

$$\begin{bmatrix} C_{11} & C_{12} & C_{12} & 0 & 0 & 0 \\ C_{12} & C_{11} & C_{12} & 0 & 0 & 0 \\ C_{12} & C_{12} & C_{11} & 0 & 0 & 0 \\ 0 & 0 & 0 & C_{44} & 0 & 0 \\ 0 & 0 & 0 & 0 & C_{44} & 0 \\ 0 & 0 & 0 & 0 & 0 & C_{44} \end{bmatrix}$$

#### Hexagonal (5)

$$\begin{bmatrix} C_{11} & C_{12} & C_{13} & 0 & 0 & 0 \\ C_{12} & C_{11} & C_{13} & 0 & 0 & 0 \\ C_{13} & C_{13} & C_{33} & 0 & 0 & 0 \\ 0 & 0 & 0 & C_{44} & 0 & 0 \\ 0 & 0 & 0 & 0 & C_{44} & 0 \\ 0 & 0 & 0 & 0 & 0 & \frac{1}{2}(C_{11}-C_{12}) \end{bmatrix}$$



Orthorhombic (9)

$$\begin{bmatrix} C_{11} & C_{12} & C_{13} & 0 & 0 & 0 \\ C_{12} & C_{22} & C_{23} & 0 & 0 & 0 \\ C_{13} & C_{23} & C_{33} & 0 & 0 & 0 \\ 0 & 0 & 0 & C_{44} & 0 & 0 \\ 0 & 0 & 0 & 0 & C_{55} & 0 \\ 0 & 0 & 0 & 0 & 0 & C_{66} \end{bmatrix}$$

Figure 1.1 Elastic constants for some typical crystallographic symmetries of minerals or Earth's materials. The numbers in the parentheses correspond to the number of independent elastic constants respectively (Karato, 2008).

The intrinsic crystal structure of minerals and some Earth's materials can be classified based on the symmetry of the unit cell and the atomic arrangement within the unit cell. For the sake of illustration, we can see the number of independent elastic constants which are necessary for the description of the elastic tensor in different symmetry systems in the Table 1.1 below.

Table 1.1 Number of independent elastic constants for selected symmetry systems and typical minerals or Earth's materials from (Babuska and Cara, 1991).

Type of symmetry	Number of independent elastic constants	Typical mineral
triclinic	21	plagioclase
monoclinic	13	hornblende
orthorhombic	9	olivine
tetragonal	6	stishovite
trigonal I	7	ilmenite
trigonal II	6	quartz
hexagonal	5	ice
cubic	3	garnet
isotropic solid	2	volcanic glass

## 1.2.2 Seismological tools and techniques to measure seismic anisotropy

Observations of seismic anisotropy can be made by utilizing information from various types of seismic waveforms, from body-waves, to surface waves, to normal modes (e.g., Long and Becker, 2010), that span all layers of the Earth. For anisotropy of the Earth's mantle, typically shear-waves are most commonly utilized, either via shear-wave splitting of body wave phases (e.g., direct-S, Eakin et al., 2018; or SKS, Eakin et al., 2019), or via the analysis of surface waves (e.g., Rayleigh wave and Love wave, Gaherty, 2004). Alternatively, P-wave anisotropy is also a popular method, particularly in subduction zones where plentiful earthquakes are available to utilize (e.g., Huang and Zhao, 2021). Most methods typically constrain either the radial or azimuthal anisotropy. Radial anisotropy refers to a difference in propagation velocity between horizontally ( $V_{SH}$ ) and vertically polarized waves ( $V_{SV}$ ). Azimuthal anisotropy refers to a directional dependence of wave velocity with azimuth in the horizontal plane.

Of all the methods, shear wave splitting is perhaps the most popular for the characterization of seismic anisotropy. It is based on the premise that when a shear wave enters an anisotropic medium, it will be split into two components with orthogonal polarizations, one parallel to the fast direction of the anisotropic medium, and the other to the slow direction (Figure 2.1). A delay time is accumulated between the two components due to the difference in seismic velocity between the fast and slow orientations of the anisotropic medium. The two key parameters: (i) the fast polarization direction of the shear wave,  $\phi$ , and (ii) the delay time,  $\delta t$ , are primarily used to constrain the (i) geometry and (ii) the strength of the anisotropy depending on the path-length through the

anisotropic medium. For studies of mantle anisotropy, receiver-based methods are typically employed that target the anisotropic structure directly beneath the seismic receiver using core-refracted tele-seismic phases such as SKS, PKS, and SKKS (Barklage et al., 2009). In recent years, however, the source-side splitting method utilizing direct-S phases has become increasingly common (see further details in section 4.1.2), that allows for investigation of seismic anisotropy beneath the earthquake source, rather than beneath the receiver.

Additionally, surface waves are a very powerful tool for investigating large-scale anisotropic properties of the Earth's crust and upper mantle. There are two types of surface waves: Rayleigh waves and Love waves. Rayleigh waves are comprised of interfering P and Sv waves, and involve retrograde elliptical particle motion parallel to the direction of propagation. They are primarily sensitive to the velocity of vertically polarized shear waves ( $V_{SV}$ ). Love waves are comprised of  $S_H$  waves with particle motion perpendicular to the propagation direction. They are therefore sensitive to the velocity of horizontally polarized shear waves ( $V_{SH}$ ).

The depth of penetration of surface wave depends on the wavelength and the mode rank. For a given type of surface wave and for a given mode, the depth of penetration increases with the wavelength and consequently with the period. Long wavelength components (corresponding to long period and low frequency) are sensitive to the elastic properties of the deeper layers while short wavelength components (corresponding to short period and high frequency) are primarily sensitive to shallower layers. For this reason, surface waves will experience different velocities at different wavelengths (or periods, frequencies), due to the general increase in seismic velocity with depth inside the Earth, leading to dispersion of the seismic signal. Based on phase or group velocity measurements of the discrepancy between Rayleigh and Love wave

dispersions, the anisotropic structure can be constrained in terms of radial and/or azimuthal anisotropy (Montagner, 1985; Babuska and Cara, 1991; Gaherty, 2004).

In general, investigations of seismic anisotropy from body waves (e.g., shear-wave splitting) tend to have better lateral resolution than surface waves, which will tend to average over any variations in lateral structure. Shear-wave splitting techniques using teleseismic phases, such as SKS, SKKS and PKS, however, are sensitive to anisotropy present anywhere along the ray-path between the core-mantle boundary and the surface, leading to uncertainty in the depth of the anisotropy source (Vinnik et al., 1992; Silver, 1996). On the other hand, due to their dispersion behavior, analyses from surface waves can provide some information on depth dependence of seismic anisotropy (Montagner and Jobert, 1988; Montagner and Tanimoto, 1990; Montagner and Tanimoto, 1991).

### **1.2.3 Formation mechanisms of seismic anisotropy in the Earth's Interior**

In order to infer the flow geometry and dynamic processes occurring in the mantle, it is essential to understand the relationship between the mantle deformation and seismic anisotropy. Microscopically, lattice preferred orientation (LPO), or crystallographic preferred orientation, (CPO) of individual anisotropic minerals can lead to bulk seismic anisotropy that is observable with seismic waves (Karato, 2008; Long and Becker, 2010).

LPO refers to the non-random distribution of crystallographic orientations and is one of the most important microstructural characteristics of rocks (Karato, 2008). The LPO of a rock can provide essential information about the physical processes by which a rock was formed and/or has been deformed in a given

environment. Therefore, LPO is a manifestation of deformation conditions, and one can further infer the dynamic processes corresponding to such conditions in the Earth's interior, such as the flow pattern in the mantle (Karato, 2008).

Deformation of the Earth's viscous mantle is accommodated via two main processes, dislocation creep and diffusion creep, but only dislocation creep is thought to generate LPO. Dislocation creep is a deformation mechanism in crystalline materials, and involves the movement of dislocations through the crystal lattice of the material. It causes plastic deformation of the individual crystals, and thus the material itself. Dislocation creep is highly sensitive to the differential stress on the material, and it is thought to occur at the relatively high stress, large grain size and low temperature conditions (Karato, 2008).

Depending on the physical conditions inside the Earth's interior, diffusional creep can also dominate. Diffusion creep refers to the deformation of crystalline solids by the diffusion of vacancies through their crystal lattice, it usually results in plastic deformation rather than brittle failure of the material. Diffusion creep is an important mechanism of plastic deformation in a polycrystalline material at relatively high temperatures, low stress and small grain size (Karato, 2008). At high temperatures, atoms move from their stable positions with some probability due to thermally activated processes, this is referred to as diffusion.

Due to the different physical conditions present inside the Earth, dislocation creep, and therefore the generation of LPO, is thought to be limited to regions of high strain rate such as the asthenosphere. For most of the mantle however, diffusion creep should dominate.

Alternatively, bulk seismic anisotropy inside the Earth may be the result of shape preferred orientation (SPO), rather than LPO. SPO is generated by

layering of two or more isotropic or anisotropic materials. It is usually associated with the alignment of material with distinct isotropic elastic properties (contrasting with the surrounding matrix). Such examples include aligned the pattern of cracks in the upper crust (e.g., Greve and Savage, 2009), or SPO of small scale inclusions such as horizontally distributed disks of partial melt in the D" region (Moore et al., 2004).

#### **1.2.4 Where is seismic anisotropy found inside the Earth?**

Seismic anisotropy can be found in many parts of the Earth, albeit with varying contributions. In the below sections, the presence of anisotropy and the likely mechanisms which produce it, are outlined for the primary layers of the Earth from top to bottom.

##### **1.2.4.1 Crust**

Although relatively thin compared to other layers of the Earth, the crust is often found to display seismic anisotropy (Mainprice and Nicolas, 1989; Zhang and Schwartz, 1994). The anisotropic structure of the crust is mainly thought to originate from SPO, associated with the alignment of materials with distinct isotropic elastic properties, such as fluid-filled cracks in the crust (e.g., Crampin, 1994). Deformation of the crust occurs mostly by brittle fracture in its shallow part (e.g., continental upper crust) and by ductile deformation in the deeper part (e.g., continental lower crust; Mainprice and Nicolas, 1989). Consequently, the most important anisotropic structure in the shallow crust is from aligned cracks (SPO).

The lower crust is thought to be able to undergo deformation by plastic and viscous deformation, allowing for lower crustal ductile flow. The existence of strong LPOs is found in the main rock-forming minerals of the lower crust, and

these minerals can be extremely seismically anisotropic (Mainprice and Nicolas, 1989).

Most of the plastically deformed crustal rocks show significant LPO and have some degree of elastic anisotropy. However, the anisotropic layer in the crust is thin (compared to the mantle) and the anisotropic structure is not always persistent at a large scale. Consequently, the total contribution of seismic anisotropy from the crust is relatively small compared to the upper mantle.

#### **1.2.4.2 Lithospheric mantle**

Seismic anisotropy of the subcrustal oceanic lithosphere has been detected by many independent observations. It is generally found that seismic waves travel fastest in the orientation parallel to the paleo or present spreading direction (i.e., perpendicular to the strike of the mid-ocean ridge at which the lithosphere formed). Such observations have been made in various regions of the Pacific Ocean (Morris et al., 1969; Raitt et al., 1969; Keen and Barrett, 1971; Shor et al., 1973; Snyderman et al., 1975; Malecek and Clowes, 1978; Shimamura et al., 1983; Shearer and Orcutt, 1985; Wolfe and Solomon, 1998; Harmon et al., 2004) and the Indian Ocean (Shor et al., 1973). The anisotropic pattern is thought to be caused by the frozen-in preferred orientation of olivine crystals, resulting from shear parallel to the spreading direction beneath the base of the newly-forming oceanic lithosphere.

For continental lithosphere, similarly the frozen-in preferred orientation of olivine crystals is generally accepted as the principal cause of any observed seismic anisotropy (Babuška et al., 1993). However, the generation of such frozen-in fabrics are thought to represent past episodes of significant tectonic deformation, such as orogenic events (e.g., Silver and Chan, 1991).

### 1.2.4.3 Asthenospheric mantle

Seismic anisotropy in the asthenospheric mantle is in most cases attributed to the LPO of anisotropic minerals particularly that of olivine. Olivine is the volumetrically dominant mineral and has a large single-crystal anisotropy (~18% for shear waves; e.g., Mainprice, 2007). When the deformation of an aggregate of olivine in simple shear occurs in the dislocation creep regime, it will produce an LPO, and the strength of LPO will increase with increasing strain until it saturates at a relatively modest amount of strain (~100-150%, e.g., Karato et al., 2008).

Table 2.2 Relationship between the olivine LPO fabric and the dominant slip systems from Karato et al., (2008).

A-type	B-type	C-type	D-type	E-type
[100](010)	[001](010)	[001](100)	[100]{0kl}	[100](001)

Technically speaking, the relationship between mantle flow and the anisotropic geometry generated is not uniform, because it also depends on the LPO fabric type of olivine. The most common interpretation (Nicolas and Christensen, 1987; Ben Ismail and Mainprice, 1998), is that the anisotropy detected is due mainly to A-type olivine fabric. A-type fabrics, dominate at modest stress and temperature conditions, and are associated with dominant slip in the [100] direction on the (010) plane (Karato et al., 2008). The fast axes of olivine crystals developed by A-type olivine LPO tend to align in the direction of maximum shear. When we consider the case of vertically propagating waves, such as direct-S, SKS, SKKS or PKS within the appropriate epicentral distances, this implies that the seismic fast direction should be parallel to the flow direction, assuming flow of the upper mantle in the horizontal plane.



However, the development of olivine LPO can be more complicated considering that there are a variety of olivine fabric types (A-, B-, C-, D- and E-type) possible. These have been identified both in the laboratory and from the naturally deformed peridotites (Ben Ismail and Mainprice, 1998; Mainprice et al., 2000). Different fabric types form under the influence of varying physical and chemical conditions including stress, temperature and water content (Zhang and Karato, 1995; Bystricky et al., 2001; Jung and Karato, 2001; Jung et al., 2006; Katayama and Karato, 2006) and possibly due to changes in pressure (Mainprice et al., 2005; Jung et al., 2009). Each olivine fabric type is associated with distinct dominant slip systems and resulting anisotropic geometries as presented in Table 2.2, Figure 2.1 and Figure 2.2.

The relationship between the different deformation fabrics of olivine and various conditions of water content and stress is best illustrated by Figure 1.1 below. As can be seen from the figure, A-type fabric is thought to dominate under dry upper mantle conditions at moderate levels of stress, while C-type and E-type may be more common under hydrated upper mantle conditions. Under high-stress conditions, B-type fabric is more likely to dominate, except under dry (low water contents) in which case D-type is more likely.

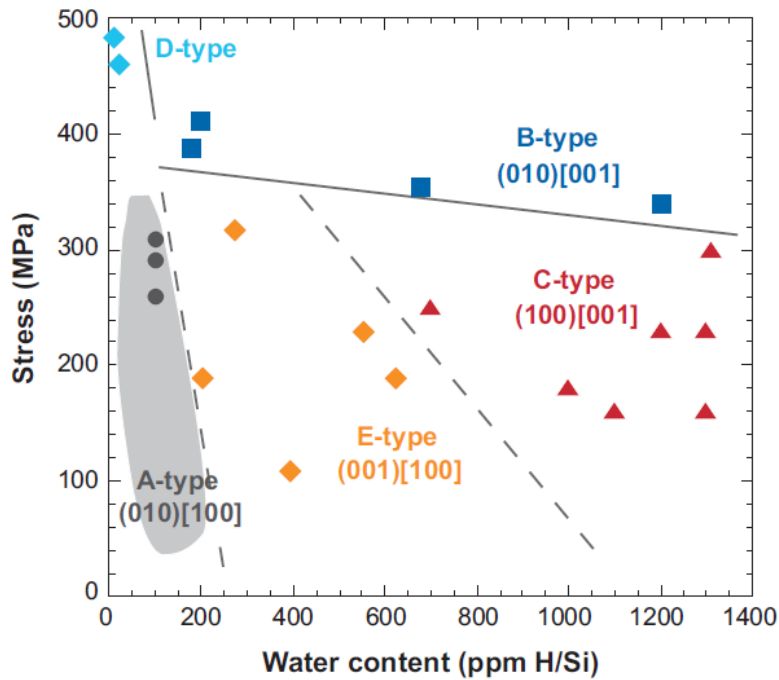


Figure 1.1 Deformation fabrics of olivine at high temperatures ( $T \sim 1470\text{-}1570\text{ K}$ ) as a function of water content and stress, taken from Karato et al., (2008).

As the deformation conditions change and the corresponding olivine LPO fabrics change, the correspondence between the orientation of the olivine crystallographic axes (i.e. [100] a-axis, [010] b-axis, [001] c-axis) and the shear direction and the shear plane will also change (Figure 1.2). For example, under low stress and water-poor conditions associated with A-type fabric, the fast [100] a-axis of olivine is subparallel to the shear direction, while the (010) plane is subparallel to the shear plane. When under relatively high stress and a range of water contents associated with B-type fabric, the olivine [001] c-axis is subparallel to the shear direction, and the (010) plane is subparallel to the shear plane. In this case, the fast axes of olivine [100] tend to align  $90^\circ$  from the maximum shear direction in the shear plane, so the fast direction from seismological observations, such as shear-wave splitting, would be perpendicular to the mantle flow direction.

At high temperatures and low stresses, the dominant fabric type is expected to change from A-type to E-type, and then C-type as the water content increases. The possible influence of pressure is still being investigated experimentally. A-type or D-type may volumetrically important in the mantle lithosphere, while A-, C- or E-type fabric may dominate in the asthenosphere (Karato et al., 2008). For typical upper mantle conditions however, whether A-, C-, or E-type fabrics dominate, the fast orientation in horizontal plane will still be parallel to the shear direction (Long and Becker, 2010). B-type fabric however, where such a relationship with the shear direction is changed, is thought to be limited to the cold corner of the subduction mantle wedge, where stresses are high and temperatures are relatively low (e.g., Kneller et al., 2005).

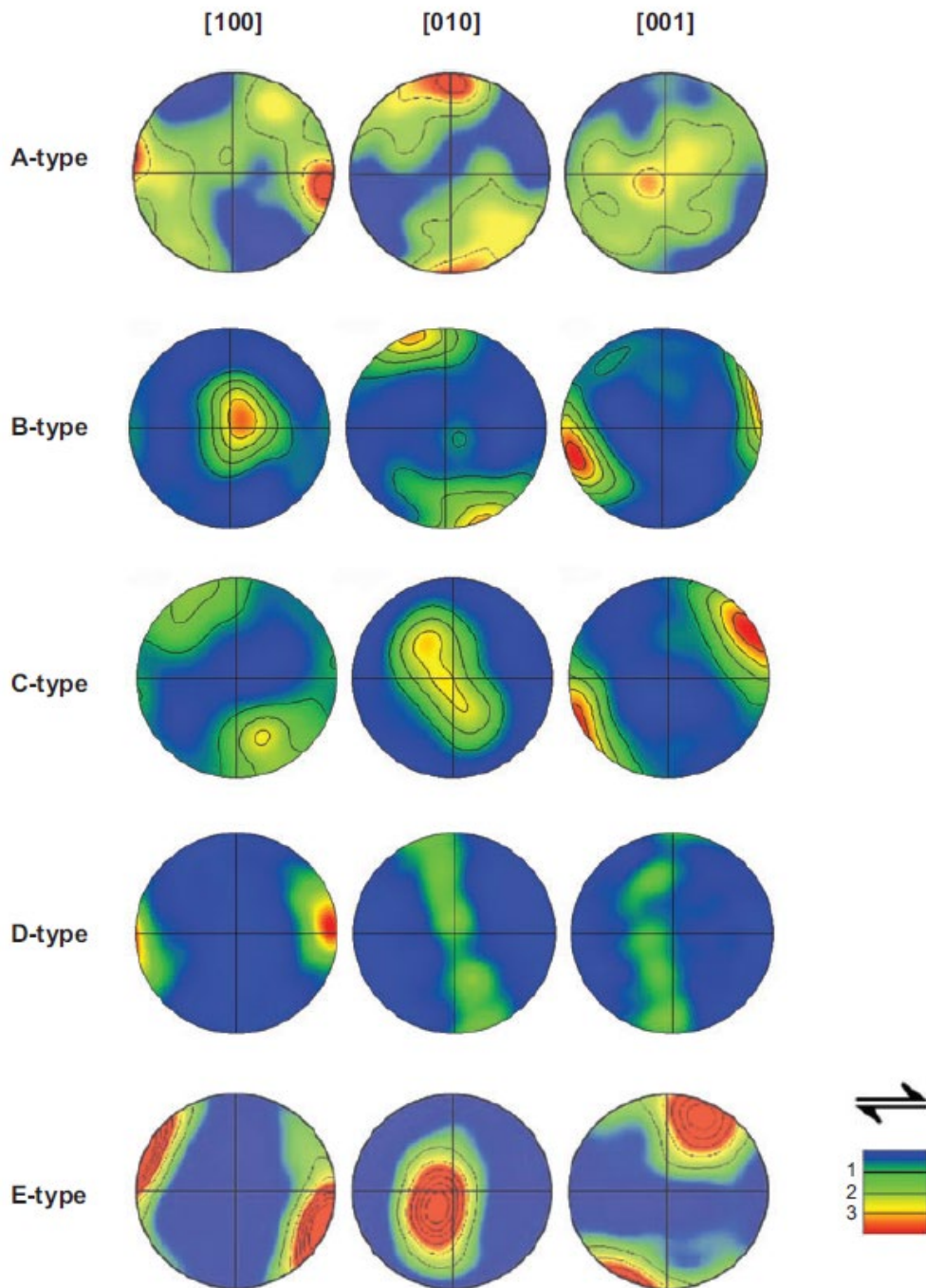


Figure 1.2 Typical olivine textures for the different olivine LPO fabric types found in the simple shear deformation experiments. The figure is taken from Karato et al., (2008), modified after Jung et al., (2006). The pole figures show the LPO of olivine (A-, B-, C-, D- and E-type). The pole figures are presented in the lower hemisphere using an equal area projection. The sense of shear is represented by the arrows on the right corner. The north (south) poles correspond to the normal to the shear plane. The colors indicate the density

of data points and contours correspond to multiples of uniform distribution.

To summarize, for the relationship between the crystallographic fast axes with upper mantle flow, under the assumption of horizontally orientated flow, such as that induced by plate motions, all-types of olivine LPO fabric except for B-type would produce fast directions (e.g., from shear-wave splitting) that are parallel to the flow direction for vertically incident seismic waves, such as SKS or PKS. For the same geometry but B-type, the fast direction would be perpendicular to the flow direction.

#### **1.2.4.4 Transition zone**

The nature of anisotropy in the transition zone is poorly understood at present, as the nature of LPO of minerals in the transition zone is relatively unknown. A previous shear-wave splitting study conducted by Fischer and Wiens, (1996), suggested that weak anisotropy exists in the transition zone beneath the Tonga back-arc, but the resolution of these studies is not high. In some subsequent studies, Montagner and Kennett (1996) found evidence for  $S_H$ - $S_V$  polarization anisotropy in the transition zone. The studies of Vinnik and Montagner (1996) and Trampert and Van Heijst (2002) also reported azimuthal anisotropy in the transition zone, distinct from that of the upper mantle.

In this layer, a volumetrically important mineral that has a large single crystal anisotropy is wadsleyite, which is present in the upper transition zone (~ 410-550 km, Karato, 2008). However, significant alignment of wadsleyite crystals due to LPO under typical conditions of the transition zone is not expected to occur, as dislocation creep is not expected at this depth. In the lower transition zone, the volumetrically important minerals are ringwoodite and majorite, which are both elastically isotropic and therefore not expected to contribute to seismic

anisotropy (Karato, 2008).

#### **1.2.4.5 Lower mantle and D'' layer**

The majority of the lower mantle is thought to be devoid of seismic anisotropy, determined observationally from the analysis of Earth's free oscillations (Montagner and Kennett, 1996). The most likely explanation for the lack of anisotropy is that lower mantle minerals deform by diffusional creep (or superplasticity; Karato et al., 1995).

However, the lowermost layer of the mantle, just above the core-mantle boundary, called the D'' layer, is believed to have significant anisotropy (Kendall and Silver, 1996; Montagner and Kennett, 1996). This is associated with the dynamics of mantle convection and the general nature of deformation mechanisms in polycrystalline aggregates. The D'' layer is possibly a boundary layer of the convecting mantle and therefore deformation probably occurs at higher stress and strain than elsewhere in the lower mantle (Karato, 2008). Considering the concept that LPO develops only at high stress, then the localized distribution of anisotropy in the D'' layer can be attributed to the stress-strain distribution and the associated change in deformation mechanisms (Karato, 1998).

Alternatively, SPO has often been invoked as a mechanism for generating anisotropy in D'' layer, however this relies on the presence of a material in the lowermost mantle with elastic properties that significantly contrast with the surrounding matrix (Long and Silver, 2009). This could take the form of partial melt, which is often invoked as the cause of that ultra-low velocity zones (ULVZs) that are intermittently observed at the base of the mantle (Russell et al., 1998). Others have proposed compositionally distinct subducted materials that have

made their way to the CMB (Kendall and Silver, 1996), or infiltrated iron from the core (Kendall and Silver, 1996; Kendall and Silver, 1998).

## **1.2.5 Patterns of mantle flow, seismic anisotropy, and its interpretation for various tectonic settings**

### **1.2.5.1 Ocean basins**

Of all the tectonic settings on Earth, seismic anisotropy beneath ocean basins is perhaps the simplest. In general, fast directions in the asthenosphere largely align with present day plate motion, while fast directions in the lithosphere appear to align with the paleo-spreading direction (e.g., Debayle and Ricard, 2013). Such relationships have aided our fundamental understanding of the lithosphere-asthenosphere system and the nature of plate-mantle coupling. Assuming an A-type olivine fabric, there appears to be a successful match between global modeling of plate motions and density heterogeneities at depth with seismic anisotropy observations from shear wave splitting and surface waves (Becker et al., 2003; Maggi et al., 2006; Conrad et al., 2007). This suggests that the traditional relationship between strain and anisotropy from the classic model (Nicolas and Christensen, 1987; Ben Ismail and Mainprice, 1998) is the correct one for interpreting observations of seismic anisotropy beneath ocean basins.

Although shear wave splitting constraints in ocean basins are sparse, the measurement and interpretation of splitting in this simple tectonic regime is very important to our understanding of how to relate splitting observations to mantle flow.

### **1.2.5.2 Mid-ocean ridges**

Shear-wave splitting studies from mid-ocean ridge settings are very limited. Previous studies by Wolfe and Solomon (1998) and Harmon et al., (2004) demonstrated fast directions in the vicinity of mid-ocean ridges which were oriented approximately parallel to the spreading direction (i.e., perpendicular to the strike of the ridge), with variable delay time. The observed pattern of fast directions is generally consistent with anisotropy controlled by olivine alignment in a 2-D corner flow field, but contrary to the predictions made by a model in which anisotropy is controlled by vertically aligned melt-filled cracks, which would predict ridge-parallel fast directions close to the ridge.

Although the availability of splitting constraints from mid-ocean ridges is limited, the available data suggest that mantle flow beneath ridges (and the associated upper mantle anisotropy) generally conforms to the expectations of a simple, 2-D corner flow-type model.

### **1.2.5.3 Continents**

In general, seismic anisotropy in continental regions is considered much more complex compared to that beneath the oceans. This is because both the lithosphere and the asthenosphere will contribute to the anisotropy detected, but the continental lithosphere is generally thicker than the oceanic, and the lithospheric component shows strong spatial variability (e.g., Silver, 1996; Savage, 1999; Fouch and Rondenay, 2006). This may lead to complex multi-layered anisotropy both beneath and within continents (e.g., Fouch and Rondenay, 2006; Yuan and Romanowicz, 2010). Continental lithosphere is also much older than oceanic lithosphere. Seismic anisotropy within the oldest cratonic lithosphere is often shown to align with past tectonic/surface features



such as orogenic belts, suture zones, and geophysical signatures (e.g., gravity and magnetic lineaments) preserved in the crust (e.g., Silver, 1996; Eakin et al., 2021). Such similarities imply that the continental lithosphere holds significant frozen-in or fossilized anisotropy as a result of past tectonic events that deformed the lithosphere. In addition, the pattern of anisotropy existing within present-day continental orogens has been shown to reflect current surface deformation, such as in Tibetan Plateau (e.g., McNamara et al., 1994).

#### **1.2.5.4 Subduction zones**

Subduction zones are among the most complicated tectonic settings on Earth. Subduction zone dynamics is regarded as a key to understanding the interaction between surface structures and the deep mantle, and so they have been the target of plenty of seismic anisotropy studies (e.g., Ando et al., 1983; Fukao, 1984; Bowman and Ando, 1987; Long and Silver, 2008). However, observations from shear-wave splitting vary a lot in subduction zones from fast directions parallel or normal to the strike of the trench, to substantial lateral heterogeneity, and a large range in delay times from 0 s to greater than 2 s (Long and Silver, 2008).

Within a subduction zone, there are four potential source regions of anisotropy: the sub-slab mantle, the slab itself, the mantle wedge, and the overlying plate. This complexity makes it difficult to resolve where in the system the anisotropy is originating from seismic observations, and harder to construct the suitable numerical models to correspond to the observations.

A variety of flow models around subduction zones have been proposed to interpret anisotropy observations globally, with the most classical among them characterized by corner flow above the slab and entrained flow beneath the

slab (e.g., Hall et al., 2000). Assuming A-type (or similar) olivine fabric, such models predict trench-perpendicular fast directions in both the mantle wedge and below the slab, however this cannot account for the variability of anisotropic observations seen. Alternative interpretations include trench-parallel flow in the mantle wedge (Smith et al., 2001) or beneath the subducting slab (Russo and Silver, 1994), flow induced by crustal foundering (Behn et al., 2007), and transpression due to oblique subduction (Mehl et al., 2003). From the perspective of fabric type, it is also proposed that a change in the olivine LPO fabric from A-type to B-type could explain trench-parallel fast direction observations (Nakajima and Hasegawa, 2004; Kneller et al., 2005; Long et al., 2007). The mantle wedge conditions with relatively high stress and low temperatures, and some water content, make it possible for the generation of the B-type olivine fabric, but the A-, C-, or E-types, with the traditional strain-anisotropy correspondence relationship, are more likely to dominate in the other parts of the upper mantle. Any of these models can be successful in accounting for anisotropy observations of local regions, but none of them give a common answer to the splitting behavior of subduction zones all around the world.

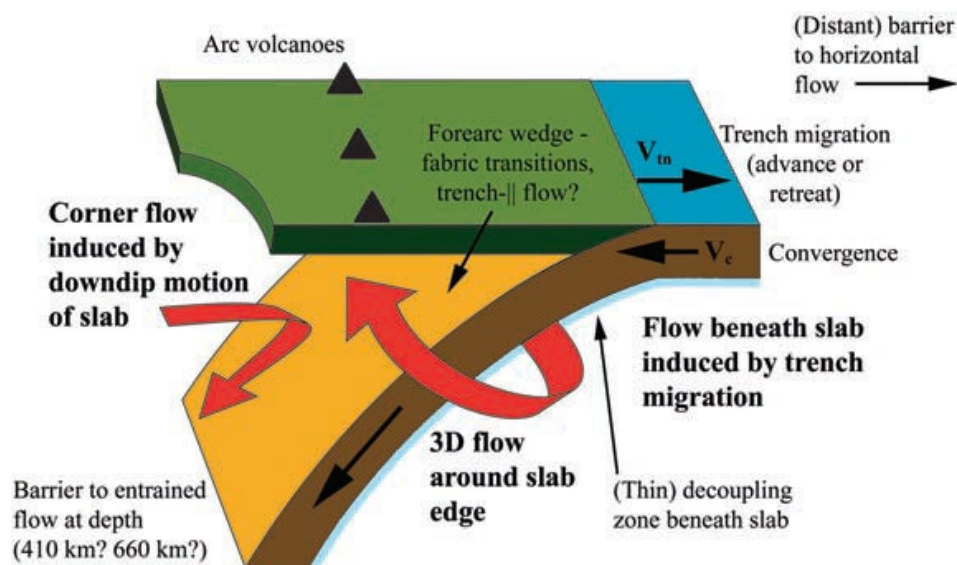


Figure 1.3 Schematic diagram of the subduction zone model proposed in and taken from

Long and Silver, (2008), showing the dominance of 3D flow beneath the slab and the competing influence of 2D and 3D flow fields in the mantle wedge.

In a review of shear-wave splitting studies targeted on 13 subduction zones globally, Long and Silver (2008), isolated the wedge and sub-wedge components of the splitting signals and examined parameters such as, convergence velocity, trench migration velocity, age of subducting lithosphere, and the stress state of the overriding plate. They concluded that sub-wedge anisotropy is primarily controlled by the 3D return flow (Figure 1.3). While for the wedge anisotropy, the convergence velocity ( $V_c$ ) and the magnitude of trench migration velocity ( $|V_t|$ ) should govern the strength of the 2D corner flow and 3D trench-parallel flow (Figure 2.2), respectively. Their ratio ( $V_{norm}=|V_t|/ V_c$ ) is a measure of the relative importance of these two models of flow field in a subduction zone.

# Chapter 2

## Tectonic Setting

### 2.1 The Macquarie Ridge Complex

The Macquarie Ridge Complex (MRC) refers to the southeastern oceanic portion of the Australian-Pacific plate boundary, from the Puysegur Trench, south of the South Island New Zealand to the submarine Australia-Pacific-Antarctica triple junction. From north to south, it is composed of four main regions: Puysegur region, McDougall region, Macquarie region (which includes Macquarie Island) and Hjort region (Figure 2.1). Studies suggest that previously the Macquarie Ridge Complex was a divergent plate boundary with oceanic crust produced along the spreading center as recently as 10 million years ago (Duncan and Varne, 1988; Massell et al., 2000). Today, the plate boundary classifications change along the length of the MRC (Ruff et al., 1989; Massell et al., 2000; Hayes et al., 2009; Figure 2.1). The McDougall and Macquarie segments can be described as a right-lateral strike-slip plate boundary with both shear and compressional motions (i.e., trans-pressure) between the two plates. For the Puysegur and Hjort segments, there is increased convergence and potential evidence for subduction initiation.

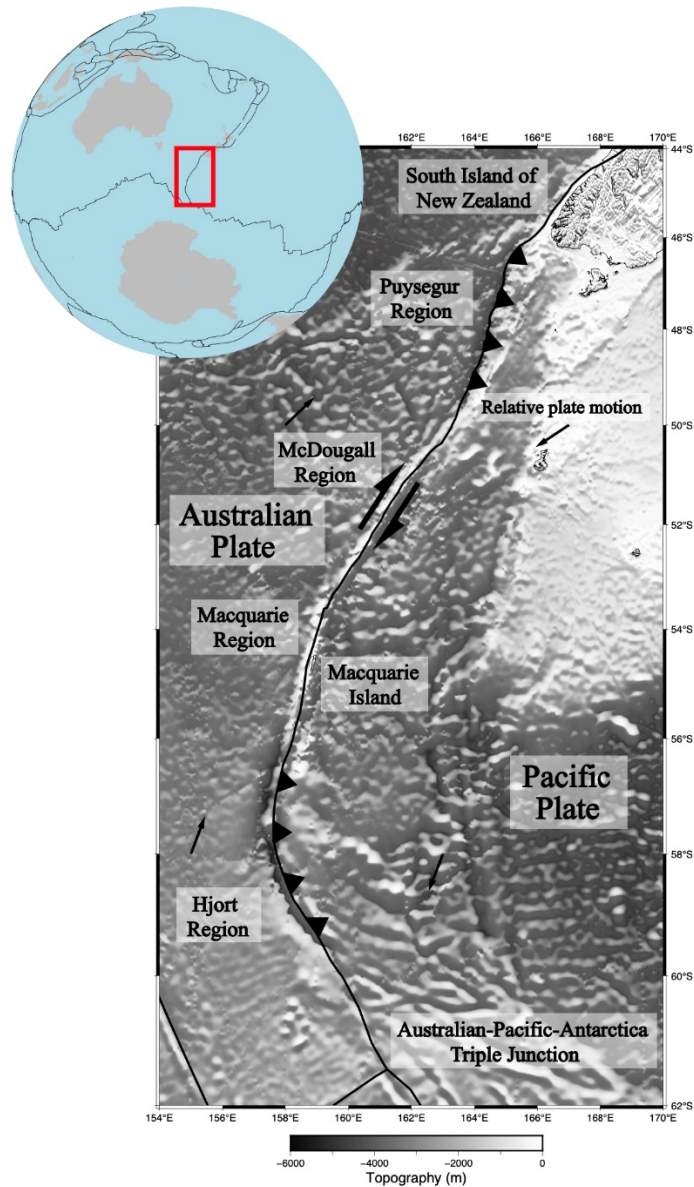


Figure 2.1 Map of the Macquarie Ridge Complex (MRC), illustrating the main surface structural features in the area. The global map in the upper left corner shows the location of the Macquarie Ridge Complex relative to Australia and Antarctica. The black triangles along the plate boundary indicate locations of convergence and inferred direction of subduction. The large black half-arrows shown close on the plate boundary indicate the direction of shear between the Australian and Pacific plates. The thin black arrows indicate the relative plate motion between Australian and Pacific plates in those locations.

A formative study by Massell et al. (2000) conducted a comprehensive

geophysical exploration of this area presenting a clear description of the plate boundary character along strike. This was based on various marine geophysical data collected including side scan, bathymetry, seismic reflection, plate motion vectors, and teleseismic recordings. They indicated the dominant role of the present-day strike-slip motion along the whole section of the plate boundary, and that the boundary is consistent with the relicts of a spreading center for the Australian-Pacific crust in the region. They also found relicts of fracture zones in the seafloor bathymetry showing an arcuate shape (Figure 2.2), and becoming asymptotic as approaching the plate boundary. This arcuate shape provides a record of the evolution of the plate boundary through time, from seafloor spreading to trans-pressure due to migration of the Euler pole and rotation of the relative plate motions.

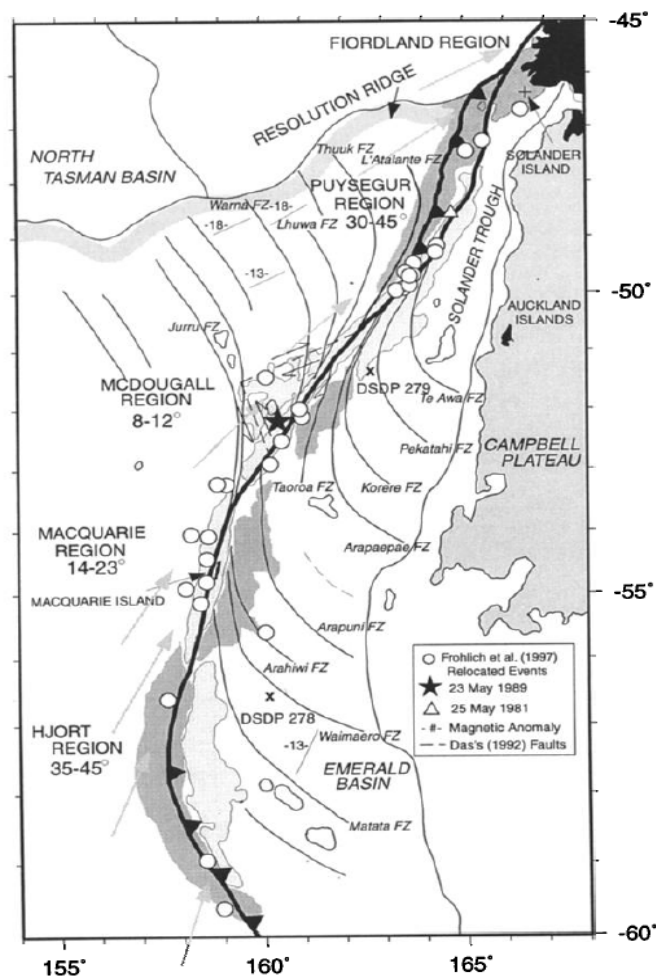


Figure 2.2 Map of the MRC taken from Massell et al., (2000), showing the structural features on the seafloor. The thick solid lines represent the plate boundary between the Australian and Pacific plate, and the thin solid lines represent the relicts of fracture zones in the area.

Evidence of under-thrusting is not found at the McDougall and southernmost Puysegur segments, while data from the Macquarie and Hjort regions strongly suggest convergence in the recent geological past (Massell et al., 2000). The study of Hayes et al. (2009) using relocated seismicity and plate boundary reconstructions suggested deformation of the Puysegur Block, and that region of the plate boundary evolved over the past ~25 Ma from divergence to translation to incipient subduction of the Australian Plate at the Puysegur Trench happening today.

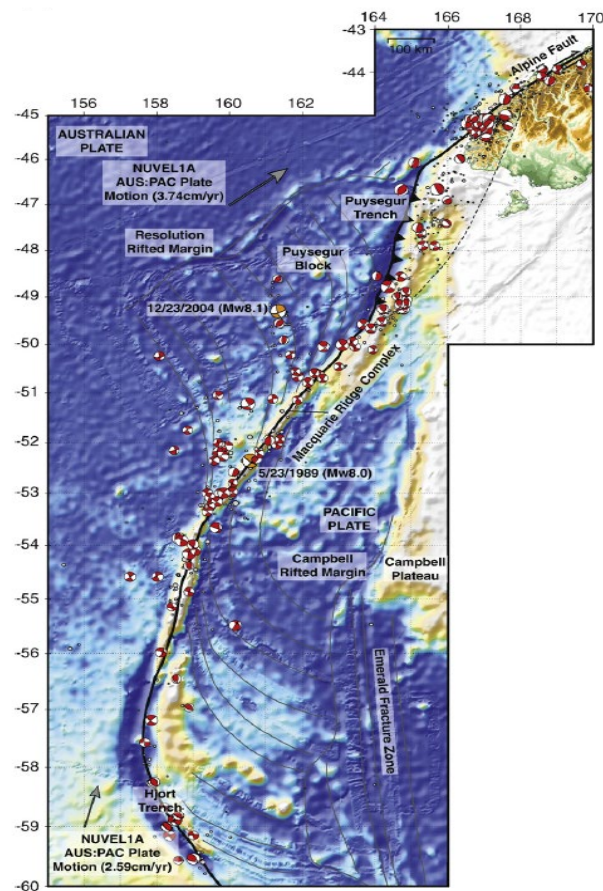


Figure 2.3 Map showing the distribution of events at the MRC taken from Hayes et al., (2009). The beach balls plotted in red represent the location of earthquakes recorded along the MRC. Most of them indicate focal mechanisms that are strike-slip. The two beach balls plotted in orange represent the location of two great earthquakes (M8+) that occurred in the vicinity of the MRC, one of which occurred on a fracture zone off the plate boundary, and the other directly on the plate boundary.

The high seismicity of the MRC makes it attractive for seismology studies. Many unusually large earthquakes, including two 8.0+ strike-slip events (23 May, 1989, Mw 8.0 and 23 December, 2004, Mw 8.1), have occurred at or off the plate boundary of the MRC and recorded by modern seismic instruments (Ruff et al., 1989; Ruff, 1990; Das, 1992 & 1993; Frohlich et al., 1997; Kennett et al., 2004; Figure 2.3). In general, the epicenters of most of the earthquakes are located close to the plate boundary and appear to be relatively shallow (depths < 35 km). Most show strike-slip focal mechanisms except for a few thrust mechanisms at the Puysegur and Hjort segments. This constitutes the primary evidence for transform motion dominating along the plate boundary with a component of under-thrusting at the Puysegur Trench (Ruff et al., 1989; Ruff, 1990; Das, 1992 & 1993; Frohlich et al., 1997; Kennett et al., 2004). Although the two large earthquakes occurred at the plate boundary, the aftershock relocation study conducted by Das (1992, 1993) shows that the aftershocks of 1989 earthquake were primarily distributed along a 220 km portion of the plate boundary, and that the earthquake reactivated a 175 km section of a fault to its west. Another study by Kennett et al., (2004) tracking the 2004 earthquake source evolution, based on the high-frequency radiation utilized estimation of the location of energy emission, found the event rupture was on two close fault systems reactivating former fracture zones. They concluded this composite fault behavior may be a characteristic for this kind of large intraplate events. Another study of focal mechanisms by Frohlich et al. (1997) indicated that the



present-day motion along most of the MRC is strike-slip, although diversity exists at the northern end of the MRC. They also speculated that for strike-slip boundaries, like the MRC and the San Andreas Fault in North America, the very largest earthquakes usually occur on the primary plate boundary fault but other large events can occur along pre-existing zones of weakness away from the plate boundary.

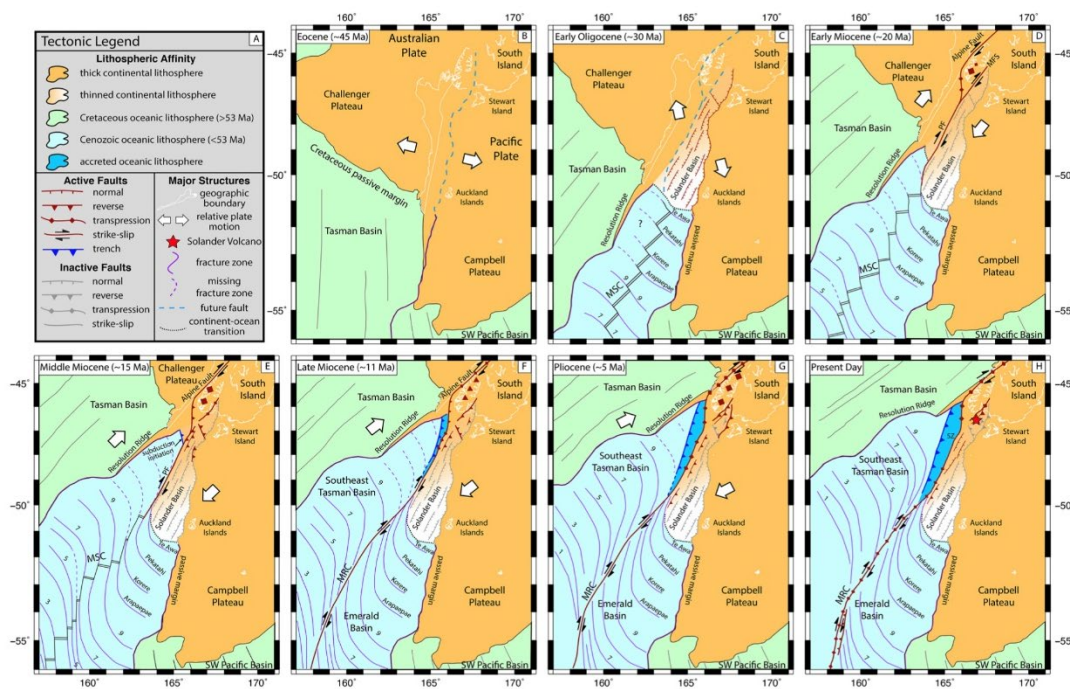


Figure 2.4 Map illustrating a proposed evolution of the MRC taken from Shuck et al., (2021), as modified from Lebrun et al., (2003).

Conceptual geodynamical models constructed by previous studies (Massell et al., 2000; Lebrun et al., 2003; Shuck et al., 2021) indicate the evolution process of the MRC from Eocene (~ 45 Ma) to the present. Such models propose the MRC, including the segments south of New Zealand, underwent an evolution from seafloor spreading to a rotation of the relative plate motions, to dextral strike-slip, trans-pressure (co-existence of compression and transform), and subduction initiation in the north, as seen at present (Figure 2.4). In the

conceptual model of Massell et al., (2000), they gave the explanation of decreasing length of the spreading center segments and spacing between fracture zones, as well as the arcuate bend of the fracture zones that become asymptotic to the current transform plate boundary. In the conceptual models of the Lebrun et al., (2003) and Shuck et al., (2021), they focused more on the dynamical factors and tectonic inheritance that influenced a divergent plate boundary to evolve towards favorable conditions for subduction initiation.

## **2.2 Previous shear-wave splitting studies along the Australian-Pacific plate boundary**

The Australian-Pacific plate boundary extends more than 12,400 kilometers encompassing the northern and eastern boundary of the Australian plate (Figure 2.5). It is part of the “Pacific Ring of Fire” with plentiful volcanoes and earthquakes. The Australian-Pacific plate boundary exhibits various plate boundary types, including subduction (such as the New Britain Trench, the New Hebrides Trench and the Tonga-Kermadec Trench), strike-slip faulting (such as the Alpine Fault) and trans-pressional-style plate boundary (such as the MRC).

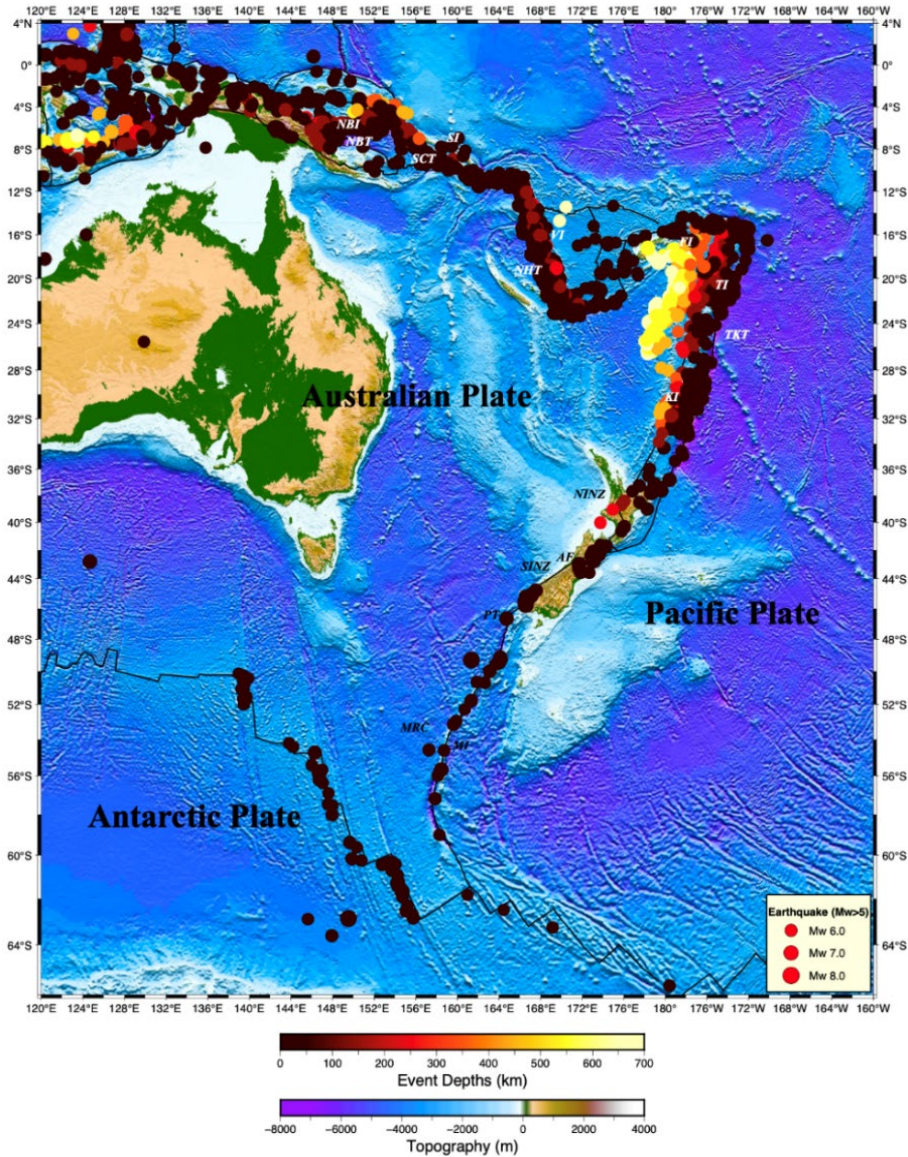


Figure 2.5 Map of events along the eastern Australian-Pacific plate boundary from 1990 to 2021 with magnitudes larger than 6.0. The coloured circles correspond to event depth. Abbreviations of corresponding geological features in the figure are as follows: NBT, New Britain Trench; NBI, New Britain Islands; SCT, San Cristobal Trench; SI, Solomon Islands; NHT, New Hebrides Trench; VI, Vanuatu Islands; FI, Fiji Islands; TI, Tonga Islands; KI, Kermadec Islands; TKT, Tonga-Kermadec Trench; NINZ, North Island of New Zealand; SINZ, South Island of New Zealand; AF, Alpine Fault; PT, Puysegur Trench; MRC, Macquarie Ridge Complex; MI, Macquarie Island.



Along the Australian-Pacific plate boundary, there are nearly 540 earthquakes larger than magnitude 5.0 every year on average and 18 earthquakes of magnitude 8.0 or higher in the past one hundred years according to the USGS catalogue (<https://www.usgs.gov/natural-hazards/earthquake-hazards/earthquakes>). We can see that the seismicity of the MRC is very high, with most of the earthquakes occurring here close to the plate boundary, and with relatively shallow depths.

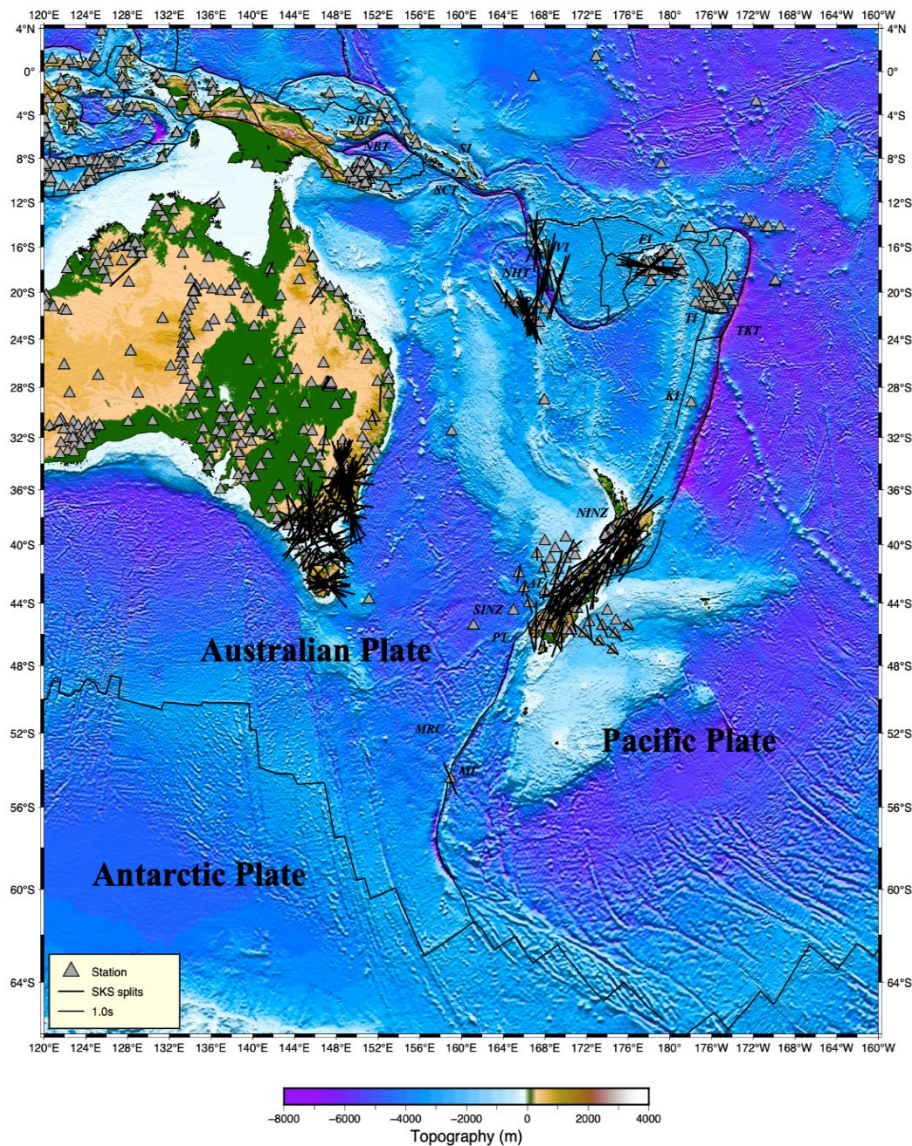


Figure 2.6 Map indicating the availability of broadband seismic stations (grey triangles) throughout the region and corresponding receiver-side (e.g., SKS) splitting results (black

bars) from previous studies. Orientation of the bars represent the fast direction and bar length is scaled with the delay time according to the legend shown. A compilation of results from previously published studies is shown (Vinnik et al., 1992; Klosko et al., 1999; Brisbane et al., 1999; Barruol and Hoffman, 1999; Marson-Pidgeon et al., 1999; Audoine et al., 2004; Heintz and Kennett, 2005; Király et al., 2012; Zietlow et al., 2014; Bello et al., 2019). Abbreviations of corresponding geological features are the same as Figure 2.5.

A compilation of results from previous receiver-side and source-side splitting studies for the region is presented in Figure 2.6 and Figure 2.7. From the two figures, we can find that the previous studies are mostly focused on a small number of limited locations along the Australian-Pacific plate boundary. The most extensively studied region using receiver-based techniques is in New Zealand with the earliest studies beginning in the 1990s, using local shear waves (Brisbourne et al., 1999; Audoine et al., 2004) and teleseismic phases like SKS, SKKS and ScS (Vinnik et al., 1992; Klosko et al., 1999; Brisbane et al., 1999; Marson-Pidgeon et al., 1999; Audoine et al., 2004). In the Central Volcanic Region, located to the north of the North Island of New Zealand, the fast direction is nearly trench-parallel, suggesting shear in the mantle or trench-parallel flow associated with continental back arc spreading (Audoine et al., 2004).



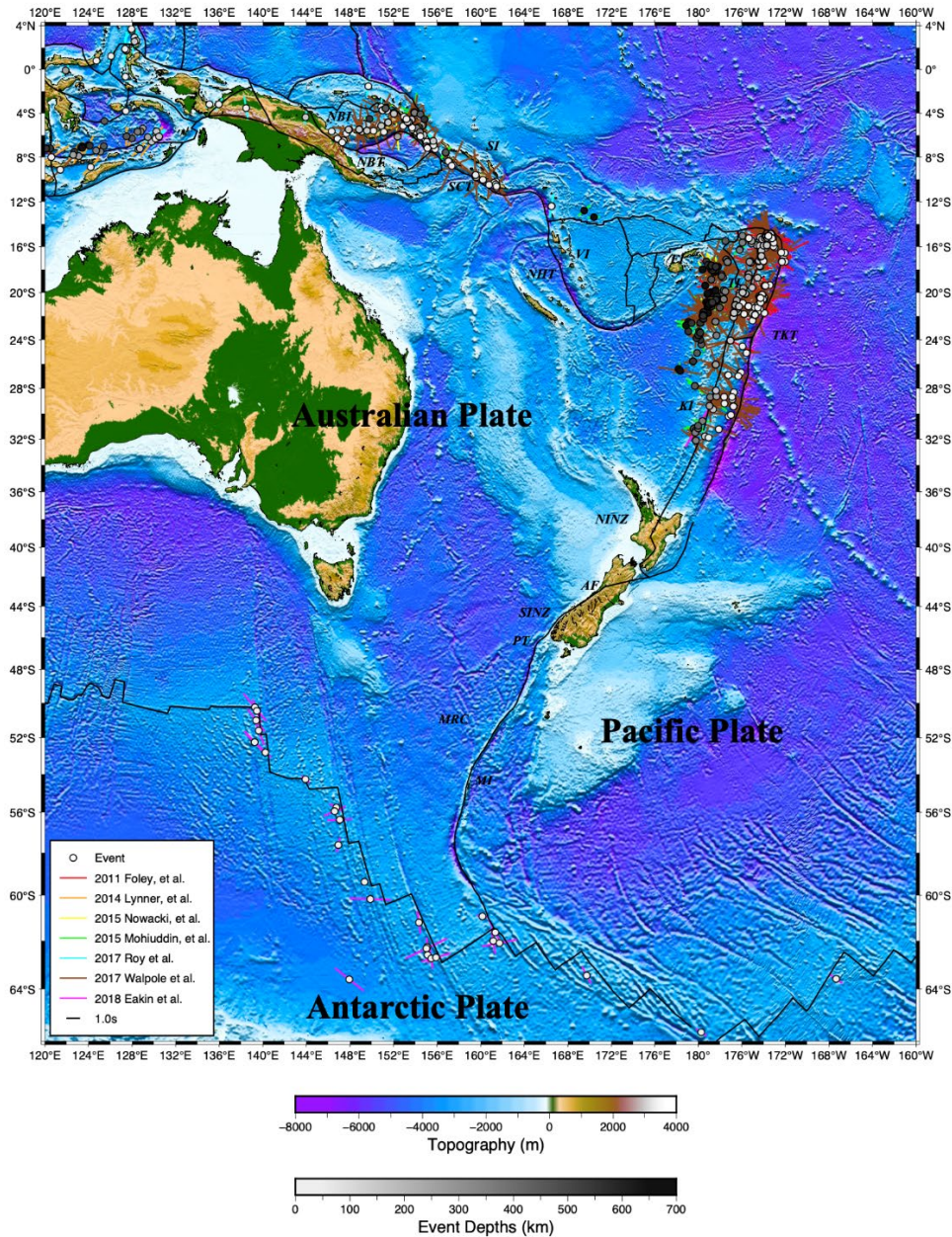


Figure 2.7 Map of source-side splitting results plotted as bars of varying colour corresponding to the individual study (refer to legend). Orientation of the bars represent the fast direction and the length is scaled by the delay time. Abbreviations of corresponding geological features in the figure are the same as Figure 2.5.

Other studies from New Zealand (Klosko et al., 1999; Brisbane et al., 1999; Marson-Pidgeon et al., 1999) mainly focused on the central-southern part of the North Island and the whole South Island, found consistent fast polarization

directions approximately parallel to the strike of the plate boundary. More recent shear wave splitting measurements from Zietlow et al., (2014) made onshore and offshore of the South Island of New Zealand, using both seismic station on land and ocean bottom seismometers, found an approximately 100-200 km wide anisotropic zone of 1.0-2.0 s delay times with fast directions nearly parallel to the direction of relative motion between the Australian and Pacific plates.

Along the entire Macquarie Ridge Complex there is only one broadband seismic station available, station MCQ, located on Macquarie Island (Figure 2.6). A temporary nearby station (MACQ) was analyzed for shear-wave splitting almost 25 years ago by Klosko et al., (1999). They found a delay time is 1.3 seconds and a fast direction trending NW-SE, at a large angle from the strike of the plate boundary which differs to that seen for the South Island in New Zealand.

Other locations along the Australian-Pacific plate boundary with receiver-side shear-wave splitting results include Fiji and the New Hebrides subduction zone (Figure 2.6). For the New Hebrides subduction zone, Király et al., (2012) made a comprehensive SKS shear-wave splitting investigation, grouping the stations into “western” and “eastern” according to the retrieved splitting parameters. For the “western” stations, the fast direction could be best explained by absolute plate motion of the Australian plate. For the “eastern” stations, the nearly trench-parallel orientation of the fast polarization axes and the higher delay times were attributed to the closer location with the subduction zone. In the region of the Fiji Islands, splitting measurements indicate a NW orientation of the anisotropic axis, almost parallel to the absolute motion of the Pacific plate, suggesting a subduction-induced back-arc mantle flow field (Király et al., 2012).

Given the abundance of seismicity along the Australian-Pacific plate boundary, this region has been favorable for applying source-side splitting analysis (Figure

2.7). Several previous studies have employed this methodology to investigate seismic anisotropy beneath the seismically-active Tonga-Kermadec subduction zone, given the abundance of earthquakes at varying depths and suitable epicentral distances from land seismic stations on the western coast of North America (Foley and Long, 2011; Nowacki et al., 2015; Mohiuddin et al., 2015; Walpole et al., 2017). However, these studies do not always show a consistent trend for the fast polarization and delay time as they target anisotropy at different depths. Foley and Long (2011) was the first to perform source-side splitting analysis in this region, discovering trench-parallel or sub-parallel anisotropic fast directions for events of upper mantle and transition zone depth. Additionally, a pattern of delay time decreasing with depth indicated that source of anisotropy for the upper mantle events was likely in the sub-slab mantle, which they attributed to trench parallel flow due to slab rollback. Shear-wave splitting was also recorded from deep earthquakes that suggested the presence of anisotropy in the lower transition zone or uppermost lower mantle (as least in the vicinity of the subducting slab).

Subsequent studies by Mohiuddin et al. (2015) and Nowacki et al. (2015) utilized earthquakes with mid-range source depths (~ 300-650 km and 200-650 km, respectively). Mohiuddin et al. (2015) found the fast polarization directions were generally parallel to the subducting slab contours. In the study of Nowacki et al. (2015), the splitting fast direction was approximately parallel to the subduction direction, in contrast to the pattern of Foley and Long (2011). However, it's worth noting that the depth of the earthquakes used between the two studies. Walpole et al. (2017) applied a global analysis of source-side splitting to probe the anisotropy of subduction zones. For the Tonga-Kermadec region, their results show trench-parallel splitting measurements, particularly for shallow events (source depth < 50 km), while for deeper events, the fast direction is more variable.



For the regions of New Britain and the Solomon Islands, there are some clear differences among the fast splitting directions from different studies. Roy et al. (2017) reported trench-normal fast directions based on measurements from shallow events, while Walpole et al. (2017) observed a more scattered pattern, with fast directions generally sub-parallel to the trench. In two other studies (Mohiuddin et al., 2015; Nowacki et al., 2015) focusing on deep-source earthquakes (~ 300-650 km and 200-650 km, respectively), trench-parallel fast directions were observed in the former, while the latter exhibited nearly trench-normal fast directions. However, the number of splitting measurements was limited for both studies.

The New Hebrides subduction zone has less deep seismicity than the Tonga-Kermadec subduction zone. Only a handful of source-side splitting results are available but these show a trench perpendicular fast direction (Mohiuddin et al., 2015). However, in the global splitting study of Walpole et al. (2017), the results are quite different, with parallel or sub-parallel fast directions for shallow earthquakes (<100 km) and dispersed fast directions for deep events (100-300 km).

In summary, previous shear-wave splitting studies conducted at various (but limited) locations along the Australian-Pacific plate boundary provide insights on the dynamics of the plate boundary and Earth's interiors below. However, such investigations along the plate boundary are not complete and many gaps in shear-wave splitting measurements exist. One such prominent gap is the MRC, where there are plentiful earthquakes occurring with mostly strike-slip focal mechanisms and shallow source depths. This abundance of seismic events provides a substantial dataset that can potentially be utilized for source-side splitting analysis. Additionally, the only previous shear-wave splitting

results for the region come from the single permanent seismic station deployed on Macquarie Island that was analyzed for receiver-side splitting in 1999 (Klosko et al., 1999). Given that more than 20 years have passed since then, there is a wealth of new seismic data available that can be utilized for a fresh receiver-side splitting study. Consequently, this presents an opportunity to apply both receiver-side and source-side splitting methods for a comprehensive analysis of the MRC region.

# Chapter 3

## Methodology and Data

### 3.1 Methodology

#### 3.1.1 The shear-wave splitting concept

Shear wave splitting is perhaps the most popular method for characterizing and inferring anisotropic structure within the Earth interior. As Figure 3.1 illustrates, when a shear wave propagates through an anisotropic medium, it is split into two separated orthogonally-polarized components, one parallel to the fast direction of the anisotropic medium, and the other to the slow direction. In this process, a delay time will be accumulated between the two components due to the different velocity of the seismic waves. We usually use two parameters: (i) the fast polarization direction of the shear wave,  $\phi$ , and (ii) the delay time,  $\delta t$ , to constrain and infer the geometry and the strength of the anisotropy and/or path-length through the anisotropic medium underneath.

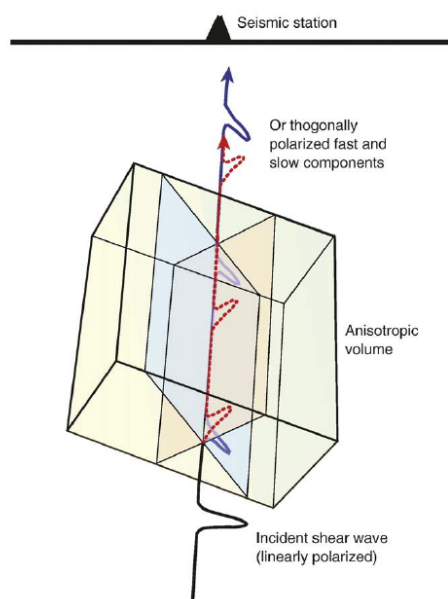


Figure 3.1 Propagation of a shear wave through an anisotropic medium demonstrating the phenomenon of shear-wave splitting. Figure is taken from Long and Becker, (2010).

Additionally, if the initial polarization of the incoming shear wave is aligned with either the fast or slow direction of the anisotropic medium, or if the medium is isotropic, then no shear-wave splitting will occur. Such observations are deemed a “null” measurement.

### **3.1.2 Receiver-side versus source-side applications**

With For targeting upper mantle anisotropy with shear-wave splitting, there are two main applications: receiver-side splitting and source-side splitting analysis. The terms “receiver-side” and “source-side” indicate whether the targeted region is the upper mantle beneath the seismic receiver or beneath the earthquake source. As illustrated in Figure 3.2a, receiver-side splitting analysis utilizes core-refracted seismic phases such as SKS, SKKS and PKS which span a range of epicentral distances (SKS: [90°, 130°]; SKKS: [90°, 180°]; PKS: [130°, 150°]). These core-refracted phases can be used to probe the seismic anisotropy beneath the seismic station (i.e., receiver-side).

Source-side splitting analysis is applied to constrain the seismic anisotropy beneath the earthquake source (i.e., source-side) using distant seismic stations. Additional steps and constraints are needed in order to be apply source-side splitting. Firstly, it must be possible to either correct for or neglect anisotropy beneath the seismic station. This is most easily achieved by only utilizing seismic stations that return an overwhelming majority of null measurements, across a substantial swath of back-azimuth, when analysed by receiver-side splitting (Figure 3.2b). This ensures apparent isotropy on the receiver side for near-vertical propagating shear-waves. In such cases, assuming the lower

mantle is also isotropic, then the primary region of anisotropy that a direct-S ray-path will encounter is in the upper mantle beneath the source. The second criteria is that epicentral distance must be in the range  $40^{\circ}$ - $80^{\circ}$ . This ensure the direct-S ray-path avoids the potentially anisotropic lowermost mantle (i.e., the D'' layer), and that the incidence angle is sufficiently steep.

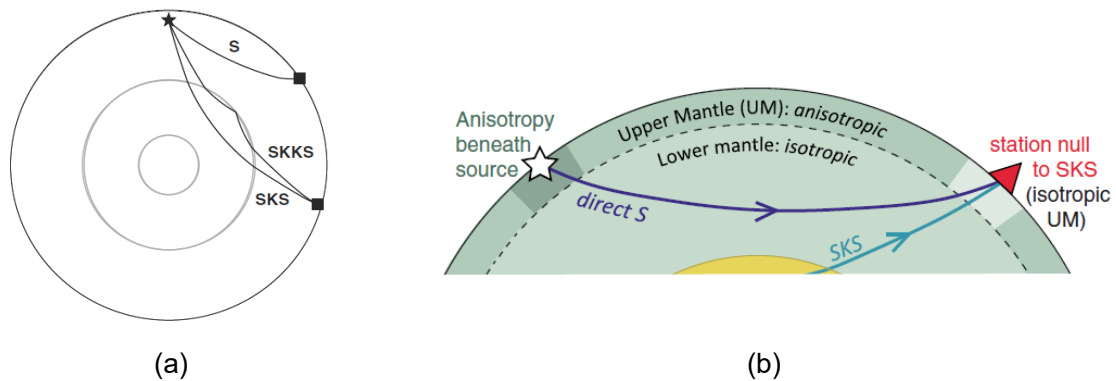


Figure 3.2 Seismic phases and ray-path geometries for (a) receiver-side studies (taken from Long and Silver, 2009) and (b) source-side studies (taken from Eakin et al., 2018).

For receiver-side splitting analysis, the initial polarization of the shear-wave is known as it is controlled by the P-to-S conversion at the core-mantle boundary (CMB), resulting in polarization to the radial plane (i.e., equivalent to the back-azimuth). This is beneficial for measuring the shear-wave splitting as any energy on the transverse component can be attributed to the presence of seismic anisotropy. In addition, the anisotropic structure can be inferred from a single record, the result is free from the influence of lateral heterogeneity and could feature excellent lateral resolution. However, the interpretation of shear-wave splitting from the receiver-side method in terms of upper mantle anisotropy is dependent on the assumption of isotropy for other layers. Since shear-wave splitting measurements are path-integrated measurements, the seismic phases may be affected by anisotropy anywhere along the ray path. It is therefore possible for potential contamination from anisotropy present within the crust, the lower mantle and the D'' region. However, the contribution from

these regions is expected to be small, compared to that from the asthenospheric upper mantle (e.g., Long and Becker, 2010).

For source-side splitting analysis, using station-event pairs with epicentral distances  $<80^\circ$  avoids the influence of anisotropy from the D'' layer. Other benefits of the source-side application include the ability to study seismic anisotropy in locations where there are no or few seismic stations deployed, such as intra-oceanic plate boundaries. However, drawbacks of this method include the reliance on careful characterization of anisotropy (or apparent isotropy) beneath the receiver prior to conducting source-side splitting (e.g., Eakin et al., 2018). If the influence of anisotropy beneath the receiver cannot be ruled out, then seismic anisotropy beneath the source will not be well constrained.

### **3.1.3 Measurement methods: Rotation correlation and transverse component minimization**

There exists a variety of measurement methods for the calculation of the splitting parameters, namely the fast splitting direction,  $\varphi$ , and the delay time,  $\delta t$  (Bowman and Ando, 1987; Vinnik et al., 1989; Silver and Chan, 1991; Chevrot, 2000; Menke and Levin, 2003). Here we focus on two methods, the rotation correlation (RC) method (Bowman and Ando, 1987) and the transverse component minimization (SC) method (Silver and Chan, 1991), which are most commonly used in the shear-wave splitting studies.

When a shear wave passes through an anisotropic medium, the fast and slow components generated through shear-wave splitting are expected to have identical pulse shapes. The RC method utilizes this principle to search for the values of  $(\varphi, \delta t)$  that produces the maximum cross-correlation between the

corrected fast and slow components. In this way, the RC method is independent of the initial polarization of the shear wave. In comparison, the SC method finds the values of  $(\varphi, \delta t)$  that best minimize the energy on the corrected transverse component (or rather the component perpendicular to the initial polarization), and thus linearizes the corrected particle motion of the shear wave. Unlike the RC method, the SC method requires prior knowledge of the initial polarization. For both RC and SC methods, a null measurement is identified if the uncorrected particle motion is already linear.

The RC method is known to produce systematic error as a function of initial polarization, equivalent to the back-azimuth for \*KS phases (Eakin et al., 2019; Wüstefeld and Bokelmann, 2007). When the initial polarization approaches the fast or slow orientation of the anisotropic medium, the RC method will predict a best fitting value of  $\varphi$  that deviates  $45^\circ$  from the true value, with a delay time that is close to zero. This results in  $90^\circ$  periodicity of the shear-wave splitting parameters as a function of initial polarization and a distinctive saw-tooth pattern in  $\varphi$  with a  $45^\circ$  slope (see figure 7 of Eakin et al., 2019). This phenomenon was utilized in Wüstefeld and Bokelmann, (2007) to develop a novel criterion for identifying null measurements in shear-wave splitting studies. The same pattern is also seen for the SC method when the signal-to-noise ratio is moderately high (SNR~5). Such systematic error can however be beneficial as it is easily predictable and can be expressed mathematically according to the following equations from Eakin et al., (2019):

$$\Phi_{app} = \Phi_{true} - \frac{90}{\pi} \tan^{-1} \cot\left(\frac{\pi}{90}(\varphi - \Phi_{true})\right) \quad (3.1)$$

$$\delta t_{app} = \delta t_{true} * \left| \sin\left(\frac{\pi}{90}(\varphi - \Phi_{true})\right) \right| \quad (3.2)$$

Where  $\Phi_{app}$  and  $\delta t_{app}$  refer to the expected or apparent fast direction and delay

time, respectively, due to the systematic error as a function of the back azimuth ( $\varphi$ ). The true parameters of the anisotropic medium are represented by  $\Phi_{\text{true}}$  and  $\delta t_{\text{true}}$ . In both equations, the units for  $\varphi$  are in degrees, and for  $\delta t$  in seconds.

### **3.2 Processing steps in SplitLab**

In this study, we used the SplitLab software package (Wüstefeld, et al., 2008) to perform shear-wave splitting analysis for both receiver-side and source-side measurements. SplitLab is an integrated package built and operated in the Matlab environment, that includes functions to input the seismic data, calculate the splitting parameters, and provide textual and graphical visualizations.

In order to conduct shear-wave splitting with teleseismic phases, events with relatively large magnitudes (usually  $M_w > 5.0$ ) are required to ensure enough energy and amplitude of the selected phase. Additionally, events are required to be in an appropriate epicentral distance range depending on different seismic phases, i.e.,  $90^\circ$ - $130^\circ$  for SKS,  $130^\circ$ - $150^\circ$  for PKS, and  $40^\circ$ - $80^\circ$  for direct-S. This ensures steeply incident seismic waves and to avoid overlap with the arrival of other seismic phases. A bandpass filter of 8 - 25 s is applied to all the seismic waveforms to reduce the impact from high-frequency noise and improve the signal-to-noise-ratio (SNR).



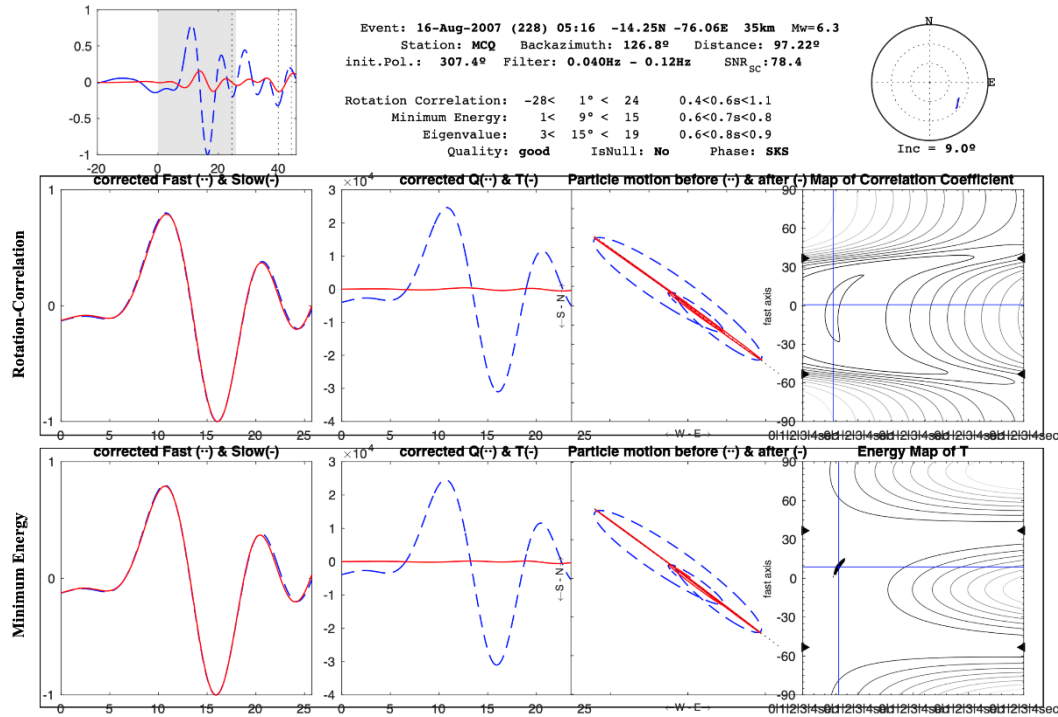


Figure 3.3 Example of a “good quality” SKS splitting measurement made at station MCQ located in the Macquarie Ridge Complex. At the top left, the uncorrected radial (dashed blue line) and transverse (solid red line) components are shown; the analysis window is shown in gray. The event information and calculated results from three methods (the RC method, the SC method and the eigenvalue minimization method) are provided at the top center, including the event date, location, depth, magnitude, recording station, back-azimuth, epicentral distance, initial polarization, filter applied, the Signal-to-Noise Ratio (SNR), best-fitting  $\phi$ ,  $\delta t$  values and their error ranges. The middle panel presents splitting diagnostics for the RC method; the bottom panel presents splitting diagnostics for the SC method. The optimal splitting parameters are  $\phi=1^\circ$ ,  $\delta t=0.6$  s (the RC method) and  $\phi=9^\circ$ ,  $\delta t=0.7$  s (the SC method), and  $\phi=15^\circ$ ,  $\delta t=0.8$  s (the eigenvalue minimization method). These splitting parameters agree well within formal errors.

After filtering, all seismograms are visually inspected to manually select the time window that best captures the shear-wave pulse of interest. Using the waveforms within this time window, SplitLab then calculates the best-fitting splitting parameters via two independent measurement methods: the

transverse component minimum energy (SC) method of Silver and Chan (1991), and the rotation correlation (RC) method (Bowman and Ando, 1987). The SC method utilizes a grid search approach to identify the pair of splitting parameters, fast direction  $\phi$  and delay time  $\delta t$ , to best minimize the energy on the transverse component that serves as a correction for the splitting. The same grid search principle is applied for the RC method with the best-fit splitting parameters determined by rotating and time-shifting the horizontal components and performing a cross-correlation.

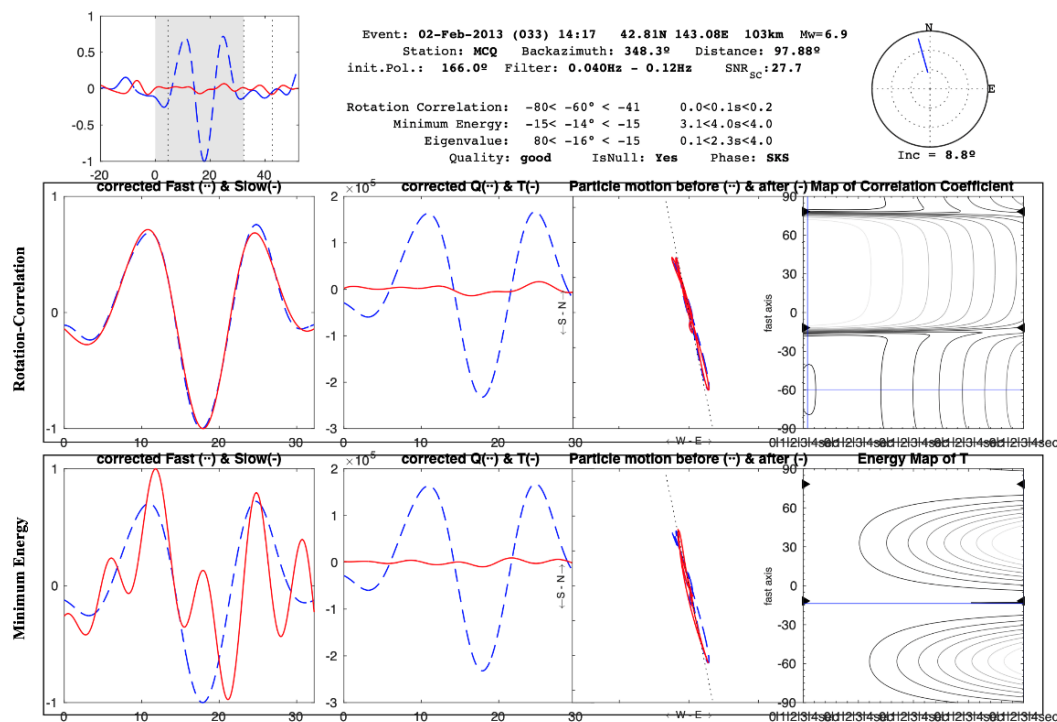


Figure 3.4 Example of a “good quality” SKS null measurement made at the station MCQ in the Macquarie Ridge Complex. The legend is the same as Figure 3.3, however, the calculated results of splitting parameters from the three methods are no longer in agreement in the case of a null measurement.

After the calculation, the diagnostic diagram (Figure 3.3 and Figure 3.4) is manually reviewed. Based on these diagnostic outputs it is decided by the user whether the event is of sufficient quality to keep, and if it is a split or null. If the

SNR is poor, and shear-wave pulse is difficult to identify due to noise then the event will be discarded. For split and null measurements, a quality assessment is made to place the result into one of three categories: “good quality”, “fair quality”, or “poor quality”, based on the criteria outlined in the following paragraphs.

As Figure 3.3 presents, a “good quality” split measurement should satisfy:

- (i) A relatively large energy pulse around the predicted arrival time of the phase on both horizontal components, and relatively low noise before and after (top left corner inset plot of Figure 3.3).
- (ii) Signal-to-Noise ratio (SNR)  $> 5$ .
- (iii) A similar shape of the corrected fast and slow components (first column inset of Figure 3.3).
- (iv) Minimal energy on the corrected transverse component (second column inset of Figure 3.3).
- (v) Elliptical uncorrected particle motion and linear corrected particle motion with the orientation aligning with the back-azimuth for SKS/PKS or long axis of the ellipse for direct-S (third column inset of Figure 3.3).
- (vi) Small and generally circular error solutions (fourth column inset of Figure 3.3).
- (vii) Good agreement of the fast direction and delay time between the RC and SC methods, usually within  $\pm 10^\circ$  for  $\varphi$  and  $\pm 0.5$  s for  $\delta t$  to be considered good quality (upper middle labels of Figure 3.3).

Measurements of “fair quality” have less strict conditions for SNR and particle motion correction, but still need to have a relatively small errors (i.e.,  $\pm 10^\circ$ - $15^\circ$  for  $\varphi$  and  $\pm 0.5$ - $0.8$  s for  $\delta t$ ). Generally, only the events rated as “good quality” and “fair quality” can be utilized in further analysis, and any measurements of “poor quality”, which have low SNR, or errors in  $\varphi$  larger than  $25^\circ$  and in  $\delta t$

larger than 1.0 s are less likely to be considered.

Figure 3.4 illustrates a “good quality” null measurement. The conditions for a “good quality” null measurement are similar to that for a “good quality” splitting measurement:

- (i) A relatively large energy pulse around the predicted arrival time of the phase on the radial component but not on the transverse, and relatively low noise before and after (top left corner inset plot of Figure 3.4).
- (ii)  $SNR > 5$ .
- (iii) Linear uncorrected particle motion (third column inset of Figure 3.4).

Null measurements of a “fair quality” may have a higher tolerance for noise on the transverse component, but the clearly-identified linear trend of the uncorrected particle motion should be guaranteed. If the noise level is too high that the shear-wave cannot be confidently identified, or no apparent linear trend of uncorrected particle motion observed, the measurement will be labelled as “poor quality” and will not be used.

For source-side measurements there is an additional consideration regarding the geometry of raypath and the difference between the up-going versus down-going ray reference frame. After acquiring the best-fitting splitting parameters from SplitLab, a further adjustment is made following the equation from Agrawal et al., (2020), to convert the fast direction to that representative beneath the source:

$$\sigma_S = 2\alpha - \sigma_F - 360 \quad (3.3)$$

In the above equation, “ $\sigma_S$ ”, “ $\alpha$ ”, and “ $\sigma_F$ ” represent the fast direction on the

source-side, the ray azimuth, and the fast direction on the receiver-side respectively. The units for all of the values are in degrees.

## **Chapter 4**

# **Shear-wave splitting results along the Macquarie Ridge Complex**

## **4.1 Receiver-side splitting analysis of the Macquarie Ridge Complex**

The simplest and most common shear-wave splitting application is the receiver-side technique that uses core-refracted phases such as SKS. This technique targets the anisotropic structure directly beneath the receiver, and therefore requires seismic stations located within the region of interest. As previously mentioned, at the time of this study, there was only one broadband station located in all of the MRC. This is permanent station MCQ (Latitude:  $-54.4983^\circ$ , Longitude:  $158.9402^\circ$ , Figure 4.1) from the Australian National Seismograph Network (network code: AU, DOI: 10.26186/144675) located on Macquarie Island, in the central MRC. This station has a long recording period of seismic data from 2004 onwards that has never been previously analyzed for shear-wave splitting. An earlier temporary station (XU: MACQ) in a nearby location operated from 1996-1997 and was previously analyzed for receiver-side splitting (Klosko et al., 1999) with only one year of data. Given the longer recording period of station MCQ, and its location at the center of the study area (Figure 4.1), a new investigation of receiver-side splitting at this location is therefore warranted.

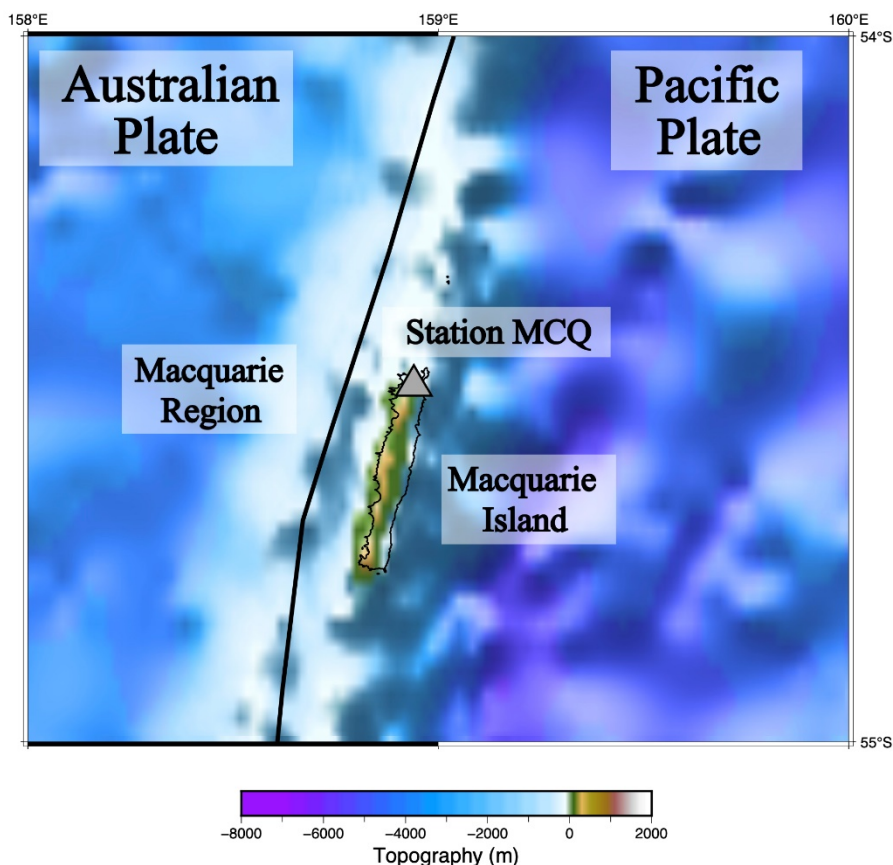
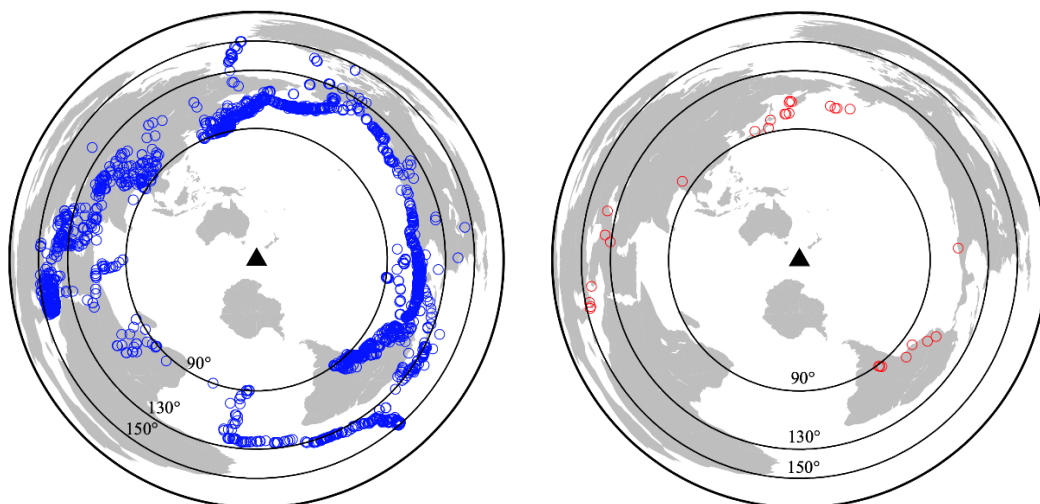


Figure 4.1 Location of station MCQ within the MRC study area. The background color corresponds to the bathymetry/topography of the study area. The thick black lines indicate the plate boundary of the MRC. The grey triangle shows the location of station MCQ at the northern end of Macquarie Island.

For this study, following the methodology as outlined in section 3.1, SKS and PKS phases were picked and utilized. Events of magnitude greater than 5.5 in the appropriate epicentral distance range were selected during a 16-year time period from 28 June, 2004 to 2 April, 2020. In total 1782 events for SKS were available, and 577 for PKS, over a wide back-azimuthal distribution (Figure 4.2a, and 4.4). Based on the criteria introduced in section 3.2, only split and null measurements of “good quality” or “fair quality” were kept for further analysis. Unfortunately, station MCQ is very noisy due to its proximity to the Southern Ocean, and only a small number of events returned results of sufficient quality (Figure 4.2b). These included 8 split and 14 null measurements for SKS phases,

and 5 split and 2 null measurements for PKS phases. The back-azimuthal distribution of these events is more limited (e.g., Figure 4.4).

Various compilations of the results for station MCQ are provided in Figures 4.3-4.8. Overall, the results suggest the anisotropic fast-axis is orientated NNW-SSE, which is somewhat oblique to the NNE-SSW orientation of the plate boundary in this location (Figure 4.1), but slightly less oblique than the earlier result from Klosko et al., (1999) as plotted in Figure 2.6. The station averaged values are  $\varphi_{RC}$ :  $-20.2^\circ$ ,  $\delta t_{RC}$ : 1.07 s, and  $\varphi_{SC}$ :  $-13.5^\circ$ ,  $\delta t_{SC}$ : 1.18 s, indicating similarity between the two methods. The pattern of results from SKS versus PKS phases also appear to be consistent (Figure 4.5-4.8). In total, more null results (16 total) are returned than splits (13 total), which may be due to the relatively large number of available events with back-azimuths that align with the average fast direction (lower plot Figure 4.4). Correspondingly, the distribution of back-azimuths at which null measurements are recorded agrees well with the fast direction retrieved from the split measurements (Figure 4.3). This suggests that both the splits and the nulls are indicative of the same anisotropic structure, and that the nulls are consistent with alignment of the initial polarization of the shear wave with the fast-axis.





(a)

(b)

Figure 4.2 (a) Map of all the events (blue circles) utilized in the study and (b) Map of all the measurements (red circles) utilized in the study. The triangle represents the location of the station MCQ and the three large circles in black illustrate the ranges of epicentral distance of  $90^\circ$ ,  $130^\circ$  and  $150^\circ$ , respectively.

While the size of the dataset is relatively small, moderate back-azimuthal variability of the splitting parameters is still found (Figures 4.5-4.8). However, the back-azimuthal variations clearly follow the predicted pattern of systematic error, as outlined in Eakin et al., (2019) and section 3.1.3. The same saw-tooth pattern in  $\varphi$  is seen for both the RC method (Figure 4.5) and the SC method (Figure 4.7), and is consistent with a NNW-SSE fast-axis (equivalent to a jump in the gold line at a back-azimuth of  $\sim 75^\circ$ , when modulated over the range  $0^\circ$ - $90^\circ$ ). In summary, the back-azimuth variations of the results follow the predicted systematic error, and therefore are consistent with a single-layer of anisotropy.

**Distribution of fast splitting directions of (SKS+PKS) good- and fair-quality split measurements and back azimuths of (SKS+PKS) good- and fair-quality null measurements for station MCQ**

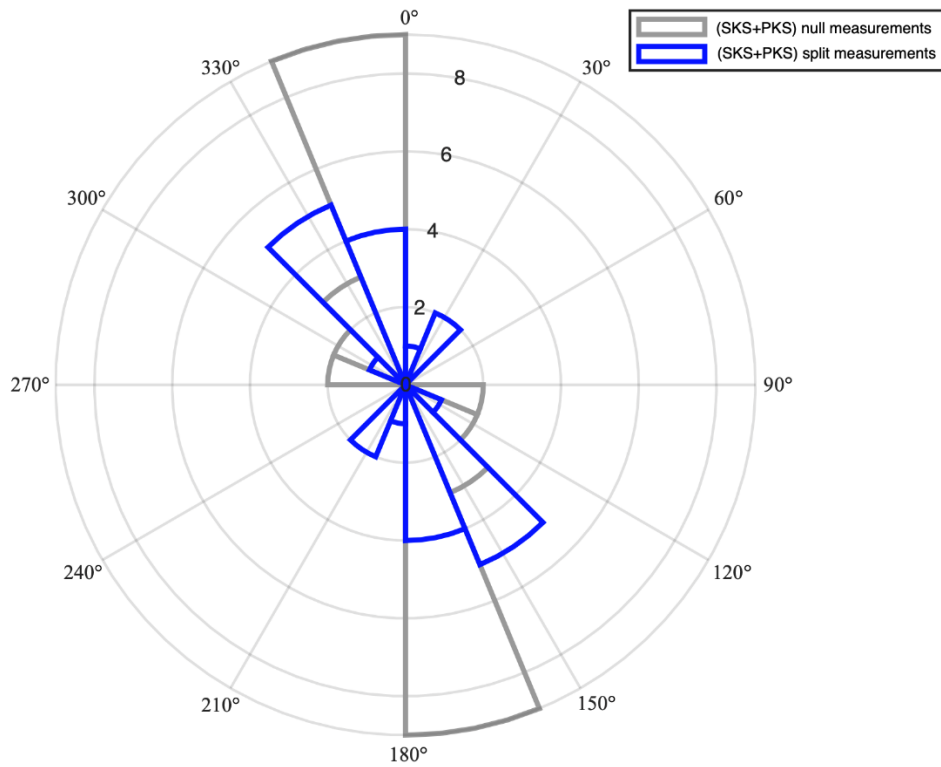


Figure 4.3 Rose diagram showing the distribution of fast splitting directions from both SKS- and PKS-phases for good- and fair-quality split measurements (blue), and the back-azimuth for good- and fair-quality null measurements (grey) at station MCQ. The number around the edge of the circle indicate the angle clockwise from North, and the number of measurements in each bin increases with distance from the center of the circle.

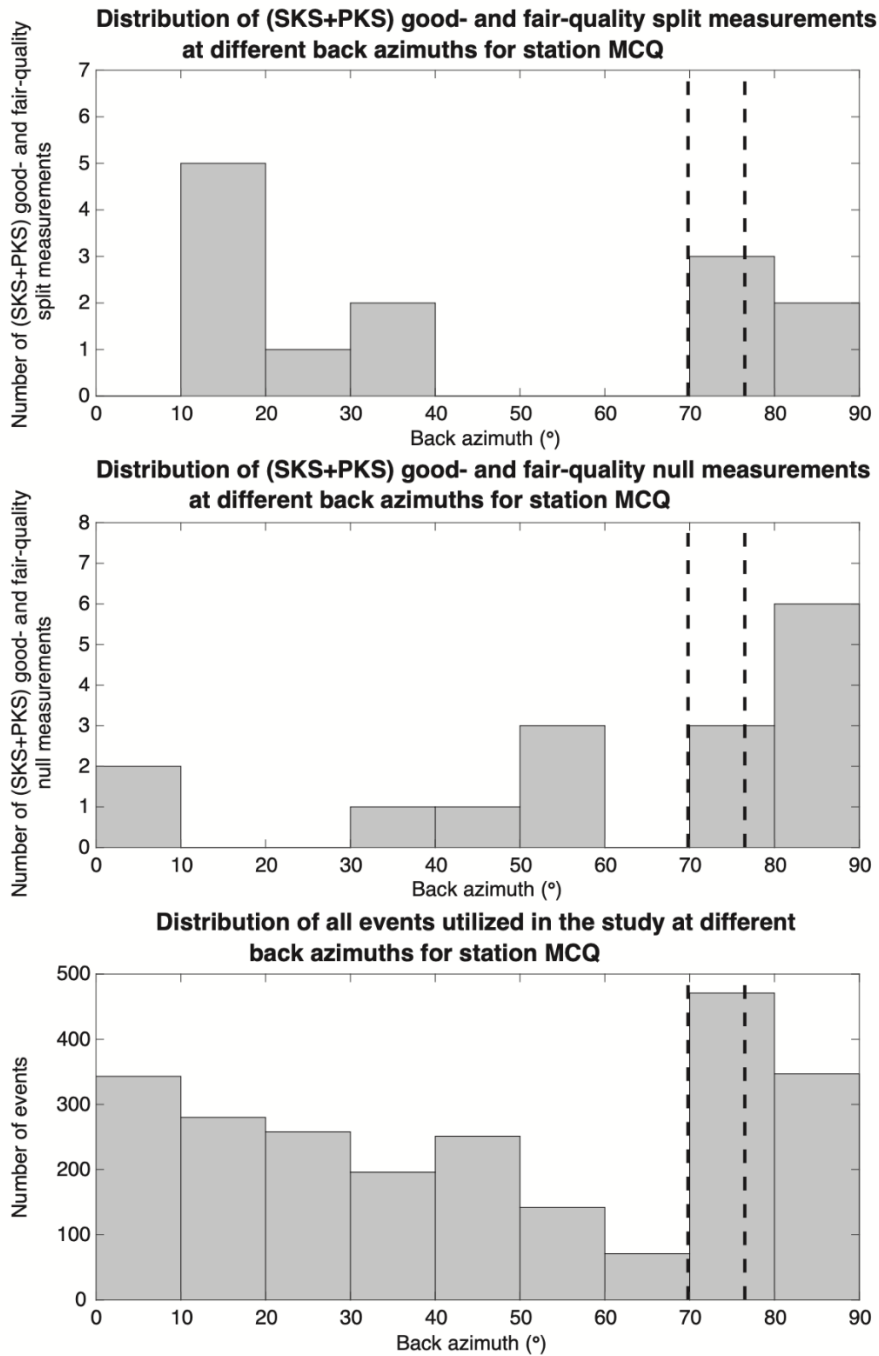


Figure 4.4 Histograms illustrating the number of split measurements (upper plot) and null measurements (middle plot) compared to the event back-azimuth availability (lower plot), modulated over the back-azimuthal range of 0°-90°. The two dotted black lines correspond to the average fast direction for the station from the RC method (-20.2°) and the SC method (-13.5°).

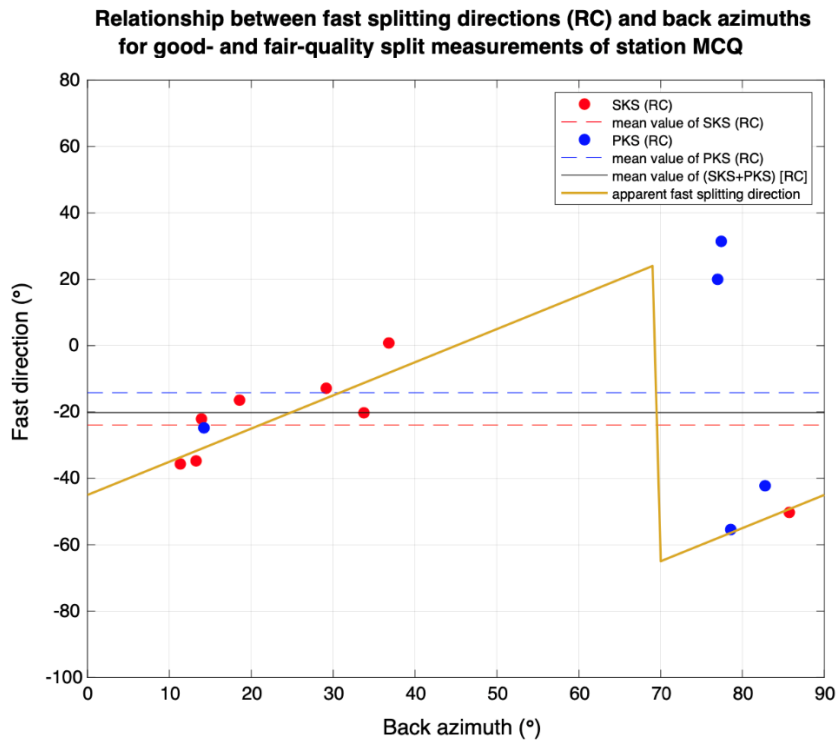


Figure 4.5 Relationship between apparent fast direction and the event back-azimuth for good- and fair-quality split measurements from the RC method at station MCQ. The red circles represent SKS phases, and the blue circles PKS phases. The dotted red line indicates the SKS average value, the dotted blue line the PKS average value, and the thin black line the average for SKS and PKS combined which has a value of  $-20.2^\circ$ . The gold line illustrates the predicted systematic error in fast direction as a function of back azimuth, according to the empirical equation of Eakin et al., (2019), as outlined in section 3.1.3 (i.e., equation 3.1).

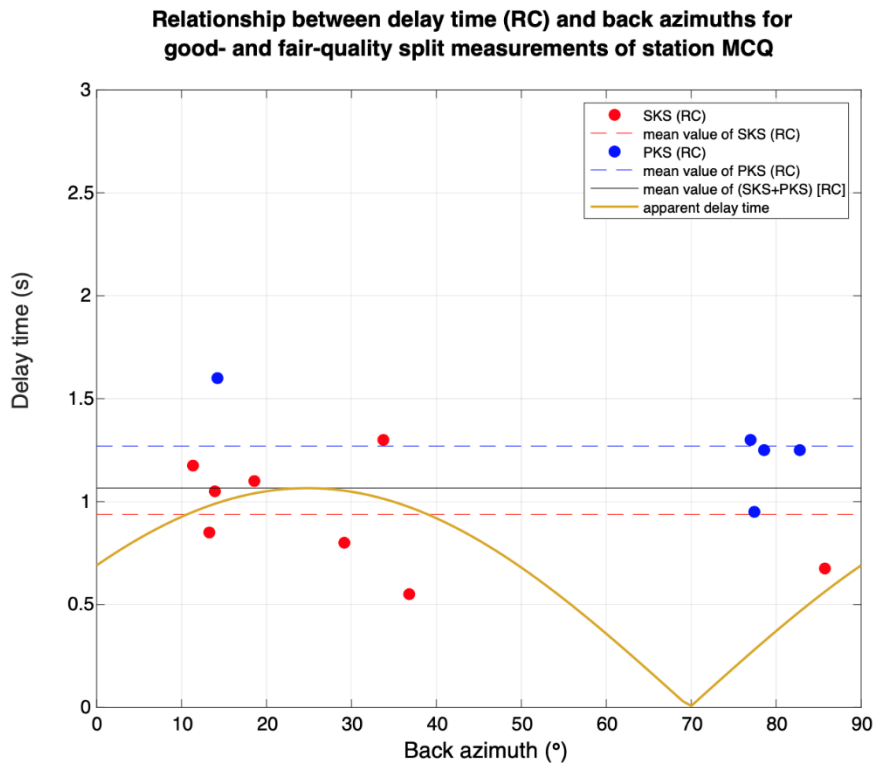


Figure 4.6 Same as Figure 4.5, except illustrating the apparent delay time as a function of event back-azimuth. The average delay time of all SKS- and PKS split measurements from the RC method is 1.07 seconds. The gold line corresponds to the predicted systematic error in delay time according to equation 3.2 as outlined in section 3.1.3.

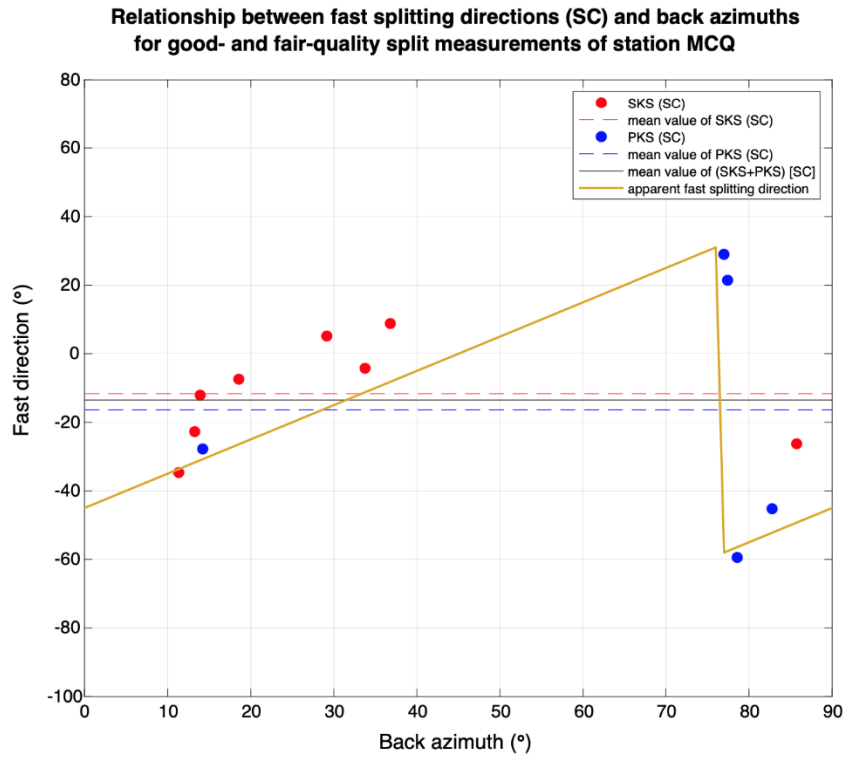


Figure 4.7 Same as Figure 4.5, except from the SC method. The average fast direction from all SKS and PKS split measurements from the SC method is  $-13.5^\circ$ .

**Relationship between delay time (SC) and back azimuths for good- and fair-quality split measurements of station MCQ**

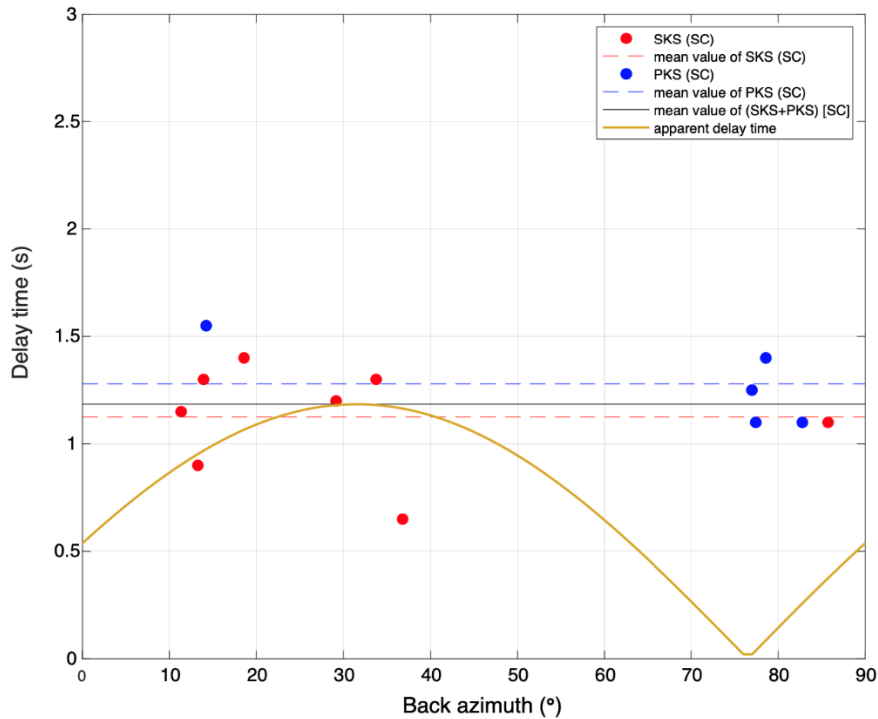


Figure 4.8 Same as Figure 4.6, except from the SC method. The average delay time of all SKS and PKS split measurements from the SC method is 1.18 seconds.

## 4.2 Stations, events, and modifications for source-side splitting analysis of the Macquarie Ridge Complex

Compared to receiver-side splitting analysis, two prerequisites are required to be taken into consideration in advance for source-side splitting analysis. (1) The receiver-side splitting analysis has been applied to the stations in advance, showing a majority of null measurements across a substantial swath of back-azimuths (i.e., “null stations”), from which we can infer apparent isotropy on the receiver-side. (2) The chosen stations are within an epicentral distance of 40°-80° from the events.

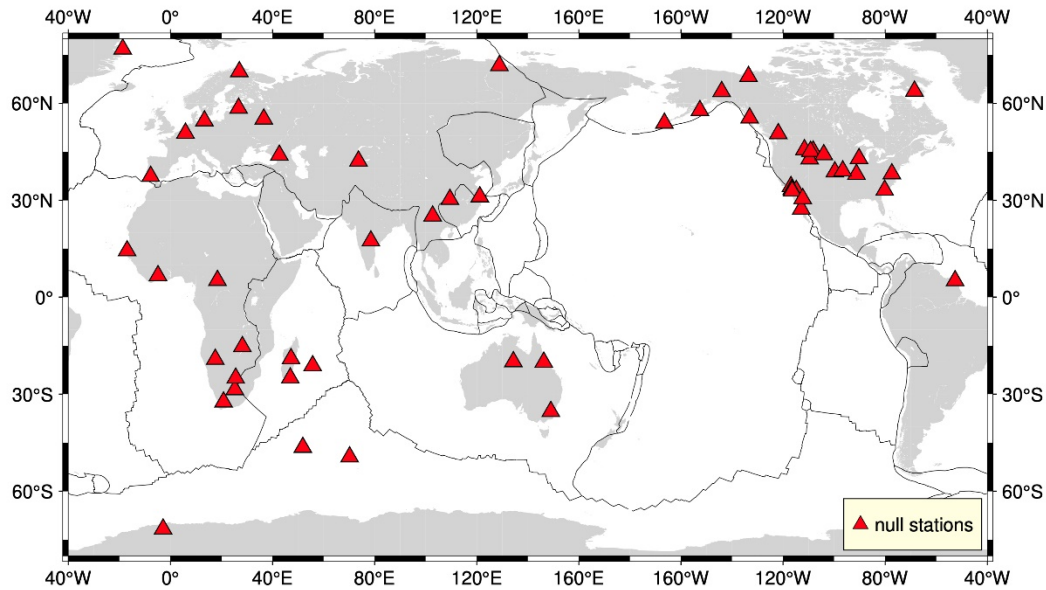


Figure 4.9 Map of the “null stations” globally (modified from Eakin et al., 2018).

Based on the “null stations” list we got from previous research work (Eakin et al., 2018; Figure 4.9), we can find that the stations which meet the prerequisites (1) are mainly distributed in western Europe, North America and South Africa. However, according to the reference of prerequisites (2), we still need to consider the epicentral distance between the events at the MRC and the known “null stations”. After the calculation of epicentral distances between these stations with several reference points along the plate boundary at the MRC, we selected some stations available, but the number of this kind of stations is very small. So, we also applied the receiver-side splitting analysis to some of the other stations within the required epicentral distance, and selected the stations which meet the requirement that the majority of observations are null measurements at the back azimuth range between the station and the MRC. In this way, we acquired more stations available for our splitting analysis for the MRC. Finally, the datasets of all these stations were input into SplitLab individually, and for the source-side splitting analysis, we made some modifications to the code in Matlab, and the selection criteria and some of the procedures are similar to what has been introduced in section 3.2.



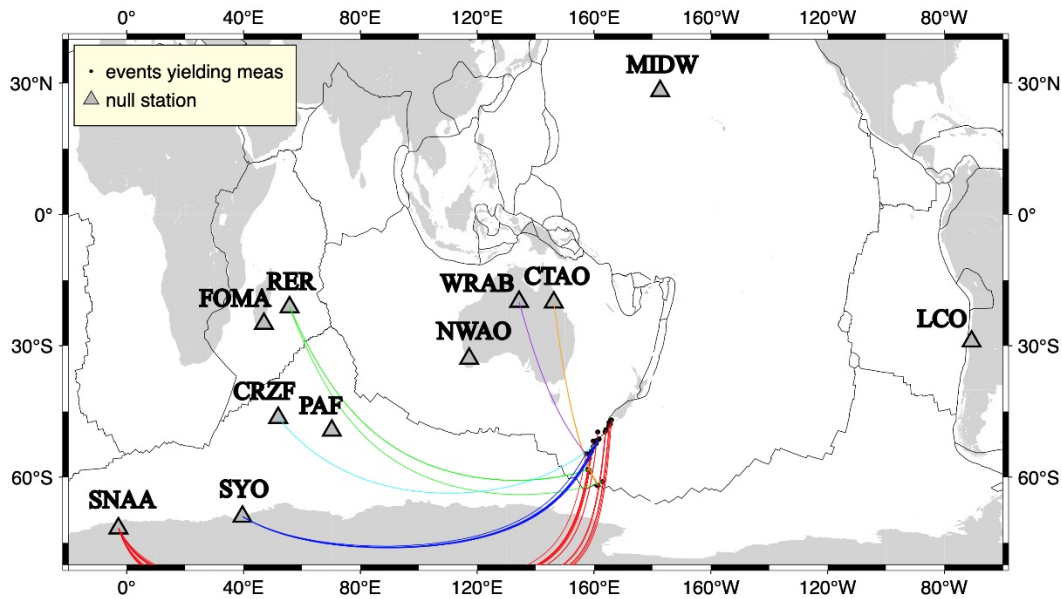


Figure 4.10 Locations of suitable stations utilized in the source-side splitting analysis of the MRC. The triangles represent the stations, with the station names beside them correspondingly. The black dots show the location of events yielding valid measurements at the MRC, connected by ray-paths of various colors corresponding to the seismic station at which the measurement was recorded.

Finally, there were 11 seismic stations in total (SNAA, SYO, MIDW, NWAQ, CIAO, WRAB, FOMA, RER, LCO, CRZF and PAF) that were considered for source-side splitting analysis. However, not all of them returned valid measurements, only those connected to an event by a coloured ray-path in Figure 4.10. Some of stations were situated on the edge of the epicentral distance range and thus had less MRC events which could be analyzed (e.g., MIDW, NWAQ, WRAB). Other stations presented very limited number of valid measurements due to the poor quality of seismic data (e.g., CIAO, WRAB, FOMA, RER, LCO, CRZF and PAF). The majority of source-side measurements were from stations SNAA and SYO, which are situated in Antarctica and were found to be of high quality for this type of study.

Overall, 733 event-station pairs were analyzed for shear-wave splitting of the

direct-S wave. The same methodology was followed as for the receiver-side analysis, as described in previous sections. Prior modifications of the SplitLab code, as outlined in Eakin et al., (2018), allowed for the SC method to still be utilized for direct-S phases. In this case the splitting parameters are estimated by minimizing the energy on the component orthogonal to the initial polarization direction, rather than on the transverse component. The initial polarization is equivalent to the back-azimuth for phases such as SKS, but can be estimated from the long axis of the ellipse in the uncorrected particle motion for direct-S. For source-side splitting, however, the splitting parameters reported are primarily from the RC method (unless otherwise stated) as it is independent of the initial polarization.

Following these source-side splitting procedures, 14 good/fair-quality and 6 poor-quality split measurements were returned, alongside 8 good/fair-quality null measurements, which are further described in section 4.4.

It is worth noting that for the source-side splitting analysis of the MRC, the poor-quality splitting measurements are still included due to the very limited number of measurements. However, the saved “poor quality” splitting measurement still satisfy:

- (i) A recognizable shear-wave pulse around the predicted arrival time of the direct-S wave, albeit with relatively high noise before and after.
- (ii) A similar shape of the corrected fast and slow components, with reduced energy on the horizontal component orthogonal to the initial polarization.
- (iii) Cursory elliptical uncorrected particle motion and linear corrected particle motion with the orientation aligning with the long axis of the ellipse.
- (iv) Error solutions between the two methods that overlap.

- (v) Moderate agreement of the fast direction and delay time between the RC and SC methods (usually within  $\pm 20^\circ$  for  $\varphi$  and  $\pm 1.0$  s for  $\delta t$ ).

### **4.3 Acquiring additional stations suitable for source-side analysis at the MRC**

Due to the limited availability of known “null stations” in the suitable range for source-side splitting analysis at the MRC (i.e., Figure 4.9-4.10), we dedicated substantial time and effort to identify additional seismic stations that could potentially be utilized. Our approach involved considering an alternative strategy. In the first step, we searched for any seismic station within the standard epicentral distance range of  $[40^\circ, 80^\circ]$  from the MRC. In the second step, we investigated whether any prior receiver-side studies had been conducted for these stations as reported in the shear-wave splitting database (<https://ds.iris.edu/spud/swsmeasurement>). If such studies existed, we compared the reported fast direction (and the inferred slow direction) to the back-azimuth between the station and some reference points along the MRC plate boundary. If the back-azimuth was consistent within a small range of the fast or slow orientation, then this suggests that no observable shear-wave splitting should occur due to receiver-side anisotropy for direct-S ray-paths. Through this approach, we were able to identify additional stations that, although they did not meet the requirements set for “null stations”, they could still be utilized for source-side splitting analysis in a specific region, i.e., the MRC.

Based on this idea, we identified four additional stations (MIDW, NWA0, LCO and SYO), which are plotted in Figure 4.10. However, in the further analysis, we found for some of these stations, like station MIDW and station NWA0, there are a few splitting observations; while for some other stations, like station LCO,

the quality of seismic raw data is too poor to obtain any valid measurements.

Fortunately, we identified a high quality and suitable station on the Antarctic continent, namely station SYO. Previous research indicated a fast splitting direction of approximately  $50^\circ$  (Kubo et al., 1996); However, due to the study's age, details of the individual measurements and the potential back-azimuth variations were not accessible. To gain a deeper understanding of the seismic anisotropy beneath the station, we conducted our own receiver-side splitting analysis using an updated dataset of SKS phases. Fortunately, a long recording span was available for this station from February 8, 1993 to August 31, 2021, the exhibiting relatively good quality waveforms. To reduce the number of earthquakes that needed to be analyzed, we implemented a more stringent criterion for earthquake magnitude, only considering events with a magnitude exceeding 6.0 within the required epicentral distance range ( $90^\circ$  to  $130^\circ$ ). Consequently, 931 events were analyzed for SKS splitting, resulting in 42 measurements of good and fair quality.

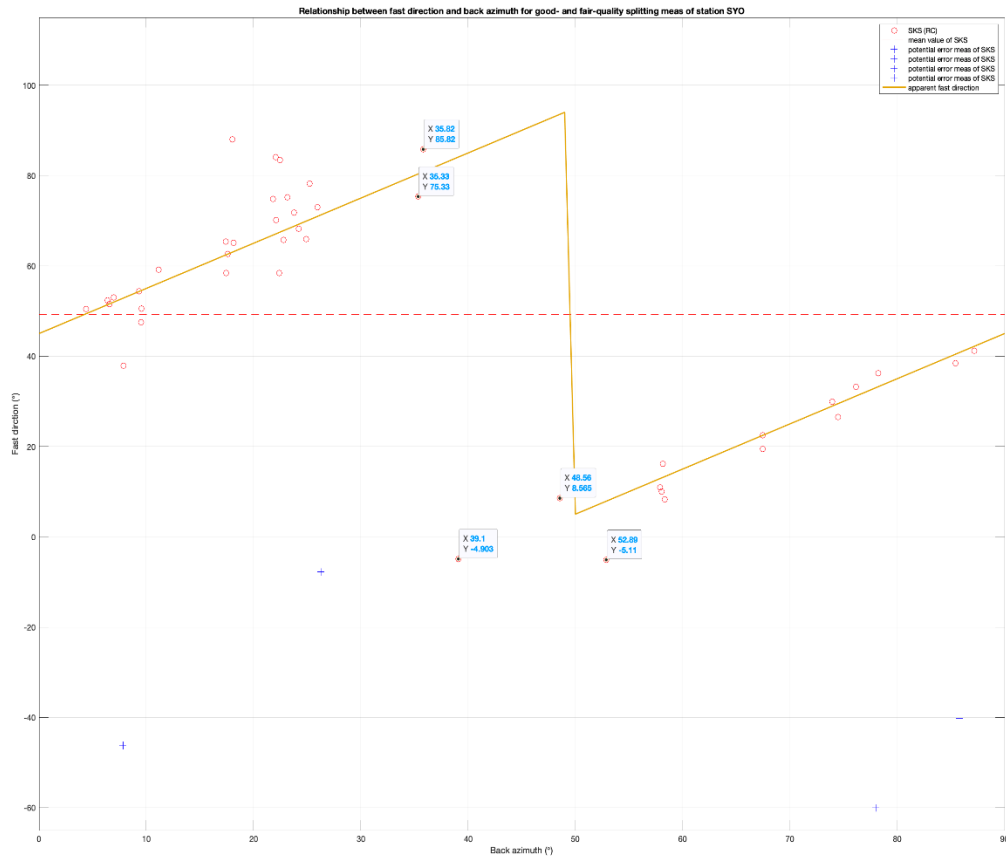


Figure 4.11 Relationship between apparent fast direction and the event back-azimuth for good- and fair-quality split measurements from the RC method at station SYO. The red circles represent results from SKS phases. The dotted red line indicates the average fast direction of all the values, excluding four anomalous results (blue crosses). The gold line illustrates the predicted systematic error in fast direction as a function of back azimuth, according to the empirical equation of Eakin et al., (2019), as outlined in section 3.1.3 (i.e., equation 3.1).

Taking these receiver-side splitting results of the station into consideration (Figure 4.11), we concluded that there are 3 reasons to support why this station can be used for source-side analysis of the MRC:

1. We did not find any good or fair-quality splitting measurements with back-azimuths between  $[35.82^\circ, 48.56^\circ]$ .

2. From location of the station SYO to the selected reference points at the MRC, the back-azimuths are around  $[135^\circ, 145^\circ]$ , which corresponds to the possible range for the slow direction of the anisotropic medium on the receiver side ( $[125.82^\circ, 138.56^\circ]$ ).
3. Most of the null measurements are within the back-azimuth range of  $[35.82^\circ, 48.56^\circ]$  for station SYO, which supports for the inferred orientation of the fast axis beneath the station.

Following these considerations, source-side splitting analysis at station SYO was then applied using only the MRC events with corresponding back-azimuths of  $[125.82^\circ, 138.56^\circ]$ . The remaining processing procedures were the same as described in section 3.2.

## **4.4 Preliminary analysis of source-side splitting results**

Following source-side splitting analysis, we obtained 33 split and 24 null measurements from 54 events along the MRC (Figures 4.12-4.13). Results are obtained for various different regions of the MRC indicating variability between segments, but often similarity in the results recorded at different stations for the same or nearby events, lending support that the splitting signal reflects anisotropy beneath the source rather than beneath the receiver.

To aid visualization, we defined a new quantity,  $\theta$ , to describe the difference between the fast directions of the split measurements and the strike of the plate boundary at the same latitude. This is indicated by the different colors of the splitting bars in Figure 4.12 to indicate which results are,  $[0^\circ, 30^\circ]$ : sub-parallel, shown in red;  $[30^\circ, 60^\circ]$ : oblique, shown in green;  $[60^\circ, 90^\circ]$ : perpendicular, shown in blue.

At the northern end, in the Puysegur region, the types are fall into the category of sub-parallel. For the McDougall and Macquarie regions, for split measurements located off the plate boundary (on the side of the Australian plate), the results are all consistent and sub-parallel. While for the measurements acquired at or very close to the plate boundary, they are generally oblique or perpendicular and more variable. To the south, in the Hjort region, the majority of measurements display a NNE-SSW trending oblique fast direction. In summary, there is a clear variation in the splitting pattern along the plate boundary at the MRC.

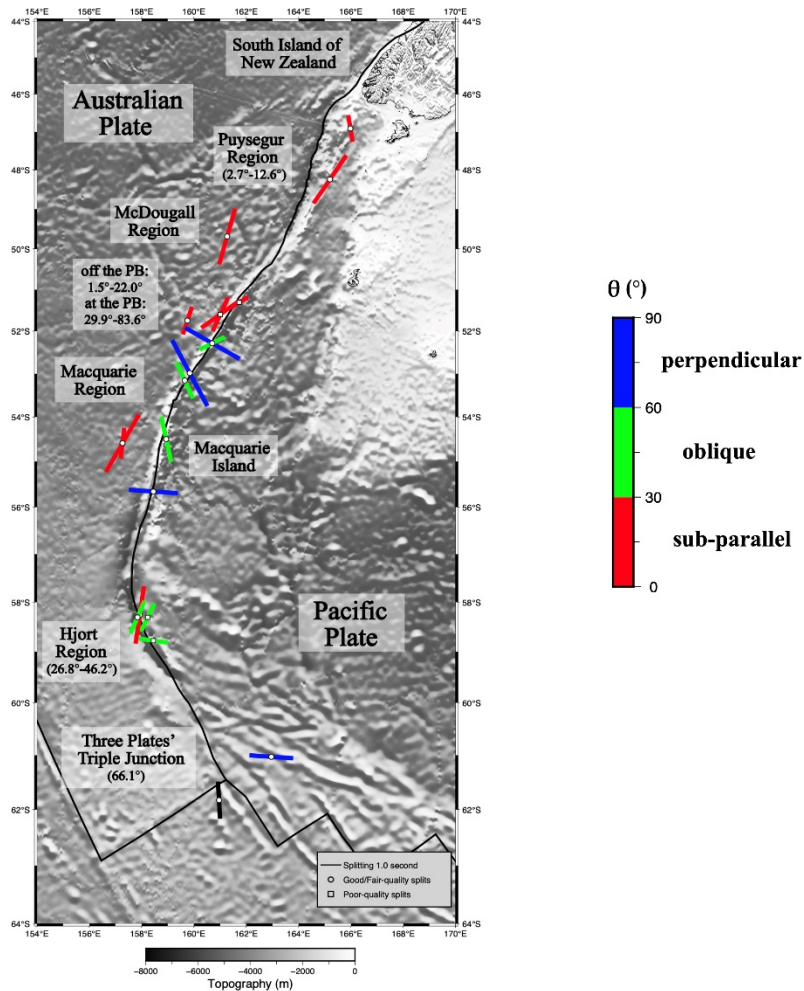


Figure 4.12 Map of the MRC, showing all the split measurements we acquired from both

receiver-side and source-side splitting analysis. The grey-shaded background color corresponds to the bathymetry/topography. The solid line in black illustrates the plate boundary. The main geological and geophysical features of the seafloor are labelled. The colored bars indicate split measurements, with their orientation representing the fast direction and their length representing delay time. The measurements plotted with a small white circle at the center indicate good or fair quality. Measurements with a small white square at the center indicate poor quality. Only the splitting bar on Macquarie Island is from receiver-side splitting analysis, and all the others are from source-side splitting analysis. The color of splitting bar corresponds to " $\theta$ " according to the legend shown, which is measure of how the fast direction compares to the strike of the plate boundary. The values in parentheses under the name of the different MRC regions indicate the range of  $\theta$  (in degrees) for that region.



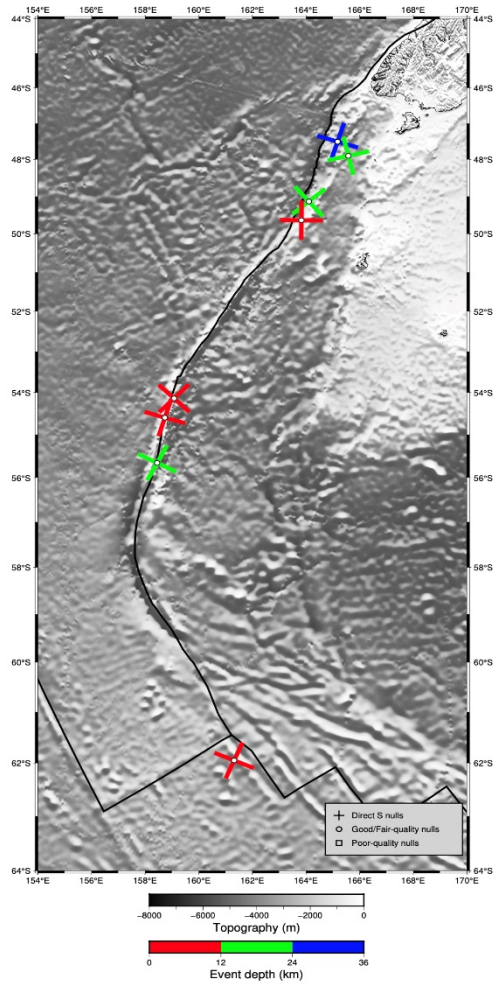


Figure 4.13 Map of the MRC, same as Figure 4.12, except showing all null measurements we acquired from source-side splitting analysis. The crosses indicate null measurements, with their orientation representing the potential fast or slow directions (based on the estimated initial polarization of the shear-wave at the source). In this case, the colors of crosses indicate the depth of the events.

In the Figure 4.13, we plot the null measurements from the source-side splitting analysis and indicate the potential fast/slow directions via the orientation of the crosses.

In comparison to the split measurements, the null measurements are fewer in number, and are mostly located at the Puysegur and Macquarie segments. At the Macquarie segment, the 3 null measurements present a similar pattern,

suggesting a relatively uniform anisotropic source beneath. While for the Puysegur segment, the 4 null measurements acquired are fairly mixed, which may indicate potentially more complex anisotropy is beneath this region where there is a young subduction zone and subducting slab.

# Chapter 5

## Interpretation and Discussion

### 5.1 Potential sources of seismic anisotropy

After the acquisition and initial analysis of splitting and null results from the receiver-side and source-side splitting analysis of the MRC, the first question to consider is where and what is the source of seismic anisotropy? As in which anisotropic layer of the Earth do the shear-wave splitting measurements reflect? After speculation with regards to the source of anisotropy, the evolution of and dynamics beneath the MRC may further be revealed.

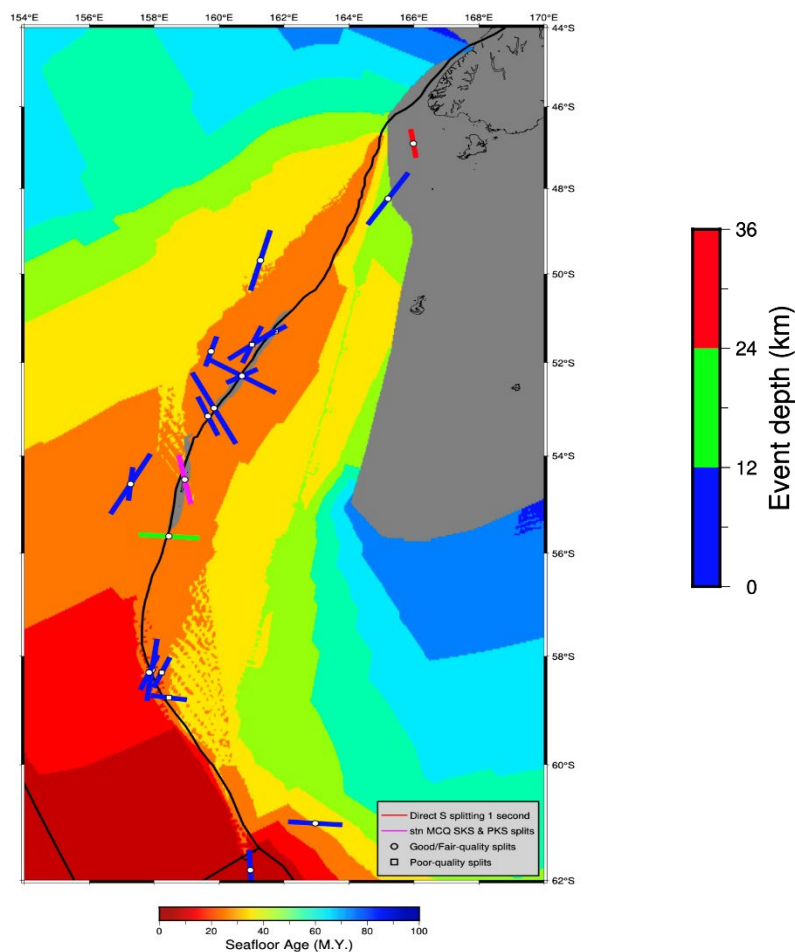


Figure 5.1 Map of seafloor age (background colors) in the vicinity of the MRC study region

from Seton et al., (2020). Shear-wave splitting measurements from both receiver-side and source-side splitting are overlain on top (same as Figure 4.12), and colored by the event depth. The only exception is the splitting bar at Macquarie Island (in magenta) which is from receiver-side splitting analysis. All others are from source-side splitting analysis. The solid black line illustrate the plate boundary.

From the Chapter 1, we know that there are two likely potential sources for our splitting observations of the MRC: first, it may come from frozen-in anisotropy within the oceanic lithosphere of the MRC, or secondly, from seismic anisotropy in the asthenospheric upper mantle beneath the MRC. Considering that both receiver-side and source-side measurements retrieve clear evidence for shear-wave splitting (Figure 4.12), we can first infer the presence of a substantial layer of anisotropy beneath the MRC, enough to generate delay times of  $\sim 0.7$ - $1.8$  seconds that have been observed. The similarity between the receiver-side splitting at station MCQ on Macquarie Island (e.g., Figure 4.3), and the source-side results in same region (Figure 4.12), suggests that the receiver-side and source-side methods are both sensitive to same anisotropic domain. It is always possible that both the lithosphere and asthenosphere may contribute to the observed anisotropy, i.e., that the splitting may be attributed to multiple layers of anisotropy. This is usually assessed by investigating the variation in the shear-wave splitting parameters with respect to the initial polarization of the shear-wave (e.g., Silver and Savage, 1994). As source-side splitting is based on individual ray-paths (i.e., single events), it is not possible to consider the effect of initial polarization. For the receiver-side results, however, back-azimuthal variations (equivalent to the initial polarization for SKS/PKS) are consistent with the predicted pattern of systematic error for a single layer of anisotropy (Figures 4.5-4.8). Moving forward we therefore interpret our results within the framework of a single layer of anisotropy beneath the MRC.

We first consider the possibility that the pattern of shear-wave splitting may be attributed to anisotropy frozen within the lithosphere. The first such evidence to consider is the seafloor age fabric on either side of the MRC as shown in Figure 5.1. First, we can see that all of the splitting results lie on seafloor that is less than 50 million years old, which would at most correspond to lithosphere of  $\sim 92$  kilometers thickness according to the half-space cooling model for oceanic lithosphere (Figure 5.2) and based on Equation 5.1 from Turcotte and Schubert, (2014) given below:

$$y_L = 2.32(\kappa t)^{1/2} = 2.32\left(\frac{\kappa x}{u}\right)^{1/2}. \quad (5.1)$$

Where  $y_L$  indicates the thickness of the oceanic lithosphere,  $\kappa$  refers to the thermal diffusivity, and the  $t$ ,  $x$  and  $u$  are the same as we introduced for the Figure 5.2. If we take  $\kappa = 1 \text{ mm}^2\text{s}^{-1}$ , and the thickness of the oceanic lithosphere at an age of 50 million years is  $\sim 92$  km.

However, most of our splitting measurements are located very close to the plate boundary, on seafloor that is younger than  $\sim 35$  million years, which corresponds to  $\sim 77$  kilometers thick based on the same equation (Equation 5.1). So, we can conclude the oceanic lithosphere beneath the MRC is quite young and with relatively thin thickness. It is therefore unlikely that such a thin layer could generate the amount of anisotropy as we observed (i.e., delay times from shear-wave splitting that are sometimes more than 1 second).

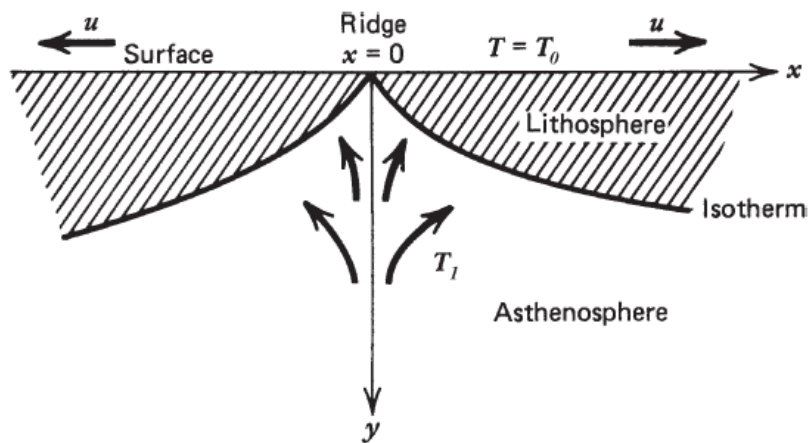


Figure 5.2 Schematic model for oceanic lithosphere cooling, taken from Turcotte and Schubert, (2014). In the figure,  $x$  represents the distance from the ridge axis,  $u$  the horizontal velocity of the surface plates on either side of the ridge, and  $t$  the age of the lithosphere at distance  $x$  from the ridge axis,  $t = x/u$ .

In addition, from the seafloor age map (Figure 5.1), we can consider the paleo-spreading direction, which is expected to be perpendicular to the contours of the seafloor age. If substantial frozen-in anisotropy with an anisotropic strength large enough to be observed, then fast splitting directions should follow a pattern parallel to the paleo-spreading direction, i.e., perpendicular to the contours of seafloor age. However, we do not observe this kind of relationship from comparison between the contours of seafloor age of the MRC and most fast directions of our splitting measurements. So, to sum up, based on initial evidence frozen-in lithospheric anisotropy does not appear to be able to explain our results, either in terms of strength nor direction.

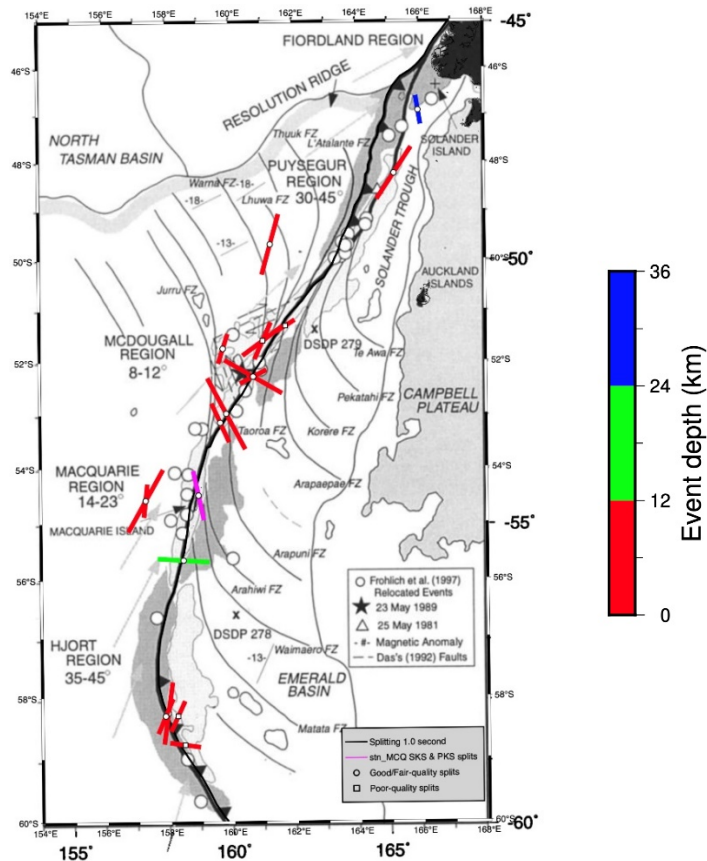


Figure 5.3 Map of the MRC from Massell et al., (2000), illustrating the main geological and geophysical structures as inferred from bathymetric mapping. Thin solid grey lines show the curved shape of relict fracture zones that become asymptotic as they approach the MRC plate boundary. The rest is the same as the Figure 5.1, but with a different correspondence between the color and the event depths.

However, in the MRC region the seafloor fabric is likely modified close to the ridge axis, which can be seen from the relicts of fracture zones of the MRC (Figure 5.3). As what we have introduced in Chapter 2, we can see that the fracture zones have an arcuate shape, and as approaching the plate boundary, they become asymptotic. These features are related to the seafloor spreading process and represent the unique evolution of the MRC. From the distribution of the fracture zones, we can speculate the modified paleo-spreading seafloor fabric of the MRC. The strike of the fracture zones should be the same as the seafloor spreading direction. So, if frozen-in anisotropy within the oceanic

lithosphere does exist, we would expect fast direction of most of our splitting measurements to be parallel or sub-parallel to the strike of relict fracture zones. However, such a correlation is not observed neither at the McDougall region nor the Macquarie region, where most of the relict fracture zones have been mapped. Although for some individual observations, like the results from receiver-side splitting analysis of station MCQ, the fast direction is somewhat similar to the strike of the fracture zones on the Pacific plate. However, this is just a single example, and no consistent pattern is found for most of our splitting observations. We therefore maintain that the primary source of anisotropy is most likely not due to frozen-in anisotropy within the oceanic lithosphere of the MRC.

The next line of evidence to consider is from the analysis of the First Fresnel Zones and comparisons with surface-wave global azimuthal anisotropy, in this case from a global surface-wave model (3D2018\_08Sv, updated in 2018 from Debayle et al., 2016). The First Fresnel Zone (FFZ) refers to the area over which seismic waves are most sensitive to as a function of depths. For the calculation of the FFZ, we utilized the method introduced by Gudmundsson (1996), as indicated by Figure 5.4 and Equation 5.2 below. This calculation requires the average velocity of the shear wave from the surface to the depth of interest, which we retrieved from the isap91 velocity model. We considered shear-waves at two periods, 8 seconds and 25 seconds, which represent the end-members of the frequency range at which we measured the splitting, and took the average value for the final FFZ estimate for a certain depth.



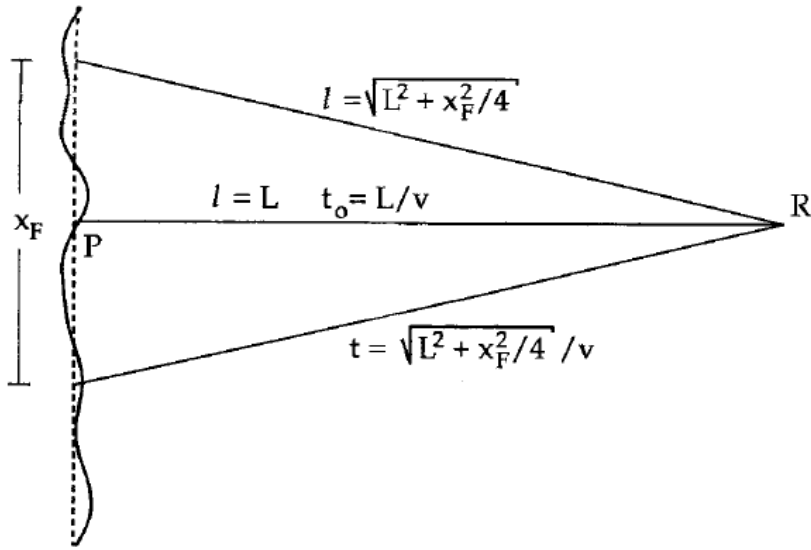


Figure 5.4 Geometrical construction of the First Fresnel Zone from Gudmundsson, (1996).

In Figure 5.4, a plane wave (represented by the dashed line) is perturbed in phase (represented by the solid curve). The wavefront proceeds to propagate a distance,  $L$ , to a receiver at point  $R$  through a homogeneous medium of velocity,  $v$ . Energy at point  $P$  arrives at the receiver at  $R$  at time  $t_0$  having followed a straight path. Energy from adjacent parts of the wavefront arrives slightly later. All energy within the distance  $x_F/2$ , measured on the wavefront from  $P$ , arrives within some time delay,  $\delta t$ , of the minimum-time arrival. If we choose this time delay as a quarter of the period of the recorded wave,  $T/4$ , all this energy interferes constructively. We can then say that the wavefield recorded at  $R$  represents an integral of the wavefield around  $P$  and that variations in phase on the wavefront around  $P$  are averaged in the wavefield at  $R$ . This leads to the definition of a First Fresnel Zone for a plane wave:

$$\delta t = t - t_0 = \left[ \sqrt{L^2 + x_F^2/4} - L \right] / v = T/4 \Rightarrow \quad (5.2)$$

$$x_F = \sqrt{2vTL + v^2 T^2/4} = \sqrt{2\lambda L + \lambda^2/4}$$

In the Equation 5.2,  $\lambda$  is the wavelength and  $L$  is the propagation distance. A phase lag of a quarter period ( $T/4$ ) represents the boundary between constructive and destructive interferences. In our splitting studies, we utilize the velocity of the shear wave,  $v$ , and the period of the shear wave,  $T$ , to calculate the range of the FFZ.

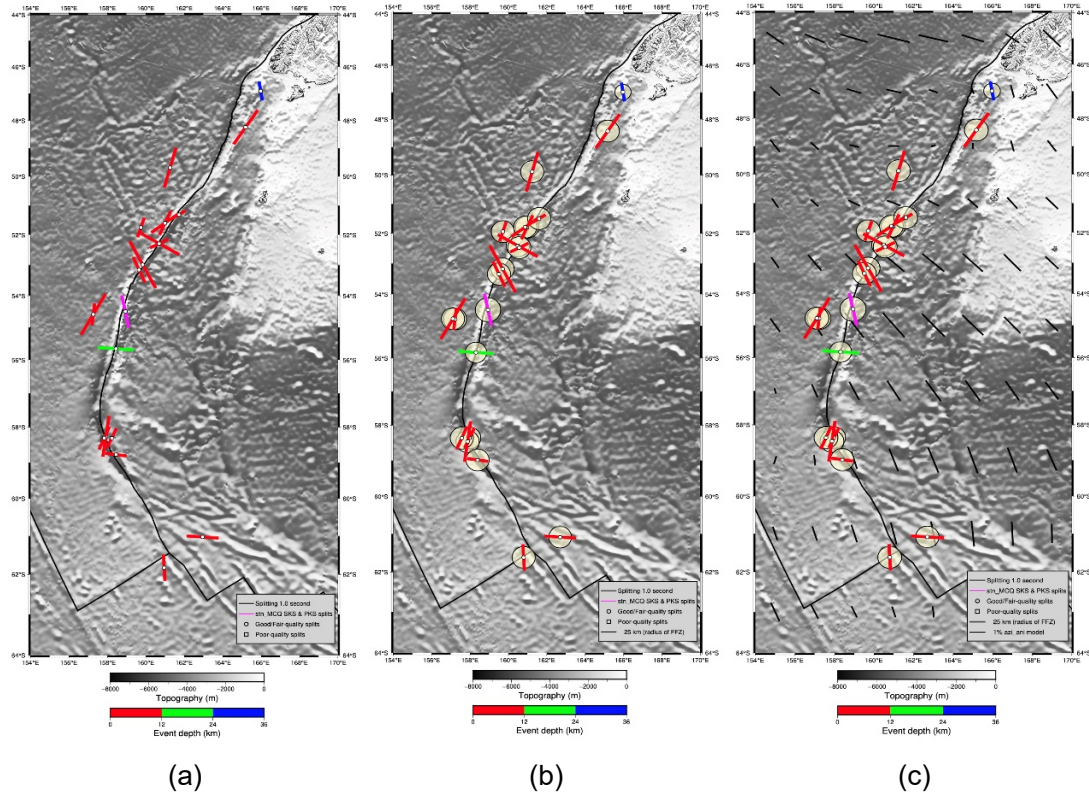
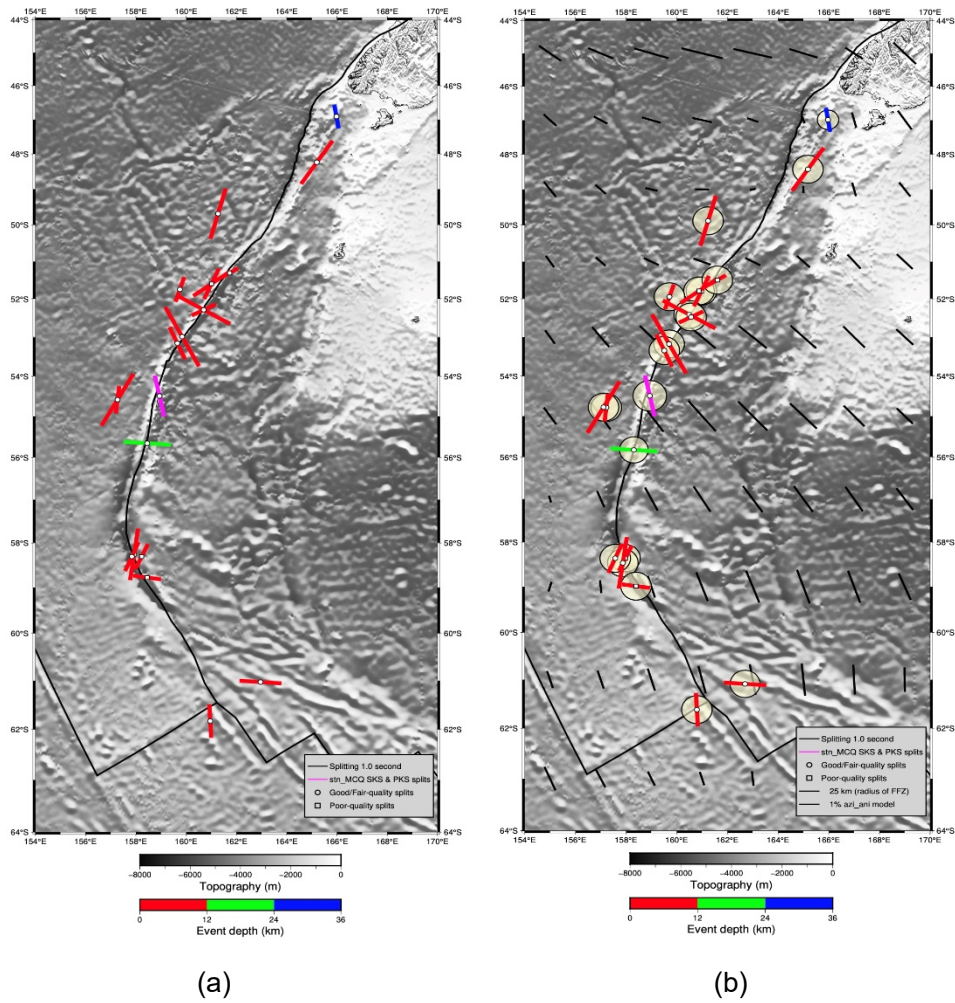


Figure 5.5 Map showing the estimated extent of the First Fresnel Zone (FFZ) of our splitting measurements at lithospheric depths. (a) Splitting measurements plotted at the surface, i.e. same as Figure 4.12. (b) Splitting measurements now centred upon the corrected pierce points for a depth of 50 km, with the range of the FFZ for each individual measurement, represented by the transparent yellow circles. (c) Same as (b), but with black bars representing the azimuthal anisotropy results from global surface-wave model (3D2018\_08Sv, updated in 2018 from Debayle et al., 2016) at a depth of 50 km. The orientation of the bars represents fast axis of anisotropy, and the length of the bars indicates the percentage anisotropy (i.e. strength).

An illustration of the First Fresnel Zones calculated for all our splitting measurements at various depths is shown in Figure 5.5-5.6, and compared to predictions of azimuthal anisotropy from a global surface-wave model (3D2018\_08Sv, updated in 2018 from Debayle et al., 2016).



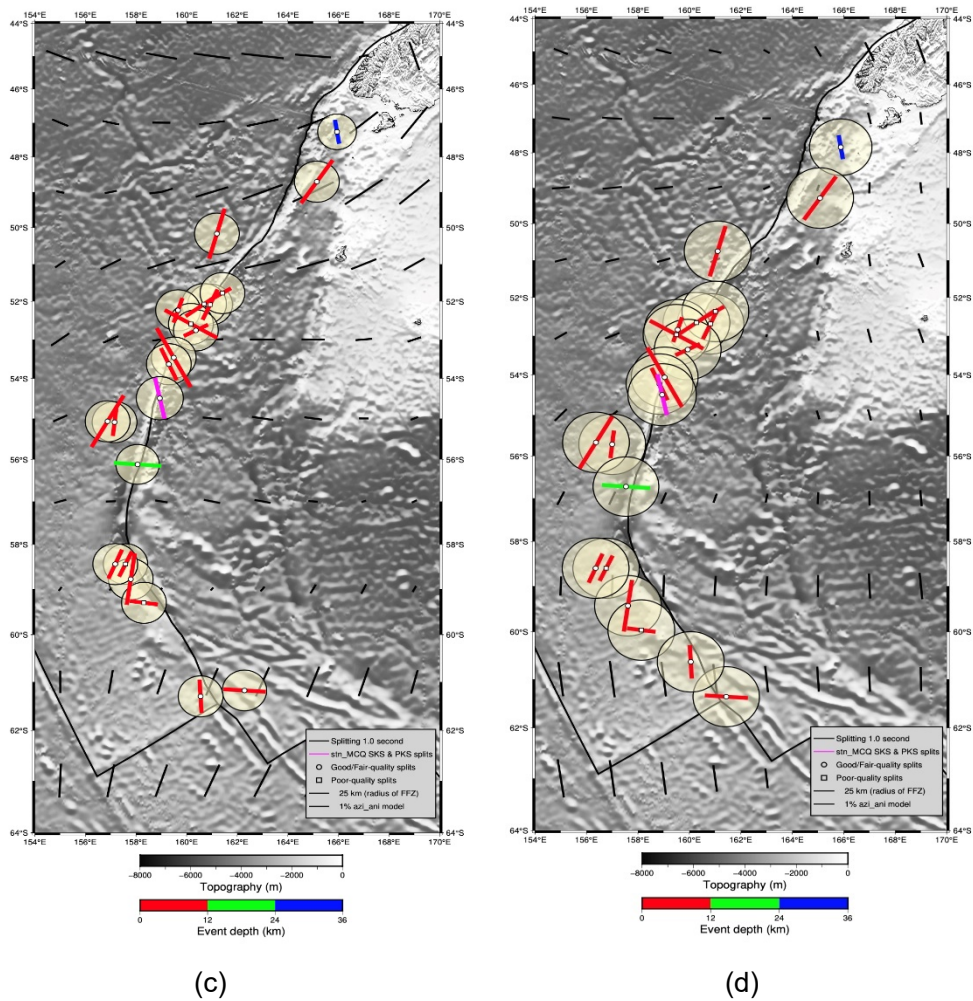


Figure 5.6 Comparison of the First Fresnel Zone (FFZ) with surface-wave derived azimuthal anisotropy (Debayle et al., 2016) at various upper mantle depths. The four figures correspond to depths of (a) zero, i.e., at the surface (same as Figure 4.12 and Figure 5.5a), (b) 50 km (same as Figure 5.5c), (c) 100 km, and (d) 200 km. Plotting conventions are the same as Figure 5.5.

To investigate further, we plot our splitting measurements from both receiver-side and source-side splitting analysis across a range of depths (Figure 5.6), from the surface down to the mid-asthenosphere  $\sim 200$  km depth. We find that as the depth increases, the offset and size of the FFZs become larger, and the fast directions of our splitting measurements become more and more consistent to the azimuthal anisotropy model. In particular for Figure 5.6d, we can see for

the Hjort segment, the fast directions of the majority of the splitting results agree well with the azimuthal anisotropy pattern aligned approximately North-South. Moving northwards along the plate boundary, the azimuthal anisotropy rotates to become more East-West orientated towards the Macquarie region to the McDougall region. For the two splitting measurements at the Puysegur region, they also show consistent features with the azimuthal anisotropy model.

Comparing between the pattern shown by our splitting measurements and the azimuthal anisotropy model results at the three different depths, it appears that the consistency increases with increasing depth. The greatest consistency is found for the depth of 200 km, which corresponds to the asthenosphere beneath the MRC. This further indicate that the primary source of seismic anisotropy is more likely from the asthenosphere, rather than the oceanic lithosphere.

To summarize, from the analysis of lithospheric thickness, possible seafloor spreading fabrics, and azimuthal anisotropy inferred from surface-waves, we can logically speculate that the primary source of the seismic anisotropy detected by our splitting observations is more likely from the asthenosphere, rather than the oceanic lithosphere.

## **5.2 Plate motion and upper mantle dynamics beneath the MRC**

From the analysis of section 5.1, we inferred that the primary source of seismic anisotropy is more likely from the asthenospheric upper mantle. We could then further speculate that the splitting patterns shown by our splitting measurements can be seen as a representation of the dynamics of the upper mantle beneath the MRC. For the next step of our interpretation, we want to



investigate the potential relationship between upper mantle dynamics and the plate motions on the surface.

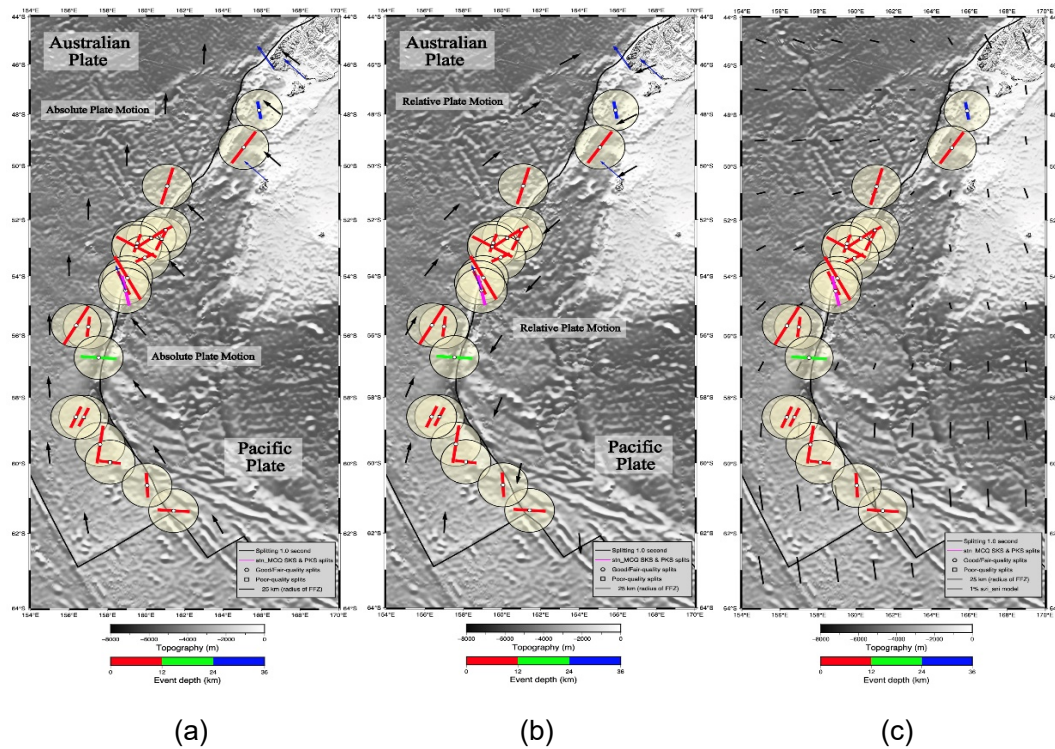


Figure 5.7 Map of splitting results and FFZ for 200 km depth pierce-points (same as Figure 5.6d), compared to plate motion models. In (a), the black arrows represent the absolute plate motion (APM) of the Australian plate and the Pacific plate at selected locations close to the plate boundary of the MRC (model: GSRM 2.1, reference: no-net-rotation, from Kreemer et al., 2014). The blue arrows represent GPS velocity vectors (Kreemer et al., 2014), which correspond to the motion measured at the surface. In (b), the black arrows represent the orientation of relative plate motions (RPM) between the Australian plate and Pacific plates (model: HS3-NUVEL 1A, reference: the Australian Plate/Pacific Plate, from Gripp and Gordon, 2002). The blue arrows represent GPS velocity vectors (Kreemer et al., 2014), which correspond to the motion measured at the surface. Azimuthal anisotropy at 200 km depth (same as Figure 5.6d) is plotted again in (c) for comparison.

In Figure 5.7, absolute and relative plate motions for the Australian and Pacific plates are plotted for comparison with the pattern of shear-wave splitting. For

the splitting measurements away from the plate boundary (i.e., at distances > 20 km) on the Australian Plate side, the fast splitting directions appear similar to both the northwards motion of the Australian Plate, and the azimuthal anisotropy model at 200 km depth (Figure 5.7c). This suggests that the mantle flow in the asthenosphere may be aligned with shear of the plate above. On the Pacific plate side, we only have results at the Puysegur region. These results show generally fast directions parallel to the plate boundary, with orientations similar to the azimuthal anisotropy, but not plate motion. These results may have an additional contribution from the incipient subducting slab beneath this segment, which is discussed further in the following section.

For the splitting measurements on the plate boundary (i.e., distance < 20 km), there are two clusters of results, one around the Macquarie Island in the Macquarie segment and the other in the McDougall segment. The splitting patterns are more complex compared to results away from the plate boundary. Beneath Macquarie Island, both receiver-side and source-side splitting results indicate approximately NW-SE aligned fast directions, oblique to the plate boundary, but matching closely with a GPS velocity vector measured from a GPS station on Macquarie Island (Figure 5.7). This strongly suggests coupled deformation of the crust and upper mantle in this region. Conversely, beneath the McDougall segment just further north, the fast directions rotate to become more plate boundary parallel. These NE-SW fast axis orientations are consistent with the modelled azimuthal anisotropy beneath the Australian plate, and the relative plate motion between Australian and the Pacific plates. This may suggest shear of the upper mantle by the relative motion between the two plates along the plate boundary. Regardless, a remarkable change in seismic anisotropy, and therefore the upper mantle dynamics, appears to exist between the Macquarie region and McDougall region at depth.

### 5.3 Local and regional variations along the MRC

In sections 5.1-5.2, we interpreted the splitting observations for the whole extent of the MRC. However, some local regions of the MRC show distinct and regional features. Here we pay more focus to two local regions, the Puysegur segment, and the boundary between the McDougall and Macquarie segment along the MRC.

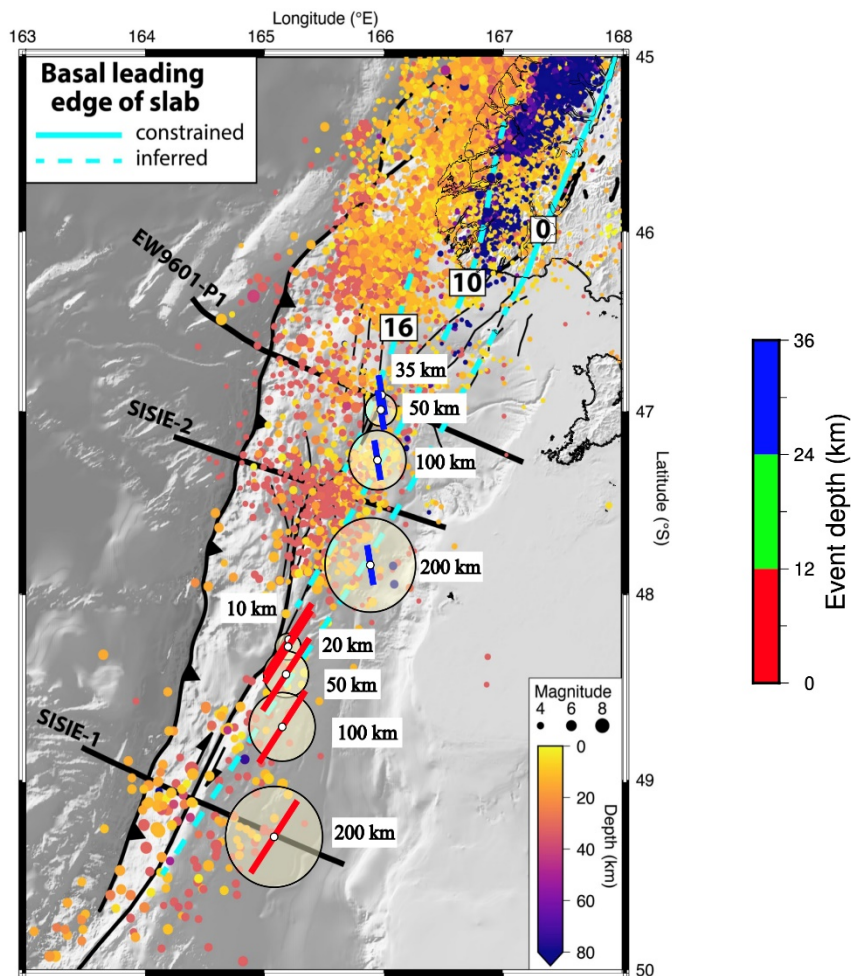


Figure 5.8 Map showing the distribution of seismicity (colored circles) in the Puysegur region modified from Shuck et al., (2022). For comparison, two source-side splitting measurements we acquired in this region, are plotted at the location of earthquakes, corrected pierce points for different depths (20 or 35 km, 50 km, 100 km, 200 km). The orientations of the bars represent the fast splitting direction, the length of the bars the delay



time, and the color representing the depth of the events according to the color bar on the right. The corresponding FFZ for different depths (50 km, 100 km, 200 km) are represented by the transparent yellow circles. The thick cyan lines represent the constrained (solid line) and inferred (dashed line) basal leading edge of the subducting slab at different times (present, 10 million years, 16 million years) in this region. The solid lines in black with triangles represent the subduction trench and pointing in the subduction direction.

Firstly, for the Puysegur region, we consider the pierce-points for the two source-side splitting measurements relative to the Wadati-Benioff zone seismicity in the young subduction here (Figure 5.8). In general, we can see that the fast directions of our splitting measurements are sub-parallel to the plate boundary here. This could suggest the existence of trench-parallel mantle flow in the young subduction zone. However, based on the pierce points of our splitting measurements, it is easy to see there are significant overlaps between the ray path of the shear-waves and the seismicity associated with the subducting slab. This suggests there could be potential contributions of anisotropy from both incipient subducting slab and the asthenosphere below.

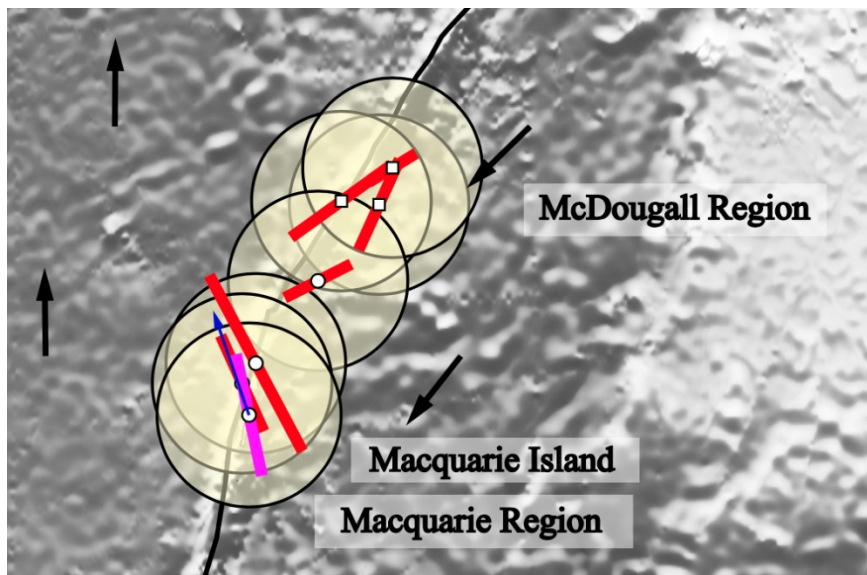


Figure 5.9 Shear-wave splitting measurements from the area between the McDougall

region and the Macquarie region, highlighting the variation in results along strike. The splitting bars in red represent source-side splitting analysis, and the splitting bar in magenta is from receiver-side splitting analysis of the station MCQ. FFZ of each measurement at a depth of 200 km are represented by the transparent yellow circles. The black arrows west of the plate boundary (on the Australian plate side) represent the APM direction, while the black arrows east of the plate boundary (on the Pacific plate side) represent the RPM direction. The blue arrow represents the GPS velocity vector as measured at the surface.

The second area of interest is the boundary of the McDougall and Macquarie regions. From Figure 5.9, we can see there are two groups of the splitting measurements with distinct splitting patterns. One group consists of three splitting measurements in the vicinity of Macquarie Island with one measurement from the receiver-side splitting analysis of the station MCQ (magenta bar), and the other two from source-side splitting analysis (red bars). As described in section 5.2, there is great agreement between the receiver-side and source-side splitting results, both showing NW-SE aligned fast directions, oblique to the plate boundary, and matching the GPS velocity vectors (blue arrow). The other group beneath the McDougall region consists of four splitting measurements with a consistent splitting pattern with fast directions sub-parallel to the strike of the plate boundary here, and consistent with the RPM direction. In addition, the delay times of the group around Macquarie Island are relatively larger compared to that of the other group at the McDougall region. The splitting patterns shown by these two groups are therefore clearly different. However, the reason for the remarkable change in the splitting pattern over such a short distance is not obvious.

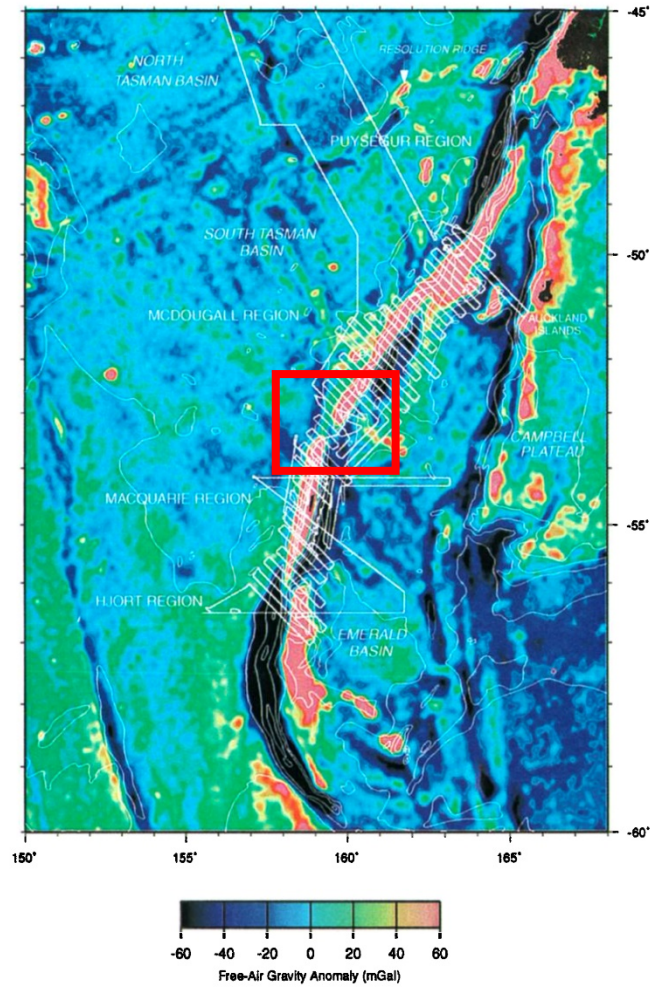


Figure 5.10 Free-air gravity anomaly of the MRC, modified from Massell et al., (2000). The red box highlights the location of the boundary area between the Macquarie region and the McDougall region.

It is possible to find other examples of a change in plate boundary dynamics between different segments of the MRC. As Figure 5.10 (modified from Massell et al., 2000) shows, there is switch in polarity of the free-air gravity anomaly on either side of the plate boundary between the Hjort region and the Macquarie region, and between the McDougall region and the Puysegur region. However, for the boundary between the Macquarie region and the McDougall region (indicated by the red box in Figure 5.10), the results of the free-air gravity anomaly show no noticeable changes, in contradiction to our splitting

observations. One possible reason for the different behavior is that the free-air gravity primarily represents variations in shallow structures (i.e., crustal). While the patterns shown by our splitting measurements is likely more of a manifestation of the deeper upper mantle structure and dynamics. Based on this, we speculate that there may be a significant boundary between the Macquarie and McDougall regions at depth, however, this discovery will require more constraints from other kinds of seismological studies that can target the deep structures beneath the MRC, such as seismic tomography.

# Conclusion

We applied shear-wave splitting analyses to the Macquarie Ridge Complex (MRC), along the Australian-Pacific plate boundary south of New Zealand. The splitting results (fast direction,  $\phi$  and delay time,  $\delta t$ ) vary along the MRC plate boundary, potentially suggesting changes in the underlying seismic anisotropy and thus deformation of the upper mantle.

From the global seafloor age model (e.g., Seton et al., 2020), we know the oceanic lithosphere is quite young near the MRC (less than 35 million years), and thus relatively thin (no thicker than  $\sim 77$  km). This is not considered enough to produce the degree of shear-wave splitting detected. In addition, the pattern of frozen-in lithospheric anisotropy predicted by the geometry of relict fracture zones on the seafloor does not match the shear-wave splitting observations. Moreover, analysis of the First Fresnel Zone, and azimuthal anisotropy from surface waves (Debayle et al., 2016) at various upper mantle depths, shows the greatest similarity at  $\sim 200$  km depth. Based on this evidence, we infer that the primary source of anisotropy is most likely from the asthenosphere, rather than the oceanic lithosphere beneath the MRC.

Based on an asthenospheric source for the seismic anisotropy, we can further infer that the pattern shown by our splitting measurements likely reflects the dynamics of upper mantle beneath the MRC. Consequently, a difference in the pattern of mantle deformation is implied directly beneath the plate boundary, versus beneath the plates (i.e., located away from the plate boundary). This can be summarized as follows:

1. Away from the plate boundary (minimum distance is  $\sim 20$  km), analysis of the First Fresnel Zones and comparison with global azimuthal anisotropy

suggests:

- (i) Beneath the Australian plate, the fast directions are similar to the absolute plate motions, indicating the mantle flow in the asthenosphere is moving in alignment with shear of the plate above.
  - (ii) On the Pacific plate side, the (limited) results at the Puysegur region present fast directions generally parallel to the plate boundary, which may correspond to trench-parallel mantle flow and/or a contribution from both the asthenosphere and the incipient subducting slab.
2. On the plate boundary (i.e., within 20 km), the splitting pattern becomes more complex:
- (i) Beneath Macquarie Island, both source-side and receiver-side splitting results indicate approximately NW-SE aligned fast directions, oblique to the plate boundary, and similar to the GPS velocity vector at the surface, strongly suggesting coupled deformation of the crust and upper mantle in this region.
  - (ii) Conversely, beneath the McDougall region, fast directions rotate to plate boundary sub-parallel, consistent with azimuthal anisotropy, and aligning with relative plate motion. This is consistent with shear of the upper mantle directly beneath the plate boundary due to the relative motion between the two plates.

To conclude, our observations of shear-wave splitting demonstrate that the pattern of mantle deformation beneath the MRC changes both with proximity to

the plate boundary, as well as along the plate boundary itself, potentially reflecting the ongoing evolution of this plate boundary both in space and time.

# Bibliography

Agrawal, S., Eakin, C. M., Portner, D. E., Rodriguez, E. E., and Beck, S. L. (2020). The deformational journey of the Nazca slab from seismic anisotropy. *Geophysical Research Letters*, 47, e2020GL087398. <https://doi.org/10.1029/2020GL087398>.

Ando, M., Ishikawa, Y., and Yamazaki, F. (1983). Shear wave polarization anisotropy in the upper mantle beneath Honshu, Japan. *Journal of Geophysical Research: Solid Earth*, 88(B7), 5850-5864.

Audoine, E., Savage, M. K., and Gledhill, K. (2004). Anisotropic structure under a back arc spreading region, the Taupo Volcanic Zone, New Zealand. *Journal of Geophysical Research: Solid Earth*, 109(B11).

Babuska, V., and Cara, M. (1991). *Seismic anisotropy in the Earth* (Vol. 10). Springer Science and Business Media.

Babuška, V., Plomerová, J., Šílený, J. (1993), Models of seismic anisotropy in the deep continental lithosphere, *Physics of the Earth and Planetary Interiors*, Volume 78, Issues 3-4, Pages 167-191, ISSN 0031-9201, [https://doi.org/10.1016/0031-9201\(93\)90154-2](https://doi.org/10.1016/0031-9201(93)90154-2).

Barruol, G., and Hoffmann, R. (1999). Upper mantle anisotropy beneath the Geoscope stations. *Journal of Geophysical Research: Solid Earth*, 104(B5), 10757-10773.

Barklage, M., D. A. Wiens, A. Nyblade and S. Anandakrishnan (2009), Upper mantle seismic anisotropy of South Victoria Land and the Ross Sea coast, Antarctica from SKS and SKKS splitting analysis, *Geophysical Journal International*, Volume 178, Issue 2, Pages 729–741, <https://doi.org/10.1111/j.1365-246X.2009.04158.x>.

Becker, T. W., Kellogg, J. B., Ekström, G., and O'Connell, R. J. (2003). Comparison of azimuthal seismic anisotropy from surface waves and finite strain from global mantle-circulation models. *Geophysical Journal International*, 155(2), 696-714.

Behn, M. D., Hirth, G., and Kelemen, P. B. (2007). Trench-parallel anisotropy produced by foundering of arc lower crust. *Science*, 317(5834), 108-111.



Ben Ismail, W., and Mainprice, D. (1998). An olivine fabric database: an overview of upper mantle fabrics and seismic anisotropy. *Tectonophysics*, 296(1-2), 145-157.

Bello, M., Cornwell, D., Rawlinson, N., and Reading, A. (2019). Insights into the structure and dynamics of the upper mantle beneath Bass Strait, southeast Australia, using shear wave splitting. *Physics of the Earth and Planetary Interiors*, 289, 45–62. <https://doi.org/10.1016/j.pepi.2019.02.002>.

Bowman, J. R., and Ando, M. (1987). Shear - wave splitting in the upper - mantle wedge above the Tonga subduction zone. *Geophysical Journal International*, 88(1), 25–41. <https://doi.org/10.1111/j.1365-246X.1987.tb01367.x>

Brisbourne, A., Stuart, G., and Kendall, J. M. (1999). Anisotropic structure of the Hikurangi subduction zone, New Zealand—integrated interpretation of surface-wave and body-wave observations. *Geophysical Journal International*, 137(1), 214-230. <https://doi.org/10.1046/j.1365-246x.1999.00786.x>.

Collins, J. A., Wolfe, C. J., and Laske, G. (2012). Shear wave splitting at the Hawaiian hot spot from the PLUME land and ocean bottom seismometer deployments. *Geochemistry, Geophysics, Geosystems*, 13(2).

Conrad, C. P., Behn, M. D., and Silver, P. G. (2007). Global mantle flow and the development of seismic anisotropy: Differences between the oceanic and continental upper mantle. *Journal of Geophysical Research: Solid Earth*, 112(B7).

Crampin, S. (1994). The fracture criticality of crustal rocks, *Geophysical Journal International*, Volume 118, Issue 2, Pages 428-438, <https://doi.org/10.1111/j.1365-246X.1994.tb03974.x>.

Das, S. (1992). Reactivation of an oceanic fracture by the Macquarie Ridge earthquake of 1989. *Nature*, 357(6374), 150-153.

Das, S. (1993). The Macquarie Ridge earthquake of 1989. *Geophysical Journal International*, 115(3), 778-798.

Debayle, E., and Ricard, Y. (2013). Seismic observations of large-scale deformation at the bottom of fast-moving plates. *Earth and Planetary Science Letters*, 376, 165-177.

Debayle, E., Dubuffet, F., and Durand, S. (2016). An automatically updated S - wave model of the upper mantle and the depth extent of azimuthal anisotropy. *Geophysical Research Letters*, 43(2), 674-682.

Duncan, R. A., and Varne, R. (1988). The age and distribution of the igneous rocks of Macquarie Island. In *Papers and Proceedings of the Royal Society of Tasmania* (Vol. 122, No. 1, pp. 45-50).

Eakin, C. M., Long, M. D., Wagner, L. S., Beck, S. L., and Tavera, H. (2015). Upper mantle anisotropy beneath Peru from SKS splitting: Constraints on flat slab dynamics and interaction with the Nazca Ridge. *Earth and Planetary Science Letters*, 412, 152–162. <https://doi.org/10.1016/j.epsl.2014.12.015>.

Eakin, C. M., Rychert, C. A., and Harmon, N. (2018). The role of oceanic transform faults in seafloor spreading: A global perspective from seismic anisotropy. *Journal of Geophysical Research: Solid Earth*, 123. <https://doi.org/10.1002/2017JB015176>.

Eakin, C. M., Wirth, E. A., Wallace, A., Ulberg, C. W., Creager, K. C., and Abers, G. A. (2019). SKS splitting beneath Mount St. Helens: Constraints on Sub-slab mantle entrainment. *Geochemistry, Geophysics, Geosystems*, 20, 4202–4217. <https://doi.org/10.1029/2019GC008433>.

Eakin, C. M., Flashman, C., and Agrawal, S. (2021). Seismic anisotropy beneath Central Australia: A record of ancient lithospheric deformation. *Tectonophysics*, 820, 229123.

Fischer K. M., Wiens D. A. (1996), The depth distribution of mantle anisotropy beneath the Tonga subduction zone, *Earth and Planetary Science Letters*, Volume 142, Issues 1-2, Pages 253-260, ISSN 0012-821X, [https://doi.org/10.1016/0012-821X\(96\)00084-2](https://doi.org/10.1016/0012-821X(96)00084-2).

Foley, B. J., and Long, M. D. (2011). Upper and mid-mantle anisotropy beneath the Tonga slab. *Geophysical Research Letters*, 38, L02303. <https://doi.org/10.1029/2010GL046021>.

Fouch, M. J., and Rondenay, S. (2006). Seismic anisotropy beneath stable continental interiors. *Physics of the Earth and Planetary Interiors*, 158(2-4), 292-320.

Frohlich, C., Coffin, M. F., Massell, C., Mann, P., Schuur, C. L., Davis, S. D., Jones, T., and Karner, G. (1997). Constraints on Macquarie Ridge tectonics

provided by Harvard focal mechanisms and teleseismic earthquake locations. *Journal of Geophysical Research: Solid Earth*, 102(B3), 5029-5041.

Fukao, Y. (1984). Evidence from core-reflected shear waves for anisotropy in the Earth's mantle. *Nature*, 309(5970), 695-698.

Gaherty J.B. (2004), A surface wave analysis of seismic anisotropy beneath eastern North America, *Geophysical Journal International*, Volume 158, Issue 3, Pages 1053–1066, <https://doi.org/10.1111/j.1365-246X.2004.02371.x>.

Greve, S. M., and Savage, M. K. (2009). Modelling seismic anisotropy variations across the Hikurangi subduction margin, New Zealand. *Earth and Planetary Science Letters*, 285(1-2), 16-26.

Griffin, B. J., and Varne, R. (1980) The Macquarie Island ophiolite complex: Mid-Tertiary oceanic lithosphere from a major ocean basin, *Chemical Geology*, Volume 30, Issue 3, Pages 285-308, ISSN 0009-2541, [https://doi.org/10.1016/0009-2541\(80\)90109-6](https://doi.org/10.1016/0009-2541(80)90109-6).

Gripp, A. E., and Gordon, R. G. (2002). Young tracks of hotspots and current plate velocities. *Geophysical Journal International*, 150(2), 321-361.

Hall, C. E., Fischer, K. M., Parmentier, E. M., and Blackman, D. K. (2000). The influence of plate motions on three - dimensional back arc mantle flow and shear wave splitting. *Journal of Geophysical Research: Solid Earth*, 105(B12), 28009-28033.

Hayes, G. P., Furlong, K. P., and Ammon, C. J. (2009). Intraplate deformation adjacent to the Macquarie Ridge south of New Zealand—The tectonic evolution of a complex plate boundary. *Tectonophysics*, 463(1-4), 1-14.

Harmon, N., Forsyth, D. W., Fischer, K. M., and Webb, S. C. (2004). Variations in shear - wave splitting in young Pacific seafloor. *Geophysical Research Letters*, 31(15).

Heintz, M., Kennett, B.L., (2005). Continental scale shear wave splitting analysis: Investigation of seismic anisotropy underneath the Australian continent. *Earth and Planetary Science Letters*, 236 (1), 106–119.

Huang, Z., and Zhao, D. (2021). Chapter 11: Mantle Convection in Subduction Zones: Insights from Seismic Anisotropy Tomography.

Geophysical Monograph Series. Edited by Hauke Marquardt, Maxim Ballmer, Sanne Cottaar, and Jasper Konter, 1<sup>st</sup> ed., 283-301. <https://doi.org/10.1002/9781119528609.ch11>.

Janiszewski, H. A., Gaherty, J. B., Abers, G. A., Gao, H., and Eilon, Z. C. (2019). Amphibious surface-wave phase-velocity measurements of the Cascadia subduction zone. *Geophysical Journal International*, 217(3), 1929-1948.

Jung, H., Katayama, I., Jiang, Z., Hiraga, T., and Karato, S. I. (2006). Effect of water and stress on the lattice-preferred orientation of olivine. *Tectonophysics*, 421(1-2), 1-22.

Karato, S. I., Zhang, S., and Wenk, H. R. (1995). Superplasticity in Earth's lower mantle: evidence from seismic anisotropy and rock physics. *Science*, 270(5235), 458-461.

Karato, S. I. (1998). Some remarks on the origin of seismic anisotropy in the D" layer. *Earth, planets and space*, 50(11-12), 1019-1028.

Karato, S. I. (2008). Deformation of earth materials. An introduction to the rheology of Solid Earth, 463.

Karato, S. I., Jung, H., Katayama, I., and Skemer, P. (2008). Geodynamic significance of seismic anisotropy of the upper mantle: New insights from laboratory studies. *Annual Review of Earth and Planetary Sciences*, 36, 59-95.

Keen, C. E., and Barrett, D. L. (1971). A measurement of seismic anisotropy in the northeast Pacific. *Canadian Journal of Earth Sciences*, 8(9), 1056-1064.

Kendall, J. M., and P. G. Silver (1996), Constraints from seismic anisotropy on the nature of the lowermost mantle, *Nature*, 381, 409-412.

Kendall, J. M., and Silver, P. G. (1998). Investigating causes of D" anisotropy. The core-mantle boundary region, 28, 97-118.

Kennett, B. L. N., Gorbatov, A., and Spiliopoulos, S. (2014). Tracking high - frequency seismic source evolution: 2004 Mw 8.1 Macquarie event. *Geophysical Research Letters*, 41(4), 1187-1193.

Kennett, B. L. N., Gorbatov, A., and Spiliopoulos, S. (2014). Tracking high -

frequency seismic source evolution: 2004 Mw 8.1 Macquarie event. *Geophysical Research Letters*, 41(4), 1187-1193.

Király, E., Bianchi, I., and Bokelmann, G. (2012). Seismic anisotropy in the south western Pacific region from shear wave splitting. *Geophysical Research Letters*, 39, L05302. <https://doi.org/10.1029/2011GL050407>.

Klosko, E. R., Wu, F. T., Anderson, H. J., Eberhart-Phillips, D., McEvilly, T. V., Audoine, E., et al. (1999). Upper mantle anisotropy in the New Zealand region. *Geophysical Research Letters*, 26(10), 1497–1500. <https://doi.org/10.1029/1999GL900273>.

Kneller, E. A., Keken P. E. van, Karato, S., Jeffrey Park J. (2005). B-type olivine fabric in the mantle wedge: Insights from high-resolution non-Newtonian subduction zone models, *Earth and Planetary Science Letters*, Volume 237, Issues 3-4, Pages 781-797, ISSN 0012-821X, <https://doi.org/10.1016/j.epsl.2005.06.049>.

Kreemer, C., Blewitt, G., and Klein, E. C. (2014). A geodetic plate motion and Global Strain Rate Model. *Geochemistry, Geophysics, Geosystems*, 15(10), 3849-3889.

Kubo, A., Hiramatsu, Y., and Kanao, M. (1996). Shear-wave Anisotropy by SKS Splitting in Antarctica. In 30th International Geological Congress, Beijing, Abstract volume.

Lebrun, J. F., Lamarche, G., Collot, J. Y., and Delteil, J. (2000). Abrupt strike - slip fault to subduction transition: The Alpine fault - Puysegur trench connection, New Zealand. *Tectonics*, 19(4), 688-706.

Lebrun, J. F., Lamarche, G., and Collot, J. Y. (2003). Subduction initiation at a strike - slip plate boundary: The Cenozoic Pacific - Australian plate boundary, south of New Zealand. *Journal of Geophysical Research: Solid Earth*, 108(B9).

Li, Z., and Peng, Z. (2017). Stress - and structure - induced anisotropy in southern California from two decades of shear wave splitting measurements. *Geophysical Research Letters*, 44(19), 9607-9614.

Liu, Y., Zhang, H., Thurber, C., and Roecker, S. (2008). Shear wave anisotropy in the crust around the San Andreas fault near Parkfield: spatial and temporal analysis. *Geophysical Journal International*, 172(3), 957-970.

Long, M. D., Hager, B. H., De Hoop, M. V., and Van Der Hilst, R. D. (2007). Two-dimensional modelling of subduction zone anisotropy with application to southwestern Japan. *Geophysical Journal International*, 170(2), 839-856.

Long, M. D., and Silver, P. G. (2008). The subduction zone flow field from seismic anisotropy: A global view. *Science*, 319(5861), 315-318.

Long, M.D., Silver, P.G. (2009). Shear Wave Splitting and Mantle Anisotropy: Measurements, Interpretations, and New Directions. *Surveys in Geophysics*, 30, 407–461. <https://doi.org/10.1007/s10712-009-9075-1>.

Long, M. D. (2010). Frequency-dependent shear wave splitting and heterogeneous anisotropic structure beneath the Gulf of California region. *Physics of the Earth and Planetary Interiors*, 182(1-2), 59–72. <https://doi.org/10.1016/j.pepi.2010.06.005>.

Long, M. D., and Becker, T. W. (2010). Mantle dynamics and seismic anisotropy. *Earth and Planetary Science Letters*, 297, 341–354. <https://doi.org/10.1016/j.epsl.2010.06.036>.

Lynner, C., and Long, M. D. (2013). Sub-slab seismic anisotropy and mantle flow beneath the Caribbean and Scotia subduction zones: Effects of slab morphology and kinematics. *Earth and Planetary Science Letters*, 361, 367–378. <https://doi.org/10.1016/j.epsl.2012.11.007>.

Lynner, C., and Long, M. D. (2014). Sub-slab anisotropy beneath the Sumatra and circum-Pacific subduction zones from source-side shear wave splitting observations. *Geochemistry, Geophysics, Geosystems*, 15, 2262–2281. <https://doi.org/10.1002/2014GC005239>.

Lynner, C., and Long, M. D. (2015). Heterogeneous seismic anisotropy in the transition zone and uppermost lower mantle: Evidence from South America, Izu-Bonin and Japan. *Geophysical Journal International*, 201(3), 1545–1552. <https://doi.org/10.1093/gji/ggv099>.

Malecek, S. J., and Clowes, R. M. (1978). Crustal structure near Explorer Ridge from a marine deep seismic sounding survey. *Journal of Geophysical Research: Solid Earth*, 83(B12), 5899-5912.

Maggi, A., Debayle, E., Priestley, K., and Barruol, G. (2006). Azimuthal anisotropy of the Pacific region. *Earth and Planetary Science Letters*, 250(1-2), 53-71.

Mainprice, D., Nicolas, A. (1989), Development of shape and lattice preferred orientations: application to the seismic anisotropy of the lower crust, *Journal of Structural Geology*, Volume 11, Issues 1-2, Pages 175-189, ISSN 0191-8141, [https://doi.org/10.1016/0191-8141\(89\)90042-4](https://doi.org/10.1016/0191-8141(89)90042-4).

Marson - Pidgeon, K., Savage, M. K., Gledhill, K., and Stuart, G. (1999). Seismic anisotropy beneath the lower half of the North Island, New Zealand. *Journal of Geophysical Research*, 104, 20,277–20,286. <https://doi.org/10.1029/1999JB900212>.

Massell, C., Coffin, M. F., Mann, P., Mosher, S., Frohlich, C., Duncan, C. S., ... and Lebrun, J. F. (2000). Neotectonics of the Macquarie ridge complex, Australia - Pacific plate boundary. *Journal of Geophysical Research: Solid Earth*, 105(B6), 13457-13480.

McNamara, D. E., Owens, T. J., Silver, P. G., and Wu, F. T. (1994). Shear wave anisotropy beneath the Tibetan Plateau. *Journal of Geophysical Research*, 99(B7), 13655-13665. <https://doi.org/10.1029/93JB03406>.

Mehl, L., Hacker, B. R., Hirth, G., and Kelemen, P. B. (2003). Arc - parallel flow within the mantle wedge: Evidence from the accreted Talkeetna arc, south central Alaska. *Journal of Geophysical Research: Solid Earth*, 108(B8).

Mohiuddin, A., Long, M.D., Lynner, C., (2015). Mid-mantle seismic anisotropy beneath southwestern Pacific subduction systems and implications for mid-mantle de-formation. *Physics of the Earth and Planetary Interiors*. 245, 1–14. <https://doi.org/10.1016/j.pepi.2015.05.003>.

Montagner, J. P. (1985), Seismic anisotropy of the Pacific Ocean inferred from long-period surface waves dispersion, *Physics of the Earth and Planetary Interiors*, Volume 38, Issue 1, Pages 28-50, ISSN 0031-9201, [https://doi.org/10.1016/0031-9201\(85\)90120-7](https://doi.org/10.1016/0031-9201(85)90120-7).

Montagner, J. P., and Jobert, N. (1988). Vectorial tomography—ii. Application to the Indian Ocean. *Geophysical Journal International*, 94(2), 309-344.

Montagner, J. P., and Tanimoto, T. (1990). Global anisotropy in the upper mantle inferred from the regionalization of phase velocities. *Journal of Geophysical Research: Solid Earth*, 95(B4), 4797-4819.

Montagner, J. P., and Tanimoto, T. (1991). Global upper mantle tomography of seismic velocities and anisotropies. *Journal of Geophysical Research*:

Solid Earth, 96(B12), 20337-20351.

Montagner, J. P., and Kennett, B. L. N. (1996), How to reconcile body-wave and normal-mode reference earth models, *Geophysical Journal International*, Volume 125, Issue 1, Pages 229–248, <https://doi.org/10.1111/j.1365-246X.1996.tb06548.x>.

Moore, M. M., Garnero, E. J., Lay, T., and Williams, Q. (2004). Shear wave splitting and waveform complexity for lowermost mantle structures with low - velocity lamellae and transverse isotropy. *Journal of Geophysical Research: Solid Earth*, 109(B2).

Morris, G. B., Raitt, R. W., and Shor Jr, G. G. (1969). Velocity anisotropy and delay - time maps of the mantle near Hawaii. *Journal of Geophysical Research*, 74(17), 4300-4316.

Nakajima, J., and Hasegawa, A. (2004). Shear-wave polarization anisotropy and subduction-induced flow in the mantle wedge of northeastern Japan. *Earth and Planetary Science Letters*, 225(3-4), 365-377.

Nicolas, A., and Christensen, N. I. (1987). Formation of anisotropy in upper mantle peridotites - A review. Composition, structure and dynamics of the lithosphere - asthenosphere system, 16, 111-123.

Nowacki, A., Kendall, J.-M., Wookey, J., Pemberton, A., (2015). Mid-mantle anisotropy in subduction zones and deep water transport. *Geochemistry, Geophysics, Geosystems*, 16, 764–784. <http://dx.doi.org/10.1002/2014GC005667>.

Özalaybey, S., and Savage, M. K. (1995). Shear-wave splitting beneath western United States in relation to plate tectonics. *Journal of Geophysical Research: Solid Earth*, 100(B9), 18135-18149.

Paul, J. D., and Eakin, C. M. (2017). Mantle upwelling beneath Madagascar: Evidence from receiver function analysis and shear wave splitting. *Journal of Seismology*, 21(4), 825–836. <https://doi.org/10.1007/s10950-016-9637-x>.

Raitt, R. W., Shor Jr, G. G., Francis, T. J. G., and Morris, G. B. (1969). Anisotropy of the Pacific upper mantle. *Journal of Geophysical Research*, 74(12), 3095-3109.

Roy, S. K., M. R. Kumar, and S. Davuluri (2017), Anisotropy in subduction zones: Insights from new source side S wave splitting measurements from



India, *Journal of Geophysical Research: Solid Earth*, 122, 6454–6472, doi:10.1002/2017JB014314.

Ruff, L. J. (1990). The Great Macquarie Ridge Earthquake of 1989: Introduction, *Geophysical Research Letters*, 17, 989-991.

Ruff, L. J., Given, J. W., Sanders, C. O., and Sperber, C. M. (1989). Large earthquakes in the Macquarie Ridge Complex: transitional tectonics and subduction initiation, *Pure and Applied Geophysics*, 129, 71-129.

Russell, S. A., T. Lay, and E. J. Garnero (1998), Seismic evidence for small-scale dynamics in the lowermost mantle at the root of the Hawaiian hotspot, *Nature*, 396, 255-258.

Russo, R. M., and Silver, P. G. (1994). Trench-parallel flow beneath the Nazca plate from seismic anisotropy. *Science*, 263(5150), 1105-1111.

Savage, M. K. (1999). Seismic anisotropy and mantle deformation: what have we learned from shear wave splitting?. *Reviews of Geophysics*, 37(1), 65-106.

Seton, M., Müller, R. D., Zahirovic, S., Williams, S., Wright, N. M., Cannon, J., ... and McGirr, R. (2020). A global data set of present - day oceanic crustal age and seafloor spreading parameters. *Geochemistry, Geophysics, Geosystems*, 21(10), e2020GC009214.

Shearer, P., and Orcutt, J. (1985). Anisotropy in the oceanic lithosphere— theory and observations from the Ngendei seismic refraction experiment in the south-west Pacific. *Geophysical Journal International*, 80(2), 493-526.

Shimamura, H., Asada, T., Suyehiro, K., Yamada, T., and Inatani, H. (1983). Longshot experiments to study velocity anisotropy in the oceanic lithosphere of the northwestern Pacific. *Physics of the Earth and Planetary Interiors*, 31(4), 348-362.

Shuck, B., Van Avendonk, H., Gulick, S. P., Gurnis, M., Sutherland, R., Stock, J., ... and Hess, T. (2021). Strike - slip enables subduction initiation beneath a failed rift: New seismic constraints from Puysegur Margin, New Zealand. *Tectonics*, 40(5), e2020TC006436.

Shuck, B., Gulick, S. P., Van Avendonk, H. J., Gurnis, M., Sutherland, R., Stock, J., and Hightower, E. (2022). Stress transition from horizontal to vertical forces during subduction initiation. *Nature Geoscience*, 15(2), 149-

155.

Silver, P. G., and Chan, W. W. (1991). Shear wave splitting and sub continental mantle deformation. *Journal of Geophysical Research*, 96(B10), 16,429–16,454. <https://doi.org/10.1029/91JB00899>.

Silver, P. G., and Savage, M. K. (1994). The interpretation of shear-wave splitting parameters in the presence of two anisotropic layers. *Geophysical Journal International*, 119(3), 949-963.

Silver, P. G. (1996). Seismic anisotropy beneath the continents: Probing the depths of geology. *Annual review of earth and planetary sciences*, 24, 385-432.

Smith, G. P., Wiens, D. A., Fischer, K. M., Dorman, L. M., Webb, S. C., and Hildebrand, J. A. (2001). A complex pattern of mantle flow in the Lau backarc. *Science*, 292(5517), 713-716.

Stern, R. J. (2004) Subduction initiation: spontaneous and induced, *Earth and Planetary Science Letters*, Volume 226, Issues 3-4, Pages 275-292, ISSN 0012-821X, <https://doi.org/10.1016/j.epsl.2004.08.007>.

Snydsman, W. E., Lewis, B. T. R., and McClain, J. (1975). Upper mantle velocities on the northern Cocos plate. *Earth and Planetary Science Letters*, 28(1), 46-50.

Tkalčić, H., C. Eakin, M. F. Coffin, N. Rawlinson, and J. Stock (2021), Deploying a submarine seismic observatory in the Furious Fifties, *Eos*, 102, <https://doi.org/10.1029/2021EO159537>. Published on 14 June 2021.

Trampert, J., and van Heijst, H. J. (2002). Global azimuthal anisotropy in the transition zone. *Science*, 296(5571), 1297-1299.

Vinnik, L. P., Makeyeva, L. I., Milev, A., and Usenko, A. Y. (1992). Global patterns of azimuthal anisotropy and deformations in the continental mantle. *Geophysical Journal International*, 111(3), 433-447. <https://doi.org/10.1111/j.1365-246X.1992.tb02102.x>.

Vinnik, L., and Montagner, J.-P. (1996). Shear wave splitting in the mantle Ps phases. *Geophysical Research Letters*, 23(18), 2449–2452. <https://doi.org/10.1029/96gl02263>.

Walpole, J., Wookey, J., Masters, G., and Kendall, J. M. (2014). A uniformly

processed data set of SKS shear wave splitting measurements: A global investigation of upper mantle anisotropy beneath seismic stations. *Geochemistry, Geophysics, Geosystems*, 15, 1991–2010. <https://doi.org/10.1002/2014GC005278>.

Walpole, J., Wookey, J., Kendall, J.-M., Masters, T.-G., (2017). Seismic anisotropy and mantle flow below subducting slabs. *Earth and Planetary Science Letters*. 465, 155–167. <https://doi.org/10.1016/j.epsl.2017.02.023>.

Wayne C. Crawford, Spahr C. Webb; Identifying and Removing Tilt Noise from Low-Frequency (<0.1 Hz) Seafloor Vertical Seismic Data. *Bulletin of the Seismological Society of America* 2000; 90 (4): 952–963. doi: <https://doi.org/10.1785/0119990121>.

Wolfe C. J., Solomon S. C. (1998). Shear-Wave Splitting and Implications for Mantle Flow Beneath the MELT Region of the East Pacific Rise. *Science*, 280(5367), 1230-1232. <https://doi.org/10.1126/science.280.5367.1230>.

Wüstefeld, A., and Bokelmann, G. (2007). Null detection in shear - wave splitting measurements. *Bulletin of the Seismological Society of America*, 97, 1204–1211. <https://doi.org/10.1785/0120060190>.

Wüstefeld, A., Bokelmann, G., Zaroli, C., and Barruol, G. (2008). SplitLab: A shear-wave splitting environment in Matlab. *Computational Geosciences*, 34(5), 515–528. <https://doi.org/10.1016/j.cageo.2007.08.002>.

Yuan, H., and Romanowicz, B. (2010). Lithospheric layering in the North American craton. *Nature*, 466(7310), 1063-1068.

Zhang, Z., Schwartz, S. Y. (1994). Seismic anisotropy in the shallow crust of the Loma Prieta segment of the San Andreas fault system. *Journal of Geophysical Research: Solid Earth*, 99 (B5), 9651-9661.

Zietlow, D. W., Sheehan, A. F., Molnar, P. H., Savage, M. K., Hirth, G., Collins, J. A., and Hager, B. H. (2014). Upper mantle seismic anisotropy at a strike-slip boundary: South Island, New Zealand. *Journal of Geophysical Research: Solid Earth*, 119, 1020–1040.

# Appendix

In the appendix, we list all the splitting measurements (split and null measurements) from both receiver-side and source-side splitting analysis in four tables (A1-A4). Table A1 and A2 include the receiver-side measurements for station MCQ and station SYO respectively. The Table A3 and A4 include the source-side measurements (direct S phase) for split measurements and null measurements respectively.

Table A1. Individual receiver-side splitting measurements (SKS- and PKS-phases) for station MCQ (Network: AU, Longitude: 158.9561°, Latitude: -54.4986°). We list the event date, event location (longitude, latitude, depth), event back azimuth, epicentral distance, seismic phase, fast direction estimated by the RC/SC methods, delay time estimated by the RC/SC methods, split or null classification, and quality.

Evt.date	Evt.long (°)	Evt.lat (°)	Evt.depth (km)	Evt.ba (°)	Dist (°)	Phase	Phi.RC (°)	dt.RC (s)	Phi.SC (°)	dt.SC (s)	Is Null?	Quality
14-Jun-2005	179.41	51.23	51	13.3	106.74	SKS	-35	0.9	-23	0.9	No	good
16-Aug-2007	-76.06	-14.25	35	126.8	97.22	SKS	1	0.6	9	0.7	No	good
19-Dec-2007	-179.52	51.36	29	13.9	107.01	SKS	-22	1.1	-12	1.3	No	good
12-Aug-2010	-77.31	-1.27	207	119.2	107.82	SKS	-13	0.8	-5	1.2	No	fair
24-Jun-2011	-171.84	52.07	52	18.6	108.95	SKS	-16	1.1	-7	1.4	No	fair
11-Apr-2012	-102.73	18.27	20	85.7	109.47	SKS	-50	0.7	-26	1.1	No	fair
03-Jan-2016	93.65	24.81	55	303.8	96.75	SKS	-20	1.3	-4	1.3	No	fair
08-Oct-2017	176.77	52.39	119	11.3	107.55	SKS	-36	1.2	-35	1.2	No	fair
17-Oct-2005	26.50	38.13	8	262.8	144.09	PKS	-42	1.2	-45	1.1	No	fair
11-Apr-2006	21.21	37.91	10	257.4	146.98	PKS	31	1	21	1.1	No	fair
11-Oct-2008	21.54	38.53	6	258.6	147.22	PKS	-55	1.2	-59	1.4	No	fair
08-Oct-2017	46.25	43.37	16	284.2	136.05	PKS	-25	1.6	-28	1.6	No	fair
26-Jan-2014	20.43	38.17	12	257	147.6	PKS	20	1.3	29	1.2	No	fair
26-Sep-2005	-76.40	-5.68	115	122.3	104.49	SKS	-	-	-	-	Yes	good
02-Feb-2013	143.08	42.81	103	348.3	97.88	SKS	-	-	-	-	Yes	good
01-Mar-2019	-70.13	-14.68	257	132.1	99.51	SKS	-	-	-	-	Yes	good
21-Mar-2005	-63.47	-24.98	579	142.2	92.84	SKS	-	-	-	-	Yes	fair
13-Nov-2006	-63.29	-26.08	550	142.8	91.9	SKS	-	-	-	-	Yes	fair
16-Jul-2007	134.88	36.79	351	340.9	93.26	SKS	-	-	-	-	Yes	fair
03-Mar-2008	153.18	46.41	10	355.9	100.65	SKS	-	-	-	-	Yes	fair

05-Jul-2008	152.89	53.88	633	356.2	108.13	SKS	-	-	-	-	Yes	fair
19-Jul-2008	142.21	37.55	22	346.7	92.81	SKS	-	-	-	-	Yes	fair
24-Nov-2008	154.32	54.20	492	357.1	108.4	SKS	-	-	-	-	Yes	fair
07-Apr-2009	151.55	46.05	31	354.8	100.37	SKS	-	-	-	-	Yes	fair
01-Jan-2011	-63.09	-26.79	577	143.2	91.32	SKS	-	-	-	-	Yes	fair
19-Apr-2013	150.80	46.18	122	354.2	100.54	SKS	-	-	-	-	Yes	fair
24-May-2013	153.28	54.87	609	356.5	109.11	SKS	-	-	-	-	Yes	fair
23-Oct-2011	43.51	38.72	16	277.3	134.59	PKS	-	-	-	-	Yes	good
12-Nov-2017	45.96	34.91	19	275.4	130.54	PKS	-	-	-	-	Yes	fair

Table A2. Individual receiver-side splitting measurements (SKS-phase only) for station SYO (Network: PS, Longitude: 39.584999°, Latitude: -69.006699°). We list the event date, event location (longitude, latitude, depth), event back azimuth, epicentral distance, fast direction estimated by the RC method, delay time estimated by the RC method, split or null classification, and quality (events marked with “\*” are considered anomalous).

Evt.date	Evt.long (°)	Evt.lat (°)	Evt.depth (km)	Evt.ba (°)	Dist (°)	Phi.RC (°)	dt.RC (s)	Is Null?	Quality
06-Mar-1993	163.39	-11.08	43	125.3	91.07	75	0.5	No	fair
17-May-1993	151.95	-5.34	33	112.8	92.88	66	0.5	No	good
18-May-1993	122.48	19.82	214	76.2	105.81	33	0.5	No	fair
08-Aug-1993	144.78	12.96	61	99.5	107.45	51	0.6	No	good
06-Sep-1993	153.21	-4.71	73	113.8	93.89	72	0.6	No	good
26-Sep-1993	138.15	9.99	33	94.4	102.34	50	0.4	No	fair
13-Oct-1993	146.03	-5.93	24	107.4	90.33	58	0.6	No	fair
16-Oct-1993	146.20	-5.94	33	107.6	90.38	63	0.5	No	good
25-Oct-1993	146.00	-5.89	10	107.4	90.36	65	0.8	No	fair
01-Feb-1994	163.85	-11.27	33	125.8	91.03	86	1.2	No	fair
18-Apr-1994	154.92	-6.49	43	116	92.78	73	0.6	No	fair
21-Apr-1994	154.08	-5.70	30	114.9	93.25	66	0.3	No	fair
05-Jun-1994	122.04	24.47	16	73.9	109.95	30	1	No	good
20-Oct-1995*	145.39	18.77	225	97.8	113.04	-46	1.2	No	fair
11-Sep-1996*	140.94	35.54	55	85.8	126.7	-40	1.6	No	fair
28-Feb-1997	48.05	38.08	10	7	106.96	53	1.5	No	fair
27-May-1997	-173.33	-15.21	14	148.3	92.8	8	0.6	No	good
08-Aug-1997	-179.14	-15.48	10	142.9	91.36	-5	1.1	No	fair
02-Sep-1997	-75.75	3.85	199	247.5	102.48	22	0.3	No	fair
21-Nov-1997	92.70	22.21	54	48.6	98.64	9	0.8	No	good
30-Aug-1998	148.13	17.09	33	101.1	112.46	59	1.9	No	fair
02-Sep-1998	126.76	5.41	50	85.4	94	38	1.1	No	fair

18-Nov-2000	153.45	-5.38	33	114.2	93.34	68	0.4	No	fair
06-Dec-2000	152.73	-4.22	31	113.1	94.19	75	0.7	No	good
15-Jan-2002	151.10	-5.53	41	112	92.42	84	1.1	No	fair
26-Apr-2002	144.62	13.09	86	99.3	107.52	54	0.7	No	fair
02-Aug-2002	138.97	29.28	426	87.2	120.35	41	1.4	No	fair
03-May-2003	-173.75	-15.14	33	147.9	92.79	11	0.8	No	fair
20-Jun-2003	-71.72	-7.61	558	247.5	90.41	19	0.3	No	fair
15-Oct-2004	122.69	24.53	94	74.5	110.23	26	0.2	No	fair
16-Jan-2005	140.84	10.93	25	96.6	104.17	52	0.7	No	fair
17-Jan-2005	140.68	10.99	12	96.4	104.17	52	0.6	No	fair
21-Nov-2005	130.00	31.02	145	78.2	118.72	36	1	No	fair
08-Dec-2005	146.95	-5.41	217	108.1	91.13	65	0.5	No	good
12-Dec-2005*	71.09	36.36	225	26.3	107.61	-8	0.9	No	fair
31-Mar-2006	48.78	33.50	7	7.9	102.43	38	1.4	No	fair
07-Jul-2006	-173.61	-15.24	35	148.1	92.72	10	0.7	No	fair
13-Nov-2006	151.23	-6.38	11	112.5	91.67	83	1	No	fair
27-Dec-2006	154.42	-5.75	375	115.2	93.31	78	1.2	No	fair
06-Oct-2007	147.14	18.73	35	99.5	113.62	48	0.6	No	fair
09-Jan-2008	85.17	32.29	10	39.1	106.4	-5	0.6	No	fair
01-Jul-2009*	25.47	34.16	19	348	103.39	-60	0.3	No	fair
09-Feb-2010	-173.49	-15.05	10	148.1	92.93	16	1	No	fair
20-Mar-2010	152.24	-3.36	415	112.4	94.83	58	0.7	No	fair
24-Jun-2010	151.16	-5.51	40	112.1	92.46	70	0.9	No	fair
20-Jul-2010	150.70	-5.91	35	111.8	91.93	75	0.8	No	good
04-Aug-2010	146.81	-5.50	226	108	91	88	1.1	No	good
12-Mar-1993	-178.30	-14.35	33	143.4	92.63	-	-	Yes	fair
20-Mar-1993	87.28	29.01	22	41.8	103.75	-	-	Yes	fair
09-Aug-1993	70.72	36.42	210	25.9	107.61	-	-	Yes	fair
09-Aug-1993	70.85	36.36	230	26.1	107.58	-	-	Yes	fair
24-Oct-1993	-98.73	16.78	32	228.5	121.7	-	-	Yes	fair
23-Feb-1994	60.61	30.87	10	18.3	100.78	-	-	Yes	good



24-Feb-1994	60.51	30.78	13	18.2	100.68	-	-	Yes	fair
29-May-1994	94.15	20.54	42	50.4	97.44	-	-	Yes	good
22-Aug-1994	166.42	-11.50	148	128.3	91.55	-	-	Yes	fair
21-Jan-1995	126.90	2.53	47	86.6	91.38	-	-	Yes	fair
20-Apr-1995	126.83	6.29	85	85.2	94.84	-	-	Yes	fair
12-Jun-1997	147.03	-5.95	33	108.4	90.65	-	-	Yes	fair
29-Aug-1997	-175.58	-15.23	33	146.2	92.34	-	-	Yes	fair
28-Oct-1997	-76.68	-4.37	112	243.9	95.07	-	-	Yes	fair
18-Nov-1997	20.66	37.57	33	344.4	107.19	-	-	Yes	fair
22-Dec-1997	147.87	-5.49	179	109	91.37	-	-	Yes	fair
14-Jan-1998	-179.33	-15.73	33	142.8	91.07	-	-	Yes	fair
14-Mar-1998	57.60	30.15	9	15.8	99.75	-	-	Yes	good
25-Nov-1998	158.62	-7.86	48	119.9	92.67	-	-	Yes	fair
28-Sep-2000	-80.58	-0.22	23	241.5	100.23	-	-	Yes	fair
26-Jan-2001	70.23	23.42	16	28	94.81	-	-	Yes	fair
03-Jan-2002	70.69	36.09	129	26	107.29	-	-	Yes	good
22-Jan-2002	26.62	35.79	88	349.1	104.93	-	-	Yes	fair
03-Mar-2002	70.44	36.43	209	25.7	107.58	-	-	Yes	fair
30-Dec-2002	123.41	7.47	10	81.6	94.71	-	-	Yes	fair
08-Oct-2005	73.10	34.73	8	28.3	106.35	-	-	Yes	fair
08-Jan-2006	23.21	36.31	66	346.3	105.71	-	-	Yes	fair
16-Nov-2007	-77.84	-2.31	123	243.4	97.38	-	-	Yes	fair
06-Jan-2008	22.69	37.22	75	346	106.65	-	-	Yes	fair
15-Jul-2008	27.86	35.80	52	350.2	104.86	-	-	Yes	fair
25-Aug-2008	83.52	30.90	12	38.1	104.69	-	-	Yes	fair
28-Oct-2008	67.35	30.64	15	24.2	101.43	-	-	Yes	fair
21-Sep-2009	91.44	27.33	14	45.9	103.18	-	-	Yes	fair
20-Dec-2010	59.17	28.40	12	17.4	98.18	-	-	Yes	fair

Table A3. Individual source-side split measurements (direct S phase only) for events from the MRC measured at various stations. We list network:station, station location (longitude, latitude), event time (including the date), event location (longitude, latitude, depth), event initial polarization, event azimuth, event back azimuth, epicentral distance, the fast direction estimated by the RC method, delay time estimated by the RC method, quality, fast direction converted to the source-side reference.

Netk:stn	Stn.long (°)	Stn.lat (°)	Evt.time	Evt.long (°)	Evt.lat (°)	Evt.dp (km)	Evt.in.po (°)	Evt.azi (°)	Evt.ba (°)	di (°)	Phi.RC (°)	dt.RC (°)	Qy	Fd.ss (°)
GE:SNAA	-2.8379	-71.6707	06-Mar-2001 09:17	157.27	-54.59	10	330.4	187.7207	165.7	53.25	8.9776	0.75	fair	6.4638
GE:SNAA	-2.8379	-71.6707	15-Apr-2006 07:14	165.98	-46.91	35	292.4	184.005	171.3	61.46	17.1897	0.65	fair	-9.1797
GE:SNAA	-2.8379	-71.6707	04-May-2006 02:08	157.93	-58.26	10	330.9	187.8587	166.8	49.66	7.5483	1.4	fair	8.1691
GE:SNAA	-2.8379	-71.6707	16-Nov-2007 13:39	159.75	-51.75	10	289.3	186.5372	167.1	56.26	-4.9977	0.7	fair	18.0721
GE:SNAA	-2.8379	-71.6707	30-Aug-2011 11:36	161.27	-49.69	10	312.6	185.8369	168	58.42	-4.1333	1.4	fair	15.8071
GE:SNAA	-2.8379	-71.6707	27-Oct-2007 11:48	161.01	-51.6	10	306.1	186.0588	168	56.5	-12.1511	0.9	poor	24.2687
GE:SNAA	-2.8379	-71.6707	07-Oct-2021 20:13	158.45	-58.78	10	326.8	187.7081	167.2	49.18	-82.5346	0.7	poor	97.9508
GE:SNAA	-2.8379	-71.6707	04-Nov-2021 16:36	165.2	-48.24	10	201.4	184.3386	170.8	60.09	-25.253	1.4	fair	33.9302
IU:CTAO	146.2545	-20.0882	12-Apr-2007 18:24	160.96	-61.83	10	294.4	339.5013	169.8	42.95	-37.865	0.9	good	-3.1324
G:RER	55.73986	-21.1712	09-Feb-2012 18:52	157.84	-58.31	10	211.7	248.7056	148.2	78.37	-65.9897	0.85	fair	203.4009
G:RER	55.73986	-21.1712	12-Aug-2015 05:16	162.96	-61.03	12	0.6	244.9765	151.8	79.68	36.1255	1.05	fair	6.4638
G:RER	55.73986	-21.1712	16-Jun-2013 14:20	158.23	-58.31	12	238.4	248.3897	148.3	78.56	-68.3	0.75	poor	-154.9206
G:CRZF	51.855308	-46.43096	05-Nov-2009 09:43	160.7	-52.29	10	182.4	226.5581	139.8	64.36	-27	1.5	poor	120.1162
PS:SYO	39.584999	-69.006699	16-Nov-2007 13:39	161.73	-51.31	10	302.7	202.5515	167.1	52.71	-13.4192	0.5	poor	58.5222
PS:SYO	39.584999	-69.006699	30-Aug-2011 11:36	159.84	-52.99	10	220	203.7166	168	50.71	75.2937	1.8	fair	-27.8605
PS:SYO	39.584999	-69.006699	06-Mar-2001 09:17	157.27	-54.59	10	296.4	205.17	165.7	48.62	20.551	1.6	fair	29.789
PS:SYO	39.584999	-69.006699	15-Apr-2006 07:14	159.65	-53.16	10	210	203.8384	171.3	50.5	71.8893	0.95	fair	-24.2125
PS:SYO	39.584999	-69.006699	04-May-2006 02:08	158.45	-55.66	16	278.9	205.1578	166.8	47.93	-43.6555	1.175	fair	93.9711
PS:SYO	39.584999	-69.006699	16-Nov-2007 13:39	160.7	-52.29	10	210.1	203.1973	167.1	51.56	-16.6227	0.675	fair	63.0173
PS:SYO	39.584999	-69.006699	27-Oct-2007 11:48	161.01	-51.6	10	77	202.8802	137.7	52.27	-8.3683	1.125	poor	54.1287

Table A4. Individual source-side null measurements (direct S phase only) for events from the MRC measured at various stations. We list network:station, station location (longitude, latitude), event time (including the date), event location (longitude, latitude, depth), event initial polarization, event azimuth, event back azimuth, epicentral distance, quality, and potential fast/slow directions converted to the source-side reference.

Netk:stn	Stn.long (°)	Stn.lat (°)	Evt.time	Evt.long (°)	Evt.lat (°)	Evt.dp (km)	Evt.in.po (°)	Evt.azi (°)	Evt.ba (°)	dist (°)	Quality	fd/sd.po (°)
GE:SNA	-2.8379	-71.6707	26-Jan-1998 23:06	165.18	-47.51	33	261	184.3145	170.7	60.82	good	107.629/287.629
GE:SNA	-2.8379	-71.6707	30-Sep-2007 09:47	164.11	-49.14	18	320.1	184.7747	170.1	59.14	fair	49.4494/229.4494
GE:SNA	-2.8379	-71.6707	05-Nov-2018 19:54	163.83	-49.64	10	279.3	184.9021	169.9	58.62	fair	90.5042/270.5042
GE:SNA	-2.8379	-71.6707	04-Aug-2019 00:11	165.58	-47.9	16	201.8	184.1874	171.1	60.45	fair	166.5748/346.5748
GE:SNA	-2.8379	-71.6707	05-Feb-2020 12:17	158.74	-54.6	10	267.2	187.1583	166.8	53.36	fair	107.1166/287.1166
GE:SNA	-2.8379	-71.6707	19-May-2022 10:13	159.08	-54.14	10	265.4	186.9863	166.9	53.84	fair	44.1161/224.1161
IU:CTAO	146.2545	-20.0882	20-Oct-2014 07:58	161.32	-61.95	10	185	339.0591	169.6	43.12	fair	113.1182/313.1182
II:WRAB	134.36	-19.9336	12-Apr-2008 00:30	158.45	-55.66	16	349.5	323.3217	158.9	40.01	fair	-62.8566/117.1434